From the Fraunhofer Research Institution
of Marine Biotechnology and Cell Technology
of the University of Lübeck
Director: Prof. Dr. Charli Kruse

"The characterization of morphological changes during axonal degeneration in an *in vitro* model of intracerebral hemorrhage"

Dissertation
for Fulfillment of
Requirements
for the Doctoral Degree
of the University of Lübeck

from the Department of Natural Sciences

Submitted by
Alex Palumbo
from Düsseldorf, Germany

Lübeck 2021

First referee: Prof. Dr. rer. nat. Dr. med. Johannes Boltze

Second referee: Prof. Dr. med. Volker Tronnier

Date of oral examination: 17.05.2021

Approved for printing. Lübeck, 18.05.2021

Declaration

I declare that the present dissertation has been written without any assistance and that intellectual sources have been stated in the text.

The contributions of external collaborators and students of the Fraunhofer Research Institution of Marine Biotechnology and Cell Technology of the University of Lübeck (hereafter: Fraunhofer Research Institution) supervised by Marietta Zille, Ph.D. (Institute for Experimental and Clinical Pharmacology and Toxicology, University of Lübeck) and me are listed below and are detailed in the main text of the dissertation.

Alessa Pabst, Sören Pietsch (both Fraunhofer Research Institution), Reinhard Schulz (Wissenschaftliche Werkstätten, University of Lübeck, Lübeck, Germany), Christopher Kren, and Norbert Koop (both Medical Laser Center GmbH, Lübeck, Germany) contributed to the development of the microfluidic device. Philipp Grüning, Amir Madany Mamlouk (both Institute for Neuro- and Bioinformatics, University of Lübeck, Lübeck Germany), Lara Eleen Heckmann, Svenja Kim Landt, and Luisa Bartram (all Fraunhofer Research Institution) contributed to the development of the deep learning tool and immunostaining experiments. Charlotte Flory (Fraunhofer Research Institution) contributed to the time lapse recording of hemin-induced AxD. Yamil Abdala Villanueva Maluje (Fraunhofer Research Institution) contributed to the pre-processing of microscopic images and the analysis of the microscopic images in immunostaining experiments. Maulana Ikhsan (Institute for Experimental and Clinical Pharmacology and Toxicology, University of Lübeck) contributed to the creation of schematic images. Marietta Zille, Ph.D. designed the study and contributed to the statistical analyses of the data.

This dissertation has not been submitted neither in the past nor in the present to any institution that awards academic titles. I did not seek to obtain the doctor title in any other institution that awards academic titles in the past and have not been awarded the doctor title before.

Table of content

Figure List

Table List

Abbreviation List

4-HNE	4-hydroxynonenal
Act-D	Actinomycin D
AM	Acetoxymethyl
ALLN	Ac-Leu-Leu-Nle-CHO, calpain inhibitor I
APAF1	Apoptotic protease activating factor 1
ATF4	Activating transcription factor 4
AUC	Area under the curve
AxD	Axonal degeneration
BafA1	Bafilomycin A1
BSA	Bovine serum albumin
CCCP	Carbonyl cyanide 3-chlorophenylhydrazone
Chx	Cycloheximide
CNN	Convolutional neural network
CO	Carbon monoxide
DAPI	4′,6-diamidino-2-phenylindole
DCYTB	Duodenal cytochrome B
DFO	Deferoxamine
DIV	Days *in vitro*
DMT1	Divalent metal transporter 1
EBSS	Earle's Balanced salt solution
ER	Endoplasmic reticulum
FACS	Fluorescence-activated cell sorting
Fer-1	Ferrostatin-1
FN	False negative
FP	False positive
GPX4	Glutathione peroxidase 4
HCP1	Heme carrier protein 1
HIF-PHD	Hypoxia-inducible factor prolyl hydroxylase domain
HO	Heme oxygenase
ICH	Intracerebral hemorrhage
JIP1	C-Jun n-terminal kinase-interacting protein 1
MAP	Microtubule-associated protein
MEK1/2	Mitogen-activated protein kinase kinase 1/2
MDA	Malondialdehyde
Mdivi-1	Mitochondrial division inhibitor-1
MEM	Minimum Essential Medium
MLKL	Mixed lineage kinase domain-like protein
MOMP	Mitochondrial outer membrane permeabilization
MPTP	Mitochondrial permeability transition pore
mTOR	Mechanistic target of rapamycin

NAC	N-acetyl-l-cysteine
NAD	Nicotinamide adenine dinucleotide
NMAT2	Nicotinamide Mononucleotide Adenylyltransferase
NMN	Nicotinamide mononucleotide
Nec-1	Necrostatin-1
Nec-1i	Necrostatin-1 inactive
NSA	Necrosulfamide
PBS	Phosphate-buffered saline
PDMS	Polydimethylsiloxane
PMMA	Polymer polymethyl methacrylate
PUMA	p53-upregulated modulator of apoptosis
ResNet	Residual network
RIPK	Receptor-interacting serine/threonine-protein kinase
RNN	Recurrent neural network
SARM1	Sterile alpha motif and toll/interleukin-1 receptor motif–containing 1
SCG10	Superior cervical ganglion 10
STAT3	Signal transducer and activator of transcription 3
STEAP3	Six-transmembrane epithelial antigen of prostate 3
TBA	Thiobarbituric acid
TfR1	Transferrin receptor 1
TNF	Tumor necrosis factor
Wld^{s}	Slow Wallerian degeneration

Abstract

The axon is a crucial part of a neuron that ensures communication between cells. In neurological diseases including intracerebral hemorrhage (ICH, bleeding in the brain tissue), axons degenerate resulting in impaired sensory, motor, and cognitive function. Axonal degeneration (AxD) is defined as the disintegration of the axon over time and characterized by morphological hallmarks (axonal fragments and axonal swellings). To date, the progression of AxD and the underlying molecular mechanisms are poorly understood in the context of disease, and in particular in ICH. Monitoring the morphological hallmarks is essential to understand AxD progression. However, current test systems allow only low throughput and analysis methods are semi-automatic and require manual annotation.

We here designed and manufactured a novel *in vitro* test system containing 16 individual units to enhance the parallel throughput of axonal investigations. Each unit uses a microflow of cell culture medium to allow the directed growth of axons into a separate compartment, which spatially separates axons from their cell bodies. We further developed a deep learning tool based on convolutional neural networks that recognizes axons and the morphological hallmarks of AxD to automatically analyze AxD on time-lapse phase-contrast microscopic images.

Using these tools, we were able to record and quantify the progression of AxD in a model of ICH by exposing axons from primary mouse neurons to the hemolysis product hemin. Hemin induced a concentration- and time-dependent AxD with axonal swellings appearing several hours prior to axonal fragments. Furthermore, axons underwent four morphological patterns of AxD (granular, retraction, swelling, and transport degeneration) that correlated with increasing hemin concentration. We then sought to investigate the underlying mechanisms of hemin-induced AxD using chemical inhibitors that target different potential molecular mechanisms. While the inhibition of calpains and global translation exacerbated AxD, blocking necroptosis, autophagy, apoptosis or ferroptosis did not prevent hemin-induced AxD. However, hemin-treated axons expressed markers of iron-dependent cell death.

Taken together, this study demonstrates that hemin-induced AxD is morphologically heterogeneous and that the underlying mechanisms may be different from neuronal cell death induced by hemin. The novel microfluidic device and the deep learning tools will enable further systematic investigations of AxD in the context of health and disease that will potentially reveal new therapeutic targets for neurological diseases.

Zusammenfassung

Das Axon ist ein essentieller Bereich des Neurons, das die Kommunikation zwischen den Zellen gewährleistet. In neurologischen Erkrankungen wie unter anderem bei der intrazerebralen Hämorrhagie (ICH, Blutung im Gewebe des Gehirns), degenerieren Axone und führen zur Beeinträchtigung der sensorischen, motorischen und kognitiven Funktion. Die axonale Degeneration (AxD) ist als die Desintegration des Axons über die Zeit definiert und durch die morphologischen Merkmale (axonale Schwellkörper und axonale Fragmente) gekennzeichnet. Der Verlauf der AxD und die zugrundeliegenden molekularen Mechanismen sind bislang in Zusammenhang mit Erkrankungen, vor allem mit der ICH, kaum verstanden. Die Nachverfolgung der morphologischen Merkmale ist essentiell um den Verlauf der AxD zu verstehen. Gegenwärtige Testsysteme ermöglichen jedoch nur einen geringen Durchsatz und die Analysemethoden sind semi-automatisch und benötigen manuelle Annotationen.

Wir entwarfen und stellten ein neues *in vitro* Testsystem her, das 16 individuelle Einheiten zur Erhöhung des parallelen Durchsatzes für axonale Untersuchungen enthält. Jede Einheit nutzt einen Mikrofluss des Zellmediums um den gerichteten Auswuchs der Axone in ein separates Kompartiment zu ermöglichen, das die Axone räumlich von deren Zellkörpern trennt. Wir entwickelten basierend auf konvolutionalen neuronalen Netzwerken zusätzlich ein deep learning tool, das Axone und die morphologischen Merkmale der AxD erkennt um die AxD automatisch in mikroskopischen Phasenkontrastbildern von Zeitrafferaufnahmen zu analysieren.

Wir konnten unter Anwendung dieser Werkzeuge den Verlauf der AxD in einem Modell der ICH, bei dem Axone primärer kortikaler Mausneuronen dem Hämolyseprodukt Hämin ausgesetzt waren, aufnehmen und quantifizieren. Hämin induzierte eine konzentrations- und zeitabhängige AxD, bei der die axonalen Schwellkörper mehrere Stunden vor den axonalen Fragmenten erschienen. Des Weiteren durchliefen Axone vier morphologische Muster (Granular-, Rückzug-, Schwellen- und Transportdegeneration), die mit steigender Häminkonzentration korrelierten. Anschließend strebten wir an mittels chemischer Inhibitoren, die verschiedene potenzielle molekulare Mechanismen anvisieren, die zugrundeliegenden Mechanismen der hämininduzierten AxD zu untersuchen. Während die Inhibition von Calpainen und globaler Translation die AxD verschlimmerte, verhinderte die Hemmung von Nekroptose, Autophagie, Apoptose und Ferroptose nicht die hämininduzierte AxD. Häminbehandelte Zellen exprimierten jedoch Marker des eisenabhängigen Zelltods.

Zusammengefasst demonstriert diese Studie, dass die hämininduzierte AxD morphologisch heterogen ist und die zugrundeliegenden Mechanismen vom hämininduzierten neuronalen Zelltod unterschiedlich sein mögen. Das neue mikrofluidische System und das deep learning tool werden weitere systematische Untersuchungen der AxD in Bezug auf Gesundheit und Krankheit ermöglichen, die potenziell neue therapeutische Angriffspunkte für neurologische Erkrankungen offenbaren werden.

1. Introduction

1.1. Axonal degeneration – characteristics and state-of-the-art investigation

1.1.1. The morphological hallmarks of axonal degeneration

The cerebral cortex consists of approximately 86 billion neurons[1]. Neurons comprise of i) the soma to regulate cellular functions, ii) dendrites to receive input signals from other neurons, and iii) the axon to transmit information to neighboring cells[2]. Axons are thin filamentous structures that propagate electrical action potentials along their shafts, leading to the release of neurotransmitters at chemical synapses[2]. Since axons are crucial to sustain neuronal communication, their degeneration has devastating consequences such as impaired sensory, motor, and cognitive function as evidenced in many neurodegenerative diseases including Alzheimer's disease, multiple and amyotrophic lateral sclerosis[3].

Axonal degeneration (AxD) is characterized by the disintegration of the axon resulting in separated axonal fragments[4]. Another morphological hallmark of AxD are axonal swellings that emerge from the blebbing of the axon and contain disorganized cytoskeleton elements and swollen mitochondria[5,6]. The relationship between axonal swellings and axonal fragments is still under investigation. However, some studies suggested a temporal pattern in the occurrence of axonal swellings and axonal fragments[6,7]. In these studies, axonal swellings were described to precede axonal fragmentation in an *in vitro* model of nutrient deprivation and in an animal model of multiple sclerosis[6,7] (**Fig. 1**).

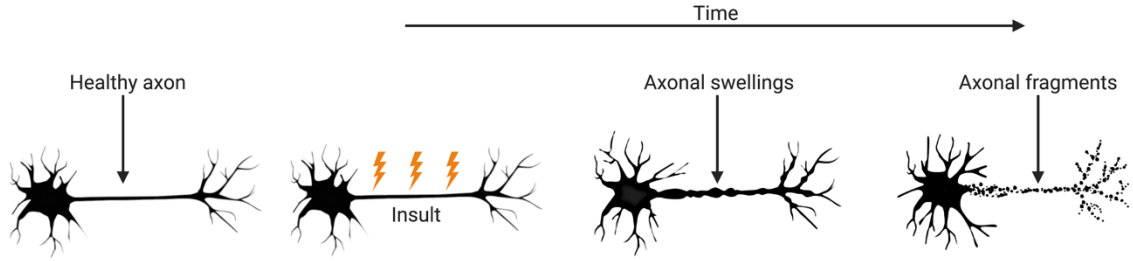

Fig. 1 The proposed model of AxD.
The healthy axon does not contain any morphological hallmarks of AxD. Upon an insult, axonal swellings appear at different locations along the axon, followed by the disintegration of the axon in form of individual axonal fragments over time. Image courtesy: Maulana Ikhsan. Created with BioRender.com.

The sequential occurrence of axonal swellings and fragments suggests that AxD progresses in different phases, the so-called latent and catastrophic phase [7,8]. In the

latent phase, no morphological changes of the axon are evident, whereas the catastrophic phase is characterized by the occurrence of axonal swellings and the subsequent disintegration of the axon into axonal fragments[7,8].

However, the occurrence of axonal swellings does not necessarily result in AxD since axons exhibiting axonal swellings have been reported to be partially recovered in an animal model of multiple sclerosis[6,9]. This may suggest that AxD may be a more complex process requiring further investigation including uncovering the exact role of the morphological hallmarks. In addition, if the occurrence of axonal swellings represents a phase during which AxD is reversible, targeting axonal swellings may be an interesting target for therapeutic strategies of neurological diseases. Thus, a further detailed description and monitoring is required.

1.1.2. The molecular mechanisms of AxD

1.1.2.1. Axonal calpain activation

Calpain is a non-lysosomal cysteine protease that is able to cleave intraaxonal proteins belonging to signaling pathways and the cytoskeleton[10]. In the context of anoxia- and stretch-mediated axonal injury, it has been described that axonal sodium influx leads to the inversion of the sodium/calcium exchanger due to the loss of sodium channel inactivation, causing an increase of intraaxonal calcium levels[11–13]. Calcium activates calpain that degrades the α-subunit of sodium channels in axons thus enhancing the deleterious feedforward loop of sodium influx[13–16]. The resulting further increase of calcium activates ryanodine and inositol trisphosphate receptors of the endoplasmic reticulum (ER) leading to further calcium release that affects the mitochondrial permeability transition pore (mPTP) and leads to apoptosis[17,18].

Furthermore, calpain also degrades microtubules and neurofilaments of the axonal cytoskeleton[14,19–22]. This may be partially mediated by the degradation of microtubule-associated proteins (MAPs) that are responsible for microtubule assembly and stabilization[10]. However, the underlying reasons why microtubules, MAPs and neurofilaments are specific substrates of calpain remain to be elucidated[10,23] (**Fig. 2**).

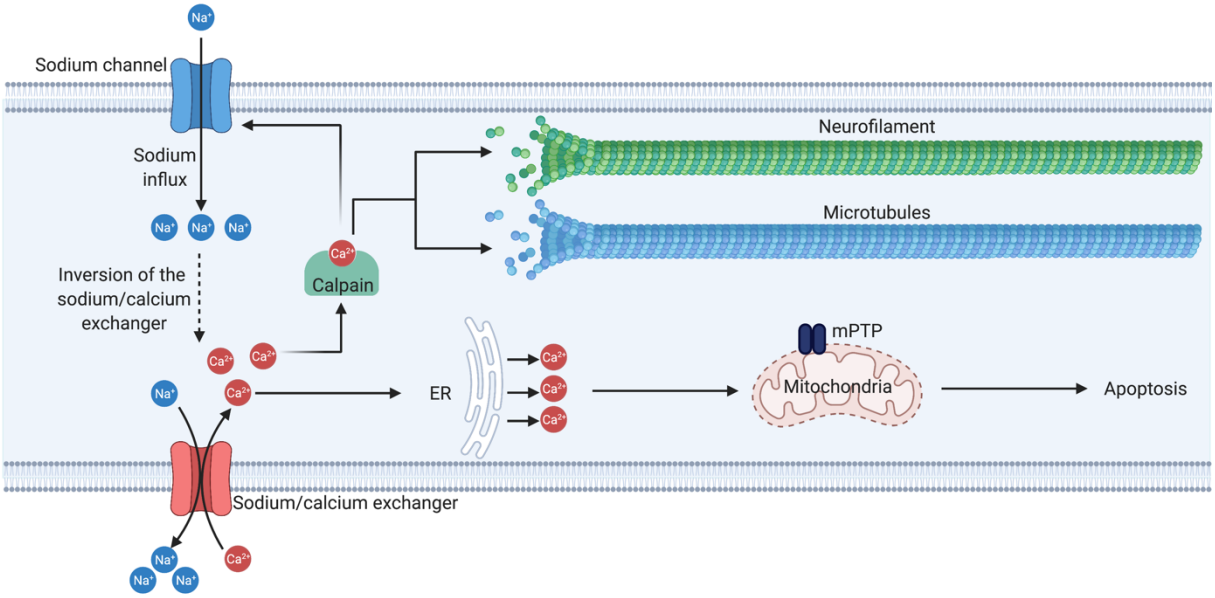

Fig. 2 Calpain activation in AxD.
Calpain degrades microtubules and neurofilaments of the axonal cytoskeleton and negatively affects the sodium channel. Sodium influx is increased and leads to elevated intraaxonal calcium levels due to sodium/calcium exchanger inversion. Calcium further activates calpain and induces calcium release from the ER that affects the mPTP of mitochondria leading to apoptosis. Created with BioRender.com.

1.1.2.2. Axonal apoptosis

Apoptosis is a regulated cell death mechanism during which cells shrink, undergo pyknosis (chromatin condensation), karyorrhexis (DNA fragmentation), and nuclear fragmentation and form apoptotic bodies[24,25]. In general, apoptosis involves proapoptotic proteins that oligomerize at the mitochondrial membrane and lead to mitochondrial outer membrane permeabilization (MOMP). Subsequently, the apoptotic protease activating factor 1 (APAF1) and cytochrome c form the apoptosome. The apoptosome ultimately leads to the activation of cysteine-aspartic proteases called caspases, such as caspase-3 and caspase-6[26].

Apoptosis has also been reported to be involved in AxD[27–30]. The synthesis of the proapoptotic protein p53-upregulated modulator of apoptosis (PUMA) in the soma is required to initiate AxD upon nutrient deprivation[30]. In another study of axonal nutrient deprivation, the release of cytochrome c and the activation of caspases such as caspase-3, and caspase-6 were detected[28] (**Fig. 3**).

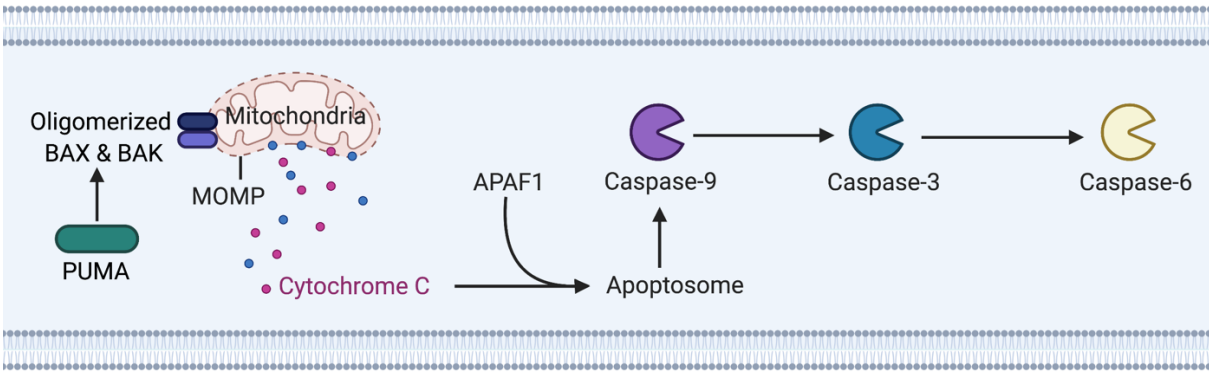

Fig. 3 Apoptosis in AxD.
PUMA induces MOMP formation upon oligomerization of the proteins BAX (Bcl-2-associated X) and BAK (Bcl-2 homologous antagonist killer) leading to apoptosome formation via cytochrome c and APAF1. The apoptosome induces the caspase cascade in which caspase-9, caspase-3 and caspase-6 are successively activated. Created with BioRender.com.

1.1.2.3. Axonal autophagy

Another mechanism involved in AxD is autophagy. Autophagy is a cellular process by which senescent, damaged or dysfunctional cytosolic components and macromolecules are degraded to maintain the cellular homeostasis[31]. Specific organelles named autophagosomes are synthesized and fuse with lysosomes to form autolysosomes that degrade cellular components[31]. As neurons have to sustain the physiology of their somata and axons over long distances, autolysosome formation is a crucial step to maintain neuronal functionality over the whole lifetime as neurogenesis is limited in the brain[2].

Autophagosomes form at the distal tip of axons and are transported retrogradely to the soma by the motor protein dynein during which they mature upon fusion with lysosomes[32–34]. Autophagosome accumulation has been reported in AxD injury models of excitotoxicity-mediated axonal dystrophy and optic neuropathy[35–37]. Why autophagosomes accumulate in axons is not fully understood yet. Axons degenerating after spinal cord injury show elevated levels of proteins that are involved in autophagosome biogenesis[38]. In turn, inhibiting autophagy-initiating upstream proteins attenuates AxD in spinal cord and optic nerve injury[39]. Another possibility is that axonal transport is impaired causing autophagosome accumulation as has been demonstrated upon inhibiting lysosomal proteolytic activity and the knockdown of the protein c-Jun N-terminal kinase-interacting protein 1 (JIP1)[34,40] (**Fig. 4**).

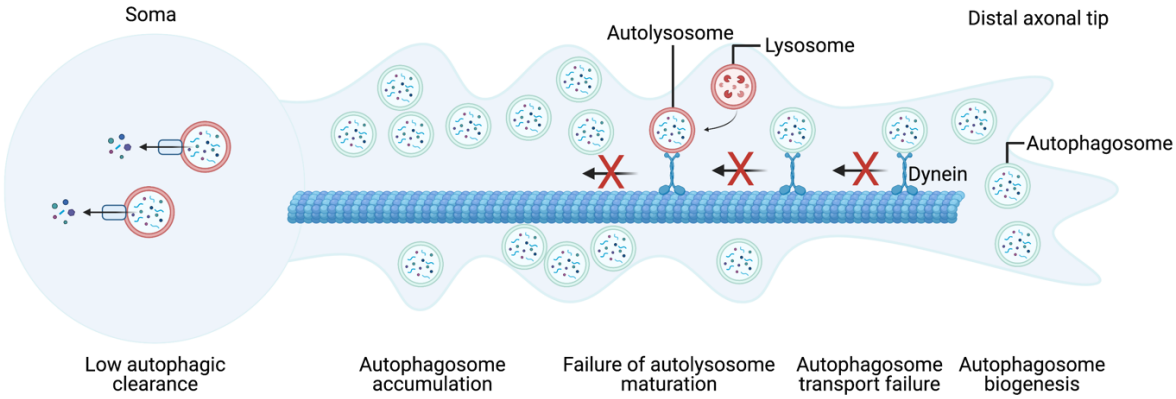

Fig. 4 Autophagy in AxD.
The retrograde transport of synthesized autophagosomes via dynein is disrupted and limits autolysosome maturation. Consequently, autophagosomes accumulate in the axon and autophagic clearance is reduced in the soma. Created with BioRender.com.

1.1.2.4. Axonal necroptosis

Necroptosis is another cell death pathway that has been detected in AxD upon axotomy *in vitro* and sciatic nerve and optic nerve injury[41]. Necroptosis is a regulated cell death mechanism with necrotic morphology, i.e., cytoplasmic and organelle swelling and plasma membrane rupture[24,25]. It involves the activation of receptor-interacting serine/threonine-protein kinase (RIPK) 1 which assembles with RIPK3 to the so-called necrosome. This leads to the phosphorylation of mixed lineage kinase domain-like (MLKL) which forms pores in the plasma membrane[42–45].

The contribution of necroptosis in both vinblastine-induced and axotomy-mediated AxD has been demonstrated by silencing RIPK3 and MLKL which blocked AxD[41]. Another study reported that tumor necrosis factor (TNF) induces axonal necroptosis as evidenced by MLKL phosphorylation within the axon[46]. When the dimerization of MLKL was induced within the axon, survival factors such as superior cervical ganglion 10 (SCG10) and nicotinamide mononucleotide adenylyltransferase (NMAT2) that inhibit sterile alpha motif and toll/interleukin-1 receptor motif–containing 1 (SARM1) were decreased[46]. This finding suggests that neuroinflammation-mediated axonal necroptosis is upstream of the SARM1-dependent AxD pathway[46] (for review about SARM1-dependent AxD pathway, see[47]). (**Fig. 5**).

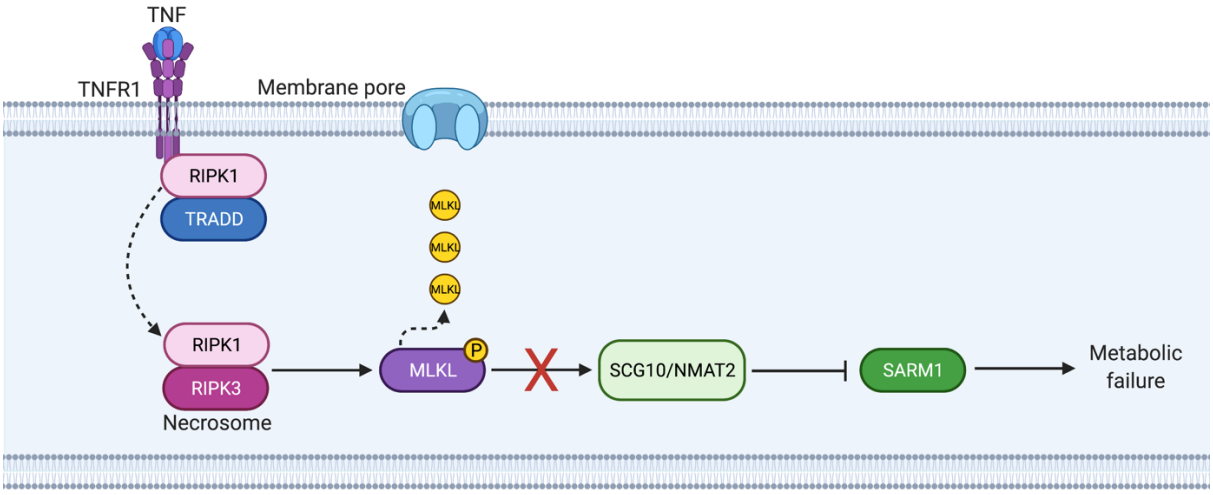

Fig. 5 Necroptosis in AxD.
Following the activation of the TNF receptor 1 (TNFR1) by TNF, RIPK1 forms a necrosome with RIPK3 leading to the phosphorylation of MLKL. pMLKL induces membrane rupture by forming a pore in the membrane and the loss of SCG10 and NMAT2 resulting in SARM1-mediated metabolic failure. Created with BioRender.com

1.1.2.4. The systematic investigation of the molecular mechanisms in AxD

The herein described molecular mechanisms of AxD have been investigated using several AxD models in different experimental conditions. However, it is still not clear why AxD involves different molecular mechanisms that hamper axonal protection and whether the different molecular mechanisms of AxD are intertwined in certain conditions.

To comprehend this complexity, prospective studies may need to examine systematically the involvement of each molecular mechanism by using tools that enable enhanced experimental throughput and automatic analysis of AxD.

1.1.3. Modeling AxD *in vitro*

The investigation of AxD requires elaborate tools to precisely dissect the extent and progression of AxD. This can be achieved by i) cell culture applications that facilitate the induction and imaging of AxD and ii) analytical tools that allow the continuous assessment of the axonal morphology and detection of the morphological hallmarks of AxD.

In vitro experiments enable the direct investigation of individual axons. Specifically, several cell culture systems have been developed to spatially separate axons from their somata allowing to dissect the axon-soma relationship in AxD during development and disease[48,49]. Although the mechanisms of AxD need to be validated *in vivo*, *in vitro* cell culture applications increase experimental throughput thereby allowing to model

several biological scenarios, whether developmental or pathological, with minimal time and costs[50].

Differences in the experimental setups also affect the choice of analytical tools. For instance, fluorescently labelled axons offer a higher signal-to-background ratio to analyze AxD whereas phase-contrast microscopy of non-labelled axons allow the continuous recording of AxD over several hours or days.

1.1.3.1. The limitations of current microfluidic devices to study AxD

As axonal injury signals also affect the soma and *vice versa*[51], it is necessary to examine both components individually. The challenge of investigating AxD *in vitro* is to specifically treat and image axons or somata individually to examine how AxD progresses and is molecularly regulated. *In vitro* tools such as microfluidic devices contain separated compartments to spatially isolate axons from their somata (**Fig. 6**). The soma compartment is connected to the axonal compartment by microgrooves to allow the outgrowth of axons. Axonal outgrowth is mediated by a microflow, which is established by filling level differences of the cell culture medium between the two opposing compartments.

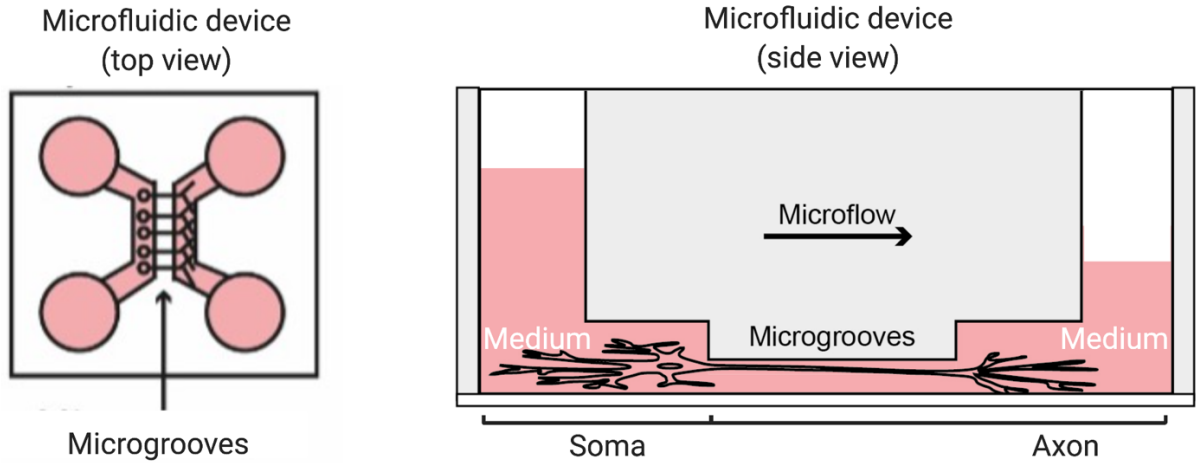

Fig. 6 The working principle of microfluidic devices.
Axons are spatially separated from their somata as they grow into a second compartment (top view). Both compartments are separated by microgrooves. The growth of the axons is driven by the medium volume difference between the two compartments resulting in a microflow (side view). Image courtesy: Marietta Zille. Created with BioRender.com

In an attempt to increase experimental flexibility allowing the exposure of axons to different experimental conditions, this configuration has previously been modified by arranging the compartments radially around a singular soma compartment[52]. While neurons reside in the central soma compartment, their axons spread into several individual axonal compartments that surround the central compartment. However,

axons exposed to one experimental condition may induce retrograde signaling to their somata. In response to the retrograde signaling, those neurons may eventually not only affect their own axons but also neighboring neurons whose axons are exposed to a different experimental condition in another axonal compartment. To avoid potential interactions among different experimental conditions and to ensure increased experimental yield, up to 12 individual microfluidic devices have previously been combined in a conventional 12-well plate[53].

However, the manufacturing of each of the 12 individual microfluidic devices is laborious and time-consuming. Furthermore, the individual microfluidic devices are not fixed within the 12-well plate. This may lead to poor recording quality as the individual microfluidic devices within the 12-well plate may shift during automatic microscopic imaging. Furthermore, the positions of the individual microfluidic devices are not consistent as they are placed manually within the 12-well plate. This limits the experimental parallelization as each microfluidic device needs to be treated individually and recording positions need to be adjusted manually for each experiment.

1.1.3.2. The limitations of current analytical tools of AxD

A major challenge in studying AxD is the quantification of AxD in microscopic images. AxD is quantitatively assessed by analyzing the morphological hallmarks of AxD[7,54]. The occurrence and motility of axonal swellings are determined by defining a region of interest, kymograph analysis, or calculating the ratio of the number of swellings compared to the axon length[7,53,55,56]. On the other hand, axonal fragments have been identified by binarizing microscopic images[54,57]. Structures that are continuously connected are interpreted as axons, while isolated, non-connected elongated structures are interpreted as axonal fragments. The ratio of axonal fragments to total axons has previously been represented as the AxD index[54,57].

However, the AxD index does not consider axonal swellings and researchers require at least two separate approaches to analyze the morphological hallmarks of AxD. Furthermore, the analytical tools are time-consuming as they are semi-automatic and include subjective evaluations. While axonal swellings are identified by manual annotations that define a region of interest, the identification of axonal fragments by image binarization includes the subjective selection of threshold filters that may result in poor sensitivity nor high specificity as axons are not binarized properly.

The detection of degenerating axons can be facilitated using high signal-to-background ratios such as in fluorescent images[7,58]. However, fluorescence itself restricts experimental flexibility as the images are either taken at single time points, or, when assessed live over time, fluorescently labeled cultures are susceptible to photobleaching and the fluorescent dye may exert toxicity after a certain incubation time.

Other approaches to quantify the axonal morphology originate from the field of deep learning[59–61]. Deep learning is increasingly applied to analyze biological imaging data, including cellular morphological changes, protein distributions within cells, or the motility of cells and their components[62]. Advantages include among others decreased time and labor as well as objectivity in the data analysis.

In the field of axonal biology, a number of deep learning tools have been developed to count the number of axons and characterize their morphology in electron microscopy images of tissue specimen[59–61]. Although these deep learning tools do not recognize the morphological hallmarks of AxD, the ability of one of the deep learning tools to distinguish subcellular neuronal compartments and to recognize organelles indicates that deep learning tools may facilitate the analysis of the morphological hallmarks of AxD[61]. Axons and their morphology can be recorded by phase-contrast microscopy at several time points[54] but so far no automatized analysis of AxD and its morphological hallmarks has been described for phase-contrast microscopic data.

1.2. AxD in intracerebral hemorrhage

1.2.1. The pathophysiology of intracerebral hemorrhage

Intracerebral hemorrhage (ICH) is a type of stroke characterized by the rupture of a brain blood vessel and subsequent bleeding into brain tissue. The hydrostatic jet of blood causes primary injury to the brain tissue (mass effect). The underlying increase of the intracranial pressure further compresses the brain and leads to brain herniation[63]. As the hematoma enlarges within the first minutes to hours[64], medical treatments include attempts to reduce the intraparenchymal hematoma volume and expansion[64–66]. However, even after surgical intervention, a residual volume of blood remains in the cavity and may lead to secondary injuries[66]. Thus, it is relevant to comprehend the pathophysiological processes underlying these secondary injuries.

The secondary injuries in ICH occur several hours to days after the insult thereby representing an attractive target for novel therapeutic strategies[67]. Secondary ICH

injuries are mediated, among others, by local hemolysis[67–69]. Hemolysis is the result of energetic and metabolic deficiency in erythrocytes through which their components are released[70]. Released ferrous hemoglobin undergoes autooxidation and/or oxidation reactions with nitric oxide forming ferric hemoglobin[71–73]. Both ferrous and ferric hemoglobin interact with peroxides forming ferric/ferryl heme iron and protein-based radicals as heme is released from both ferrous and ferric hemoglobin[73–75]. Further, ferric/ferryl heme iron and protein-based radicals interact with signaling molecules such as lipids in so-called “pseudo-peroxidase reactions” that finally result in lipid peroxidation[73].

1.2.2. The neuronal toxicity of hemin iron and AxD in ICH

As a product of hemoglobin breakdown, hemin is often used to simulate the secondary injuries of ICH *in vitro*. Several independent experiments showed that hemin treatment of neurons resulted in decreased cell viability[76–79]. However, the exact mechanisms had not been clarified until Zille et al. and Li et al. showed the involvement of the cell death mechanisms ferroptosis, necroptosis, and autophagy as the underlying molecular mechanisms of neuronal cell death in the context of ICH[79,80].

Axonal damages have also been observed in patients suffering from ICH[81,82]. The progression of axonal damages correlated with the hematoma volume[82]. In patients with deep ICH, AxD occurred mostly in the internal capsule and cerebral peduncle[81]. Both of these structure contain axons that ascend and descend from the cortex to the spinal cord[83]. Inspections of axons in animal models of ICH revealed that axons appeared compromised three days after the insult and even in some distance from the primary lesion. The amount of axons decreased after 28 days[80].

However, it remains unknown i) how hemolysis products such as hemin affect axonal morphology, and ii) what the underlying molecular mechanisms of hemin-induced AxD are.

1.3. Aims and experimental strategies

The aim of this thesis was to morphologically characterize AxD in an *in vitro* model of ICH. To overcome current limitations in the experimental setup and image analysis, we developed i) a novel microfluidic device using bioengineering approaches to separate axons from their somata in an enhanced throughput manner (aim 1) and ii) a deep learning analysis tool using supervised learning to characterize the axonal

morphology in the context of AxD (aim 2). We then used these tools to quantify the concentration- and time-dependent progression of AxD upon hemin exposure (aim 3) and the effect of chemical inhibitors of several molecular mechanisms in an attempt to rescue the axonal morphology and to understand the underlying mechanisms (aim 4) (**Fig. 7**).

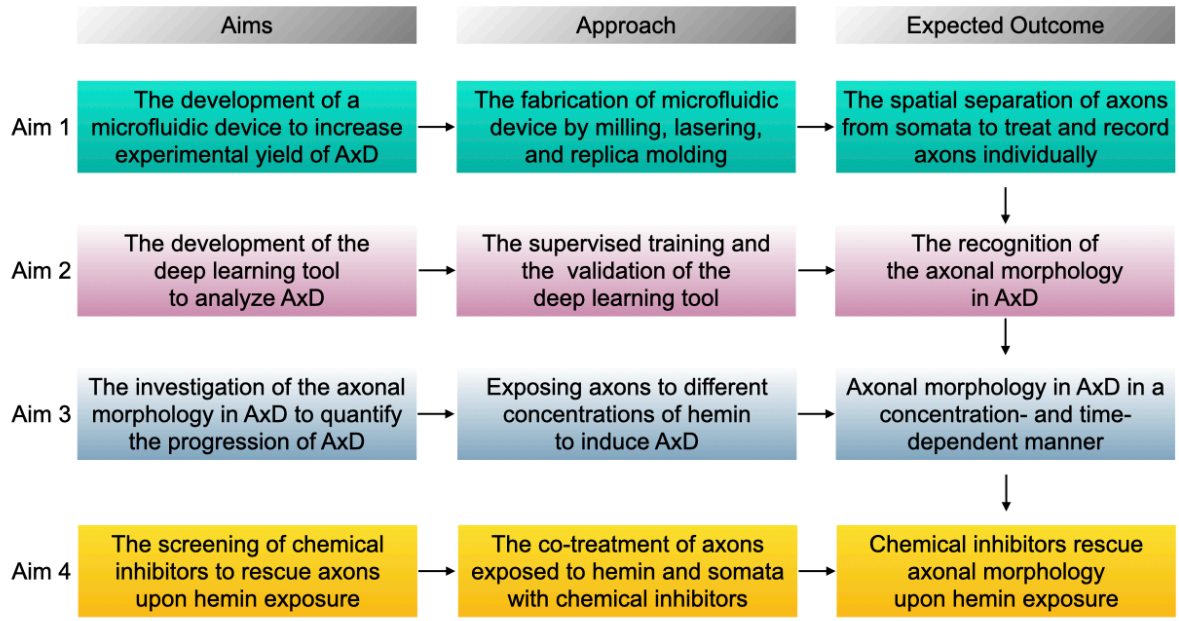

Fig. 7 The aims of the project including approaches and expected outcomes.

2. Materials and methods

2.1. Materials

Table 1 Animals

Animal	Genotype	Company
Mice	Crl:CD1 (ICR) Swiss outbred mice	Charles River

Table 2 Chemicals and reagents

Product	Company	Catalogue number
B-27™ Plus Neuronal Culture System	Thermo Fisher Scientific	A3653401
Boric acid	Merck	925K12283365
Bovine serum albumin (BSA)	Sigma Aldrich	A9418
Calcein AM	Santa Cruz	sc-203865
Chicken trypsin inhibitor	Sigma Aldrich	T9253
Cooling lubricant	Opta Cool 600 HS	Wisura GmbH
4′,6-diamidino-2-phenylindole (DAPI)	Roche	10236276001
DNAse	Sigma Aldrich	D5025-15KU
Earle's balanced salt solution (10 X) (EBSS)	Sigma Aldrich	E7510
Epoxy solution Smooth-Cast 310/1	KauPo	09202-003-000002
Ethanol 70%	Carl Roth	9065.5
Ethylenediaminetetraacetic acid	Carl Roth	8043.3
Fetal calf serum	Thermo Fisher Scientific	A15-151
Fluorescence mounting medium	Agilent/Dako	S302380-2
Hemin	Sigma Aldrich	H9039
Horse serum	GE Health Life Sciences	SH30074.03
Laminin	Sigma Aldrich	L2020
L-cysteine	Carl Roth	1693.2
Minimum Essential Medium (MEM), GlutaMAX™ Supplement	Thermo Fisher Scientific	41090028
Neurobasal™ Plus Medium	Thermo Fisher Scientific	A3582901
Normal goat serum	Biozol	VEC-S-100
Papain	Carl Roth	8933.1
Penicillin/streptomycin	Biochrom	A2212
Phosphate buffered saline (PBS)	Thermo Fisher Scientific	14200083
Polydimethylsiloxane (PDMS)	Biesterfeld Spezialchemie GmbH	5498840000
Poly-d-lysine	Sigma Aldrich	P6407
Polymethylmethacrylate (PMMA)	Kongsback	Customized
Sodium acetate	Carl Roth	X891.1
Sodium bicarbonate	Sigma Aldrich	S5761
Sodium pyruvate	Thermo Fisher Scientific	11360070
Sodium tetraborate	Merck	1.06308.1000
Triton X-100	Fluka	93420

Table 3 Chemical inhibitors

Chemical inhibitor	Concentration range [µM]	Dissolved in	Company	Catalogue number
Actinomycin-D (Act-D)	0.001-1	DMSO	Enzo Life Science	BML-GR300-0005
Ac-Leu-Leu-Nle-CHO (ALLN)	0.1-100	DMSO	Enzo	BML-P120
Bafilomycin A1 (BafA1)	0.001-0.1	DMSO	LC Labs	B-1080
Cycloheximide (Chx)	0.1-50	DMSO	Enzo Life Science	ALX-380-269-G001
Deferoxamine (DFO)	10-200	Water	Sigma Aldrich	D9533
E64d	0.1-100	DMSO	Enzo	BML-PI107
Ferrostatin-1 (Fer-1)	0.01-10	DMSO	Sigma Aldrich	SML0583
GSK872	1-20	DMSO	Merck	530389
MDL28170	0.1-100	DMSO	Enzo	BML-PI130
Mitochondrial division inhibitor-1 (Mdivi-1)	0.1-100	DMSO	Enzo Life Science	BML-CM127-0010
N-acetyl-Cysteine (NAC)	10-2000	Water	Sigma Aldrich	A7250
Necrostatin-1 (Nec-1)	1-100	DMSO	Enzo Life Science	BML-Ap309-0020
Necrostatin-1i (Nec-1i)	1-100	DMSO	Merck	480066
Necrosulfamide (NSA)	0.1-10	DMSO	Merck	480073
Trolox	0.1-100	Ethanol	Enzo Life Science	ALX-270-267-M100
U0124	0.1-10	DMSO	Merck	662006
U0126	0.1-10	DMSO	LC Labs	U-6770
z-VAD-fmk	0.1-100	DMSO	Enzo Life Science	ALX-260-020-M001

Table 4 Buffers and solutions

Buffer/solution	Ingredients
Borate buffer	0.25 % (w/v) boric acid and 0.38 % (w/v) sodium tetraborate in distilled water, pH 8.5
Blocking solution A	2 % BSA, 0.5 % Triton-X-100 in PBS
Blocking solution B	5 % normal goat serum, 0.5 % Triton X-100 in PBS
Bovine serum albumin/trypsin inhibitor solution	1 % (w/v) bovine serum albumin and 1 % (w/v) trypsin inhibitor chicken in 1 X EBSS
4% formaldehyde solution	Formaldehyde in PBS
Hemin	Dissolved in 1 M sodium hydroxide and further diluted in distilled water to obtain a 10 mM stock solution
MEM + Glutamax medium	10 % fetal calf serum, 1 % horse serum, and 1 % penicillin/streptomycin in MEM+Glutamax medium

Neurobasal Medium	2 % B-27 Plus Supplement, 1 mM sodium pyruvate, and 1 % penicillin/streptomycin in Neurobasal Plus Medium
Poly-d-lysine solution	1 mg/mL of poly-d-lysine in 0.02 M borate buffer
Papain solution	0.33 % (w/v) papain, 0.017 % (w/v) L-cysteine, 0.1 % 0.5 M ethylenediaminetetraacetic acid, 1 % sodium acetate, and 30 mL EBSS (1 X in dH_2O) and 0.22 % (w/v) sodium bicarbonate, pH 7.3

Table 5 Primary antibodies

Primary antibody	Dilution	Clone	Company	Catalogue number	RRID
Polyclonal rabbit anti-microtubule-associated protein 2 (MAP2)	1:4000	n/a	Abcam	ab32454	AB_776174
Monoclonal mouse anti-synaptophysin	1:250	SY38	Thermo Fisher Scientific	MA1-213	AB_2723681
Monoclonal rabbit anti-cleaved caspase-3	1:500	5A1E	Cell Signaling	9664S	AB_2070042
Monoclonal mouse anti-malondialdehyde (MDA)	1:100	1F83	Biomol GmbH	JAI-MND-030N	n/a
Monoclonal mouse anti-CD71 (TfR1)	1:50	3B8 2A1	Santa Cruz	sc-32272	AB_627167

Table 6 Secondary antibodies

Secondary antibody	Dilution	Company	Catalogue number	RRID
Polyclonal goat anti-mouse IgG (H+L) highly cross-adsorbed secondary antibody, Alexa Fluor 546	1:500	Thermo Fisher Scientific	A-11030	AB_2534089
Polyclonal goat anti-rabbit IgG (H+L) highly cross-adsorbed secondary antibody, Alexa Fluor 488	1:500	Thermo Fisher Scientific	A-11034	AB_2576217
Polyclonal goat anti-mouse IgG (H+L) highly cross-adsorbed secondary antibody, Alexa Fluor 488	1:500	Thermo Fisher Scientific	A-11029	AB_138404

Table 7 Equipment

Device/tool	Model	Company
Biopsy punch	130805	DocCheck Shop GmbH
Cell strainer 70 µm	734-2761	VWR International
Excimer laser	Excistar XS 193 nm	Coherent
High Power Expanded Plasma Cleaner	PDC-002-HP	Harrick Plasma
Milling machine	Mikron WF21C	Mikron Holding AG
Sonicator	Sonicator Elmasonic S	Elma Schmidbauer GmbH
Triple tooth cutter	HSS-CO8 Type N	Holex

Vacuum desiccator	VDC-31	Jeio Tech

Table 8 Microscopes

Microscope	Model	Objectives	Company
Olympus	IX81	10X (0.3 NA)	Olympus Deutschland GmbH
Leica	DMI6000 B	20X (0.4 NA)	Leica Microsystems
Zeiss	Axiovert 200	10X (0.45 NA)	Carl Zeiss AG

Table 9 Software

Sofware	Version	Company	RRID
Axiovision	4.7.0.0	Carl Zeiss AG	SCR_002677
Cell^{M}	3.1 (Build 1275)	Olympus Deutschland GmbH	n/a
GIMP	2.10.14	Free Software Foundation, Inc	SCR_003182
ImageJ	1.52a	National Institutes of Health	SCR_003070
LAS AF	2.5.0.6735	Leica Microsystems	SCR_013673
Python	3.7.3	Python Software Foundation	SCR_008394

2.2. Methods

2.2.1. The development of an enhanced-throughput microfluidic device to investigate AxD

2.2.1.1. The design of the microfluidic device

To enable the spatial separation of axons, Alessa Pabst (Fraunhofer Research Institution, Lübeck, Germany, Bachelor thesis) designed a microfluidic unit, in which both the soma and axon compartments are composed of one medium-filled well each. Both compartments are connected by microgrooves. A difference in medium filling level (microfluidic gradient) between the two compartments induces a microflow that directs axonal outgrowth from the soma compartment through the microgrooves into the axonal compartment. We modified the design to arrange 16 microfluidic units in a conventional 96-well plate format (**Fig. 8**). This allowed to increase the experimental throughput and to parallelize the cultivation and treatment of axons.

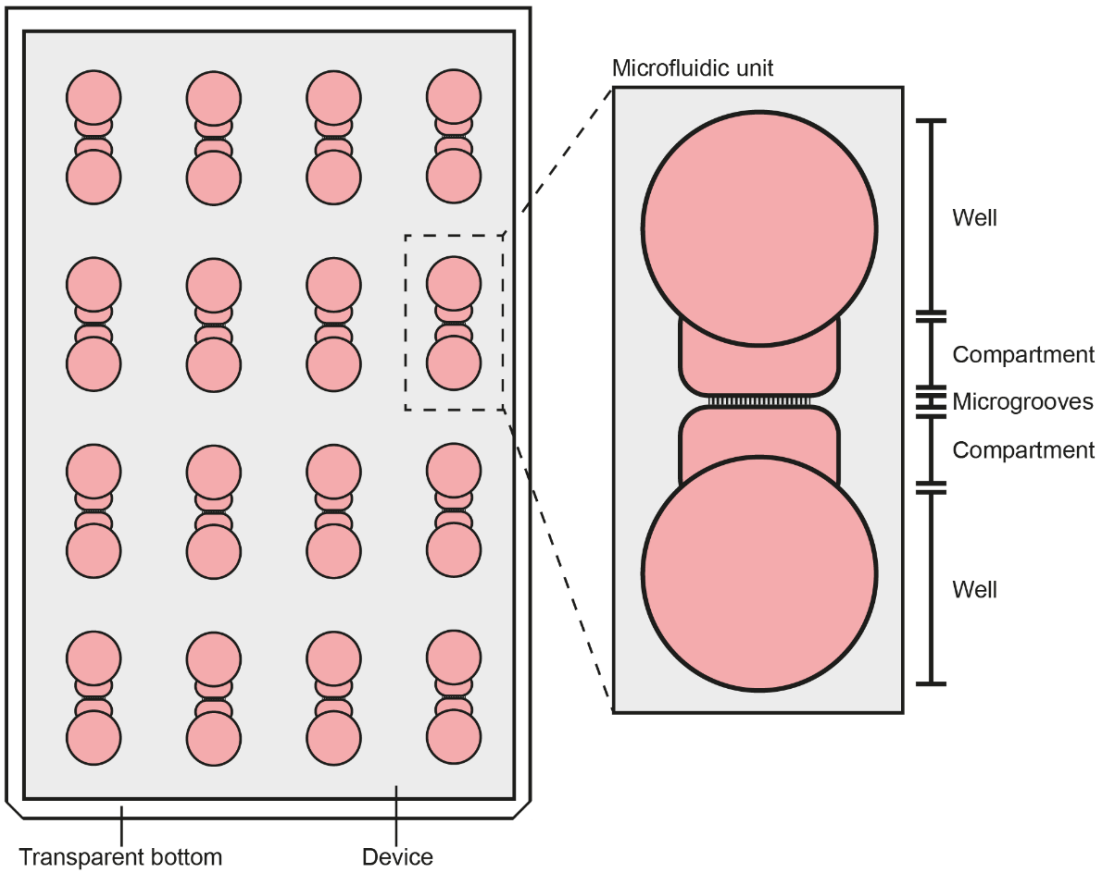

Fig. 8 The design of the microfluidic device
The microfluidic device contains 16 individual microfluidic units. Each microfluidic unit consists of two wells to establish the microflow and two compartments which are connected through microgrooves. Neurons are seeded into one compartment and axons grow into the opposite compartment through the microgrooves.

2.2.1.2. The principle of soft lithography

Soft lithography is an approach to fabricate prototypes at micro- and nanoscale. It encompasses different patterning techniques that are based on printing, molding and embossing[84]. The replica molding technique enables the fastest production of replicas by i) manufacturing a topographically patterned master, ii) transmitting the pattern of a master into a PDMS stamp and iii) transferring the structure of the PDMS stamp into a further replica mold consisting of either thermally-curable epoxy or UV-curable polyurethane[85,86].

The first two steps of the replica molding technique are usually based on photolithography to fabricate the topographically patterned master from which a PDMS stamp is casted[84]. In photolithography, a photomask containing the pattern of interest is produced and transferred on a photoresist and a silicon wafer. We combined the first two steps of the replica molding technique and transmitted the patterns of the PMMA plate directly into a negative casting mold consisting of epoxy to fabricate the microfluidic device (**Fig. 9**).

We used PDMS for the device as it is the most widely used siloxane-based elastomeric polymer in cell culture due to its transparency for microscopic recordings and biocompatibility[87–89].

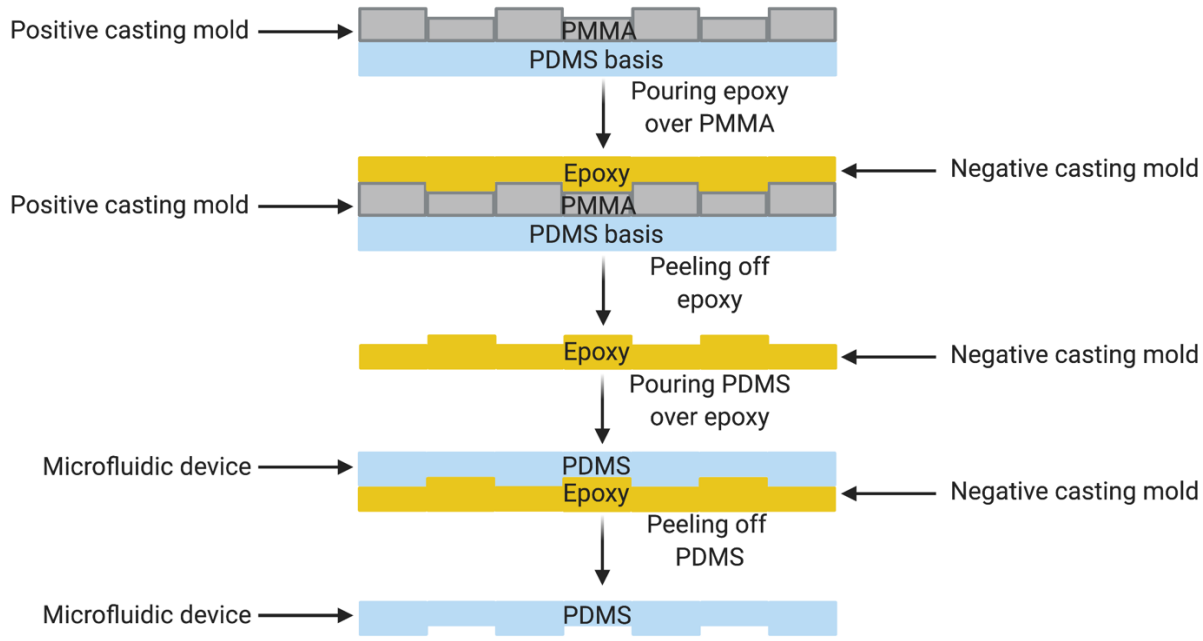

Fig. 9 The schematic of replica molding for microfluidic device development.
A PMMA plate is added onto a PDMS basis before epoxy is poured over the PMMA. Afterwards, the epoxy is peeled off and used as a negative casting mold for the PDMS to create the microfluidic device. Created with BioRender.com.

2.2.1.3. The milling and lasering procedure of a positive PMMA casting mold

Milling and lasering of the positive casting mold were performed by Reinhard Schulz (Wissenschaftliche Werkstätten, University of Lübeck, Lübeck, Germany) and Christopher Kren (Medical Laser Center GmbH, Lübeck, Germany). Then, we produced the negative epoxy casting mold from which the PDMS devices were obtained prior to bonding onto glass using oxygen plasma treatment (**Fig. 10**).

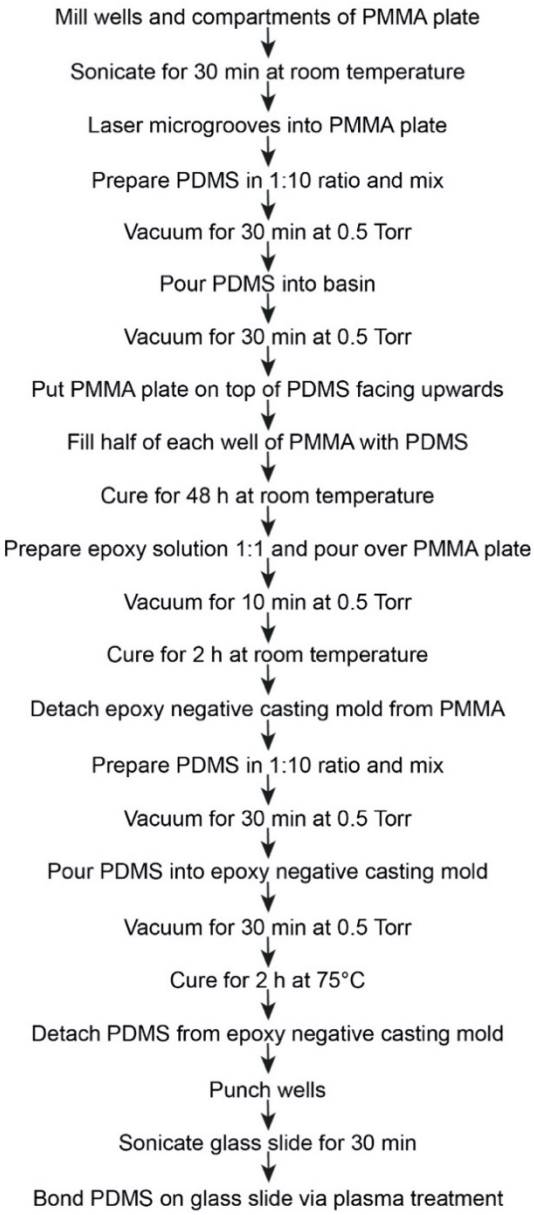

Fig. 10 The manufacturing protocol of microfluidic device.
The step-by-step fabrication protocol of the microfluidic device.

In detail, 32 wells and compartments were milled in a PMMA plate of the size of a conventional cell culture plate with a universal milling machine containing a 1 mm triple tooth cutter with 0.01 mm precision. The debris produced during the milling step was removed with a cooling lubricant followed by 30 minutes sonication in a water bath.

The microgrooves were lasered with an Excimer laser and again cleaned by sonication in a water bath for 30 minutes.

2.2.1.4. The fabrication of the negative epoxy casting mold

The milled and lasered PMMA plate was used to transfer its structures into a negative casting mold. We used epoxy for the negative casting mold as it had to be detached from both the positive imprinting template and the PDMS.

We first mixed PDMS in a 1:10 ratio and applied vacuum with a vacuum desiccator at 0.5 Torr for 30 minutes to remove air bubbles within the PDMS. After pouring the PDMS onto the bottom of a basin to function as a ground for easier detachment at a later step, we again applied vacuum for 30 minutes at 0.5 Torr. We cured the PDMS for 48 hours at room temperature and placed the PMMA on top of the PDMS with its structures facing upwards. We sealed the wells with PDMS up to the half of their height, condensed the edges of the PMMA and cured it for 48 hours at room temperature. We then prepared the epoxy solution in a 1:1 ratio and poured it into the basin covering the surface of the PMMA plate before applying vacuum for 10 minutes at 0.5 Torr to remove air bubbles. After curing the epoxy solution for two hours at room temperature, we detached the epoxy negative casting mold from the basin and PMMA plate.

The negative casting mold was then used to manufacture the microfluidic devices. As described above, we prepared a 1:10 ratio of PDMS mixture, applied vacuum for 30 minutes at 0.5 Torr and cured it for 2 hours at 75 °C after pouring the PDMS into the negative casting mold followed by vacuum application of 30 minutes at 0.5 Torr. We detached the PDMS microfluidic device from the epoxy and used an 8-mm biopsy punch (DocCheck Shop GmbH) to obtain the wells.

2.2.1.5. The oxygen plasma treatment of the PDMS for glass bonding

The PDMS microfluidic device has to be fixed to a material that serves as a ground and allows the cultivation of axons. Glass enables strong covalent bonding with PDMS as oxygen plasma treatment alters the PDMS surface by oxidizing methyl groups on the PDMS surface ($CH_3[Si(CH_3)_2O]nSi(CH_3)_3$) into silanol groups (Si–O–H)[90–92].

Before plasma treatment, we washed customized 115 x 78 x 1 mm glass slides with water and ethanol to remove polar and apolar compounds that may inactivate the glass prior to plasma treatment. We exposed the glass slides and the microfluidic device to

plasma inside a High Power Expanded Plasma Cleaner for 2 minutes at 45 W and 0.5 Torr to enable the attachment of the activated silanol groups onto glass.

2.2.1.6. The coating of the PDMS microfluidic devices

Next, we rinsed the microfluidic units with ethanol and water and coated the compartments with 0.1 mg/mL of poly-d-lysine solution in 0.02 M borate buffer at 4°C overnight. Then, we aspirated the poly-d-lysine solution and re-coated the surface with 50 µg/mL of laminin at 4°C overnight.

2.2.2. The cultivation and treatment of axons *in vitro*

The general experimental strategy consisted of exposing axons of primary cortical neurons to the hemolysis product hemin alone or in combination with chemical inhibitors of several molecular cell death mechanisms for 24 hours at day *in vitro* (DIV) 6/7. The morphological changes were analyzed with a deep learning tool that was trained to recognize axons and the morphological hallmarks of AxD (**Fig. 11**).

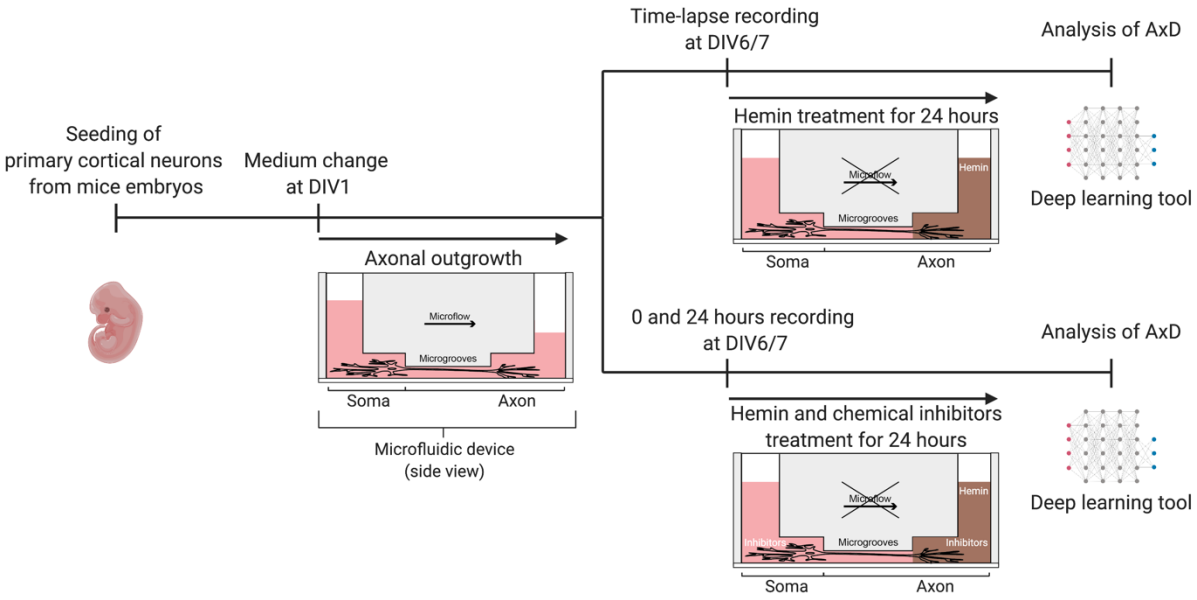

Fig. 11 Experimental design and strategy.
Primary cortical neurons from mouse embryos were seeded into the microfluidic device. In the following six to seven days in culture, axons were separated from their somata due to a microflow that directs axonal growth. Axons were treated for 24 hours with either hemin alone or in combination with chemical inhibitors. AxD analysis was performed using a deep learning tool that was trained to recognize axons and the morphological features of AxD**.** Image courtesy: Marietta Zille. Created with BioRender.com.

2.2.2.1. Experimental animals

We used Crl:CD1 (ICR) Swiss outbred mice kept at 20-22 °C and 30-70 % humidity in a 12-hours/12-hours light/dark cycle. Animals were fed *ad libitum* with standard diet

(Altromin Spezialfutter GmbH). The Schleswig-Holstein Ministry for Energy Transition, Agriculture, Environment, Nature and Digitalization approved the animal experiments (animal license number: 2017-07-06 Zille), and the “NIH Guide for the care and use of laboratory animals” was applied.

2.2.2.2. The isolation and culture of primary cortical neurons

We sacrificed the dam by cervical dislocation and removed the embryos as described previously[79] at embryonic day 14. The isolated cortical hemispheres were chilled in PBS on ice prior to digestion in CO_2-saturated papain solution for 20 minutes at 37 °C. Afterwards, we pipetted the brain tissue carefully up and down and added DNAse (1 mg/mL) for 3 minutes at 37 °C. After spinning down at 250 x g for 5 minutes, we resuspended the pellet in bovine serum albumin/trypsin inhibitor solution diluted 1:10 in EBSS and added a second layer of undiluted bovine serum albumin/trypsin inhibitor solution. We centrifuged again at 250 x g for 10 minutes and resuspended the pellet in MEM + Glutamax medium. To remove undissociated cellular components, myelin, and debris, we filtered the cell suspension with a 70 µm cell strainer.

Prior to cell seeding, we aspirated the laminin, rinsed the microfluidic units twice with medium and removed the medium only from the wells. Primary cortical neurons were seeded into the soma compartment of each microfluidic unit of the device at a density of 10,000 cells/mm^2 in MEM + Glutamax medium. After allowing the primary cortical neurons to adhere on the surface for 30 minutes at 37 °C, we induced the microflow to promote axonal growth into the axonal compartment by applying 150 µL of MEM + Glutamax medium into the soma compartment and 100 µL of MEM + Glutamax medium into the axonal compartment. Culturing conditions were 37 °C in a humidified 5 % CO_2 atmosphere. The next day, we replaced the medium by Neurobasal Medium keeping the respective volume differences for microflow. For long-term cultivation experiments, the medium was exchanged every three to four days.

2.2.2.3. The selection of microfluidic units for treatments

We investigated AxD at six or seven days in culture as axons had grown i) through at least 80 % of all microgrooves and ii) at least approximately 150 µm into the axonal compartment. The microfluidic units were randomly selected and all further analyses were done in a blinded fashion.

2.2.2.4. Immunofluorescence

Immunofluorescence stainings were performed i) to confirm axonal outgrowth using primary antibodies targeting synaptophysin and microtubule-associated protein (MAP) 2 as axonal and dendritic markers, respectively[93,94] (together with Svenja Kim Landt, Fraunhofer Research Institution), and ii) to investigate the expression of markers of apoptosis (cleaved caspase-3), and ferroptosis (malondialdehyde (MDA) and transferrin receptor 1 (TfR1)).

Axonal outgrowth was stained as follows. After removing the culture medium at DIV 7, microfluidic units were fixed with 4 % formaldehyde solution in PBS for 1 hour at room temperature followed by two washing steps with PBS. Next, blocking solution A was applied on the microfluidic units for 1 hour at room temperature. Afterwards, the microfluidic units were incubated with the primary antibodies synaptophysin (1:250) and MAP2 (1:4000) overnight at 4 °C.

Cell death-specific markers were stained as follows. Prior to immunofluorescence staining, axons were treated with 100 µM hemin for 2, 4, 8, 16, and 24 hours at DIV 7. After treatment, we fixed all microfluidic units with either 4 % formaldehyde in PBS at room temperature (cleaved caspase-3) or methanol at -20 °C (MDA and TfR1) for 30 minutes each. After rinsing the axons twice with PBS, we incubated the wells with either blocking solution A for cleaved caspase-3 or blocking solution B for MDA and TfR1 for 1 hour at room temperature. We stained for cleaved caspase-3 (1:500), MDA (1:100), and TfR1 (1:50) in the microfluidic units overnight at 4 °C.

The following day, the microfluidic units were washed three times with PBS and the secondary antibodies goat anti-mouse Alexa Fluor 546 (1:500) and goat anti-rabbit Alexa Fluor 488 (1:500) were added for 1 hour at room temperature. After removing the secondary antibodies by washing three times with PBS, the nuclei of the cells were stained with DAPI (1 µg/mL) for 10 minutes at room temperature. Prior to fluorescence microscopy, the microfluidic units were washed three times with PBS. We used four biological replicates to determine the expression of the cell death markers.

2.2.2.5. The validation of the cleaved-caspase 3 antibody

We treated the somata with staurosporine for 9 hours to induce apoptosis (300 nM). After treatment, we followed the staining protocol for the cleaved-caspase 3 antibody as described in **section 2.2.2.4**. We used four biological replicates to validate the expression of the cleaved-caspase 3 antibody upon staurosporine treatment.

2.2.2.6. Live cell staining for long-term cultivation and the time window of AxD

We used calcein acetoxymethyl (AM) to evaluate axonal vitality. Calcein AM is non-fluorescent and passes through the plasma membrane of living cells[95]. In the cytoplasma, calcein AM is cleaved by esterases and is converted to a green-fluorescent molecule[95], which is retained by intact cell membranes.

We washed the axonal compartment once with PBS and incubated it with calcein AM (4 µM) for 30 minutes at 37 °C at DIV 7, DIV 11, DIV 15, DIV 22, DIV 29 or in four-hour intervals over 24 hours upon hemin treatment. We used three biological replicates for the confirmation of axonal vitality with calcein AM.

2.2.3 The *in vitro* model of hemin-induced AxD

We exposed axons to 0 (vehicle), 50, 100, and 200 µM of hemin to mimic the secondary ICH injuries induced by hemolysis products. These concentrations lie in the range of those applied in previous studies investigating the effects of hemin on neurons[79]. The treatment was performed by diluting hemin to its final concentration in conditioned medium. The diluted hemin was then added to the axonal compartments at the same volume as the soma compartment to block the microflow (**Fig. 12**).

To investigate the molecular mechanisms underlying hemin-induced AxD, we applied different chemical inhibitors of cell death pathways that were diluted in conditioned medium at different concentrations (**Table 3**) on both compartments of the microfluidic units, while exposing only the axonal compartment to hemin (**Fig. 12**). For each concentration, we used six biological replicates for the time-lapse recordings and the screening of the chemical inhibitors.

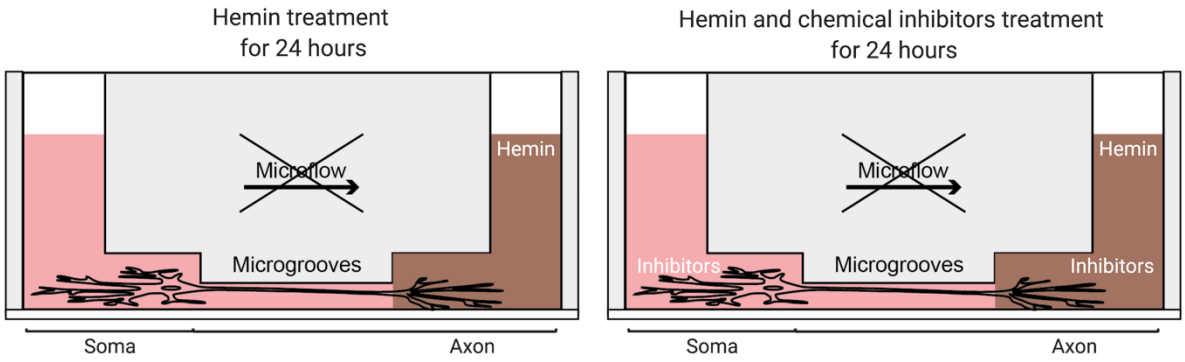

Fig. 12 AxD induction in an *in vitro* model of ICH.
Hemin is applied to the isolated axons in the axon compartment for 24 hours to induce AxD in context of ICH (left panel). Isolated axons are exposed to hemin for 24 hours, somata and axons are simultaneously treated with chemical inhibitors of cell death pathways (right panel). Image courtesy: Marietta Zille. Created with BioRender.com.

2.2.4. The recording of hemin-induced AxD

We recorded the microfluidic units using time-lapse microscopy to quantify the morphology of AxD upon hemin treatment (together with Charlotte Flory, Fraunhofer Research Institution, Lübeck, Germany). After pre-incubating the microfluidic device in the incubation chamber of the microscope at 37 °C, 5 % CO_2, and 65 % humidity and after adjusting individual positions, we recorded the axons over 24 hours in 30-minutes intervals using an Olympus IX81 time-lapse microscope equipped with a 10X objective (0.3 NA Ph1). Images were acquired with the Cell^M software.

To investigate the molecular mechanisms of hemin-induced AxD, images were taken immediately (0 hours) and at 24 hours using the Zeiss Axiovert 200 microscope with a 10X objective (0.45 NA Ph1) using the Axiovision software.

2.2.5. The analysis of AxD in ICH

2.2.5.1. The image binarization of phase-contrast microscopic images of AxD

Currently, the analysis of AxD in phase-contrast microscopy predominantly relies on the binarization of images with ImageJ[54,57]. However, the accuracy of image binarization depends on the employed processing steps. For our dataset, we established a protocol to binarize phase-contrast microscopy images of hemin-treated axons. We extracted images at 0 and 24 hours and converted them to 8-bit. Next, we applied the "find edges"-processing tool to recognize the edges of the axons, applied the "Phansalkar" local auto-threshold, a specific threshold for low-contrast images such as phase-contrast images[96].

2.2.5.2. Deep learning approach to analyze AxD in ICH

2.2.5.2.1. The basic principle of a convolutional neural network

In biology, convolutional neural networks (CNNs) are often applied to objectively analyze microscopic images by extracting information from those images[62]. This is based on training during which the CNN encounters selected microscopic images that contain the information to be analyzed (supervised learning)[62,97]. A validation dataset, containing images that the CNN has never been exposed before, is used to assess the performance of the CNN[62].

CNNs are based on fully-connected artificial neurons. They are composed of different layers (input, hidden, and output layers), in which each neuronal information is propagated and integrated by the successive neuron[62,98,99] (**Fig. 13**).

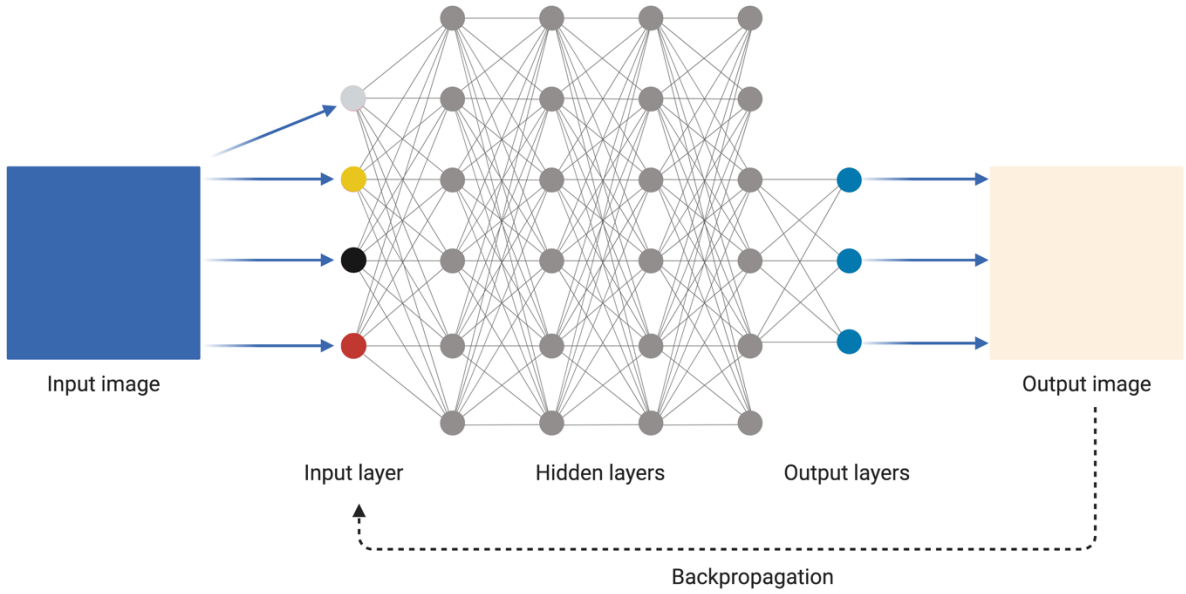

Fig. 13 The principle of a CNN.
The input layer extracts the features of the input image and forwards this information to the hidden layers. The hidden layers extract further information and propagate them to the output layers that generate an output image. In case the output image does not correspond to the input image, backpropagation corrects the connection among the layers. Created with BioRender.com.

Each artificial neuron in the input layer is generated by a convolutional filter (kernel) that is applied to the input image in a defined stride to extract features and thereby to produce a feature map with width and height of the corresponding image (convolution)[62,100]. Depending on the task and the features of interest, the number of feature maps, and consequently the depth dimension, may vary. All feature maps, originating from different kernels, are finally stacked together to generate a feature map with a greater depth. The dimensions of the feature map (width and height, but not depth) are then reduced via pooling giving rise to a hidden convolutional layer[98,101]. The processes of convolution and pooling are then repeated for each hidden convolutional layer. Therefore, the number of hidden layers in the CNN represents the depth of the neural network and its ability to extract features for an output.

The output prediction of a CNN is generated by an output layer, i.e., a “final” layer of neurons that summarizes the signals of the former layers[97]. In case the resulting output prediction does not match the input image, the CNN uses so-called backpropagation to correct the weights of the neurons in each layer starting with the layer closest to the output and propagating towards the input layer[97].

Each iteration, i.e., the process from presenting an input image to the CNN until the step of backpropagation, is called an epoch. As the performance of the CNN to predict the training data is limited to a number of epochs, data augmentation is often employed[102]. To further strengthen the performance of neural networks, it is possible

to combine several individual networks to function as an ensemble[103]. The ensemble represents a greater diversity in the capacity of predicting the correct outcome by incorporating several individual CNNs.

The depth of a CNN characterizes its ability to perform even more complex tasks such as the recognition of axonal morphology[61]. However, the network depth cannot be increased infinitely due to the so-called vanishing gradient problem, which describes the ineffectiveness of changing the weights and biases leading to increased training and testing errors[104]. Residual Networks (ResNets) are considered as a solution to this limitation as they contain "identity shortcut connections" that skip various layers and prevent the vanishing gradient[104,105]. Therefore, ResNets are more reliable in the context of backpropagation, in particular in very deep networks.

2.2.5.2.2. The training of the EntireAxon CNN for axon segmentation and classification

Philipp Grüning (Institute for Neuro- and Bioinformatics, University of Lübeck, Lübeck Germany) developed an ensemble of eight CNNs, called the "EntireAxon CNN", by modifying a u-net architecture with a ResNet-50 encoder[106]. With the assistance of Luisa Bartram (Fraunhofer Research Institution, Lübeck, Germany), we trained the EntireAxon CNN to automatically determine the class probability for each pixel of an input image. The EntireAxon assigned every pixel of a phase-contrast image to one of the following four classes: 'background', 'axon', 'axonal swelling', and 'axonal fragment' (**Fig. 14**).

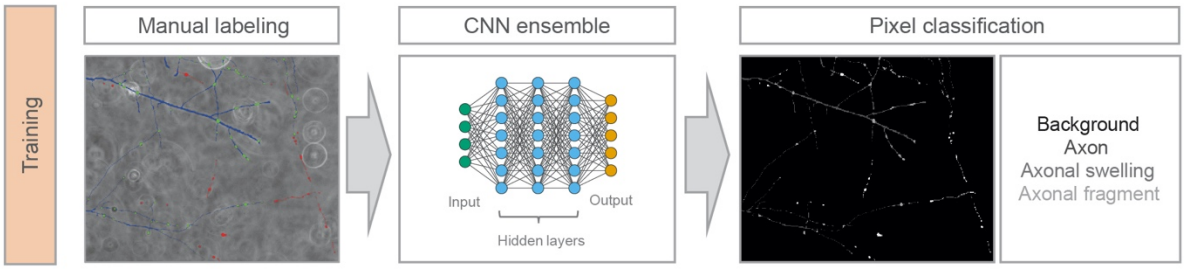

Fig. 14 The training of the EntireAxon CNN.
The training dataset was manually labeled to segment each pixel and the EntireAxon CNN ensemble was trained to recognize the four classes 'background', 'axon', 'axonal swelling', and 'axonal fragment'. It generated output images representing each class (black = 'background', dark grey = 'axon', intermediate grey = 'axonal swelling', and light grey = 'axonal fragment').

The training dataset consisted of 33 images (1376 x 1038 pixels) that were manually labeled by Svenja Kim Landt via GIMP. Each pixel was assigned one of the four classes with the values 0, 1, 2, and 3 for 'background', 'axon', 'axonal swelling', and

'axonal fragments', respectively. The EntireAxon CNN calculated the probability distribution for each pixel over all four classes to generate a segmentation output map according to the most probable class that is compared with the input image via backpropagation. We trained eight neural networks for 180 epochs with a batch size of four, an adam optimizer, and a learning rate of 0.001 that decreased by a factor of ten after every 60 epochs. We applied data augmentation (random cropping, image flipping, and rotation)[102]. The mean ensemble of the eight neural networks was used to assign the most probable class to each pixel of the images.

2.2.5.2.3. The validation of the EntireAxon CNN performance and comparison to human evaluators

To evaluate the performance of the trained EntireAxon CNN, we utilized a validation dataset of eight images that was not presented to the EntireAxon CNN before. Three trained human evaluators (Svenja Kim Landt, Lara Eleen Heckmann, Fraunhofer Research Institution, Lübeck, Germany, and I) each generated a labeled mask for the eight images. It is noteworthy that the EntireAxon CNN did not additionally learn during the validation and that its performance solely relied on the learning process during the training (**Fig. 15**).

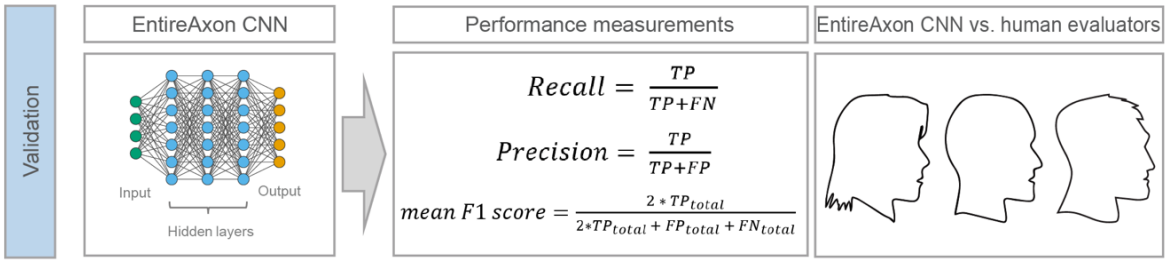

Fig. 15 The validation of the EntireAxon CNN.
A validation dataset was employed to assess the performance (recall, precision, and mean F1 score) of the EntireAxon CNN and to compare it to three human evaluators.

The EntireAxon CNN predicted a segmentation for each image to generate a binary mask, in which only one value was assigned to a specific class. The binary label mask from each human evaluator was generated the same way. To compare their performance with that of the EntireAxon CNN, we determined true positive (TP), false positive (FP), and false negative (FN) pixels, and calculated the recall (sensitivity) and precision as follows[107]:

$$\text{Recall} = \frac{TP}{TP+FN} \quad (1)$$

$$\text{Precision} = \frac{TP}{TP+FP} \quad (2)$$

We computed the recall and precision for each class in every validation image and determined the mean recall and precision over all eight validation images. The class distributions in our dataset were imbalanced as the classes 'background', 'axon', 'axonal swelling', and 'axonal fragment' covered the image area by 96.42 %, 2.77 %, 0.58 %, and 0.23 %, respectively. Since this imbalance may affect recall and precision[107], we computed the mean F1 score as a harmonic mean of recall and precision. We counted the total TP, FP, and FN of all validation images to calculate the mean F1 score as follows[107]:

$$\text{mean F1 score} = \frac{2 * TP_{total}}{2*TP_{total} + FP_{total} + FN_{total}} \quad (3)$$

In addition, we conjugated the individual masks of all three human evaluators to generate consensus labels between human evaluator 1 and 2, 2 and 3 as well as 1 and 3 to compare the EntireAxon CNN against the human evaluator missing in the consensus label (human evaluator 3, 1 and 2, respectively) based on the consensus label. We computed the mean F1 scores for all classes as described above.

2.2.5.2.4. The image preprocessing prior to AxD analysis

Yamil Abdala Villanueva Maluje (Fraunhofer Research Institution, Lübeck, Germany) and I preprocessed all acquired images using ImageJ with a custom-written macro, in which we converted the images to 8-bit and aligned them subsequently. Using the ImageJ plug-in "Linear Stack Alignment with SIFT" as described previously[108], we aligned each stack with the following settings listed as they appear in the software: "an initial Gaussian blur of 1.6 pixel", "3 steps per scale octave", "minimum image size of 64 pixel", "maximum image size of 1024 pixel", "feature descriptor size of 4", "8 feature descriptor orientation bins", "closest/next closest ratio of 0.92", "maximal alignment error of 25 pixel; inlier ratio of 0.05", "expected transformation as rigid", ""interpolate" and "show info" checked" (order of setting is copied from ImageJ). We finally cropped the images to exclude black edges appearing after the alignment.

2.2.5.2.5. The application of the EntireAxon CNN to analyze AxD

We applied the EntireAxon CNN to analyze the extent of AxD by classifying each pixel to one of the four classes 'background', 'axon', 'axonal swelling', and 'axonal fragment'. The EntireAxon CNN calculated the sum percentage of all pixels per class at the corresponding experimental day at each time point ($Axon_{tbaseline}$–$Axon_{t24h}$, $Axonalswelling_{tbaseline}$-$Axonalswelling_{t24h}$, $Axonalfragment_{tbaseline}$-$Axonalfragment_{t24h}$) and for each experimental condition (i.e., hemin and chemical inhibitor concentration). The changes of each class over time were calculated to assess the progression of AxD. The EntireAxon CNN calculated the sum percentage of pixels for all given time points (t_i with i = baseline to 24 hours) of the corresponding class over the sum of the pixels of all three classes at baseline as follows[109]:

$$\text{normalized 'class' area } (t_i) = \frac{\text{'Class'}_{ti}}{Axon_{tbaseline}+Axonalswelling_{tbaseline}+Axonalfragments_{tbaseline}} * 100 \quad (4).$$

2.2.5.2.6. The basic principle of a recurrent neural network

We observed in time-lapse recordings that axons underwent four different morphological patterns during AxD. The analysis of these morphological patterns requires an approach that considers the temporal aspect as the information seen in each image is connected with that seen in the previous and following one.

However, CNNs rely mainly on the assumption that images are independent from each other and therefore they cannot interpret temporal information from a sequence of images[110]. In contrast, recurrent neural networks (RNNs) perform the same computation for each step in every image of a sequence on which the output of the following image of a sequence depends[110,111]. The "internal memory" of an RNN is typically enabled by two different recurrent units, either a long short-term memory unit or Gated Recurrent Unit that have been established to prevent the vanishing gradient problem in RNNs[112–114].

2.2.5.2.7. The classification of the morphological patterns of AxD using an attention-based RNN

We defined each of the four morphological alterations as a morphological pattern of AxD. In collaboration with Philipp Grüning, we used the segmentation masks of the time-lapse recordings to classify the four morphological patterns of AxD: i) granular, ii) retraction, iii) swelling, and iv) transport degeneration (**Fig. 16**).

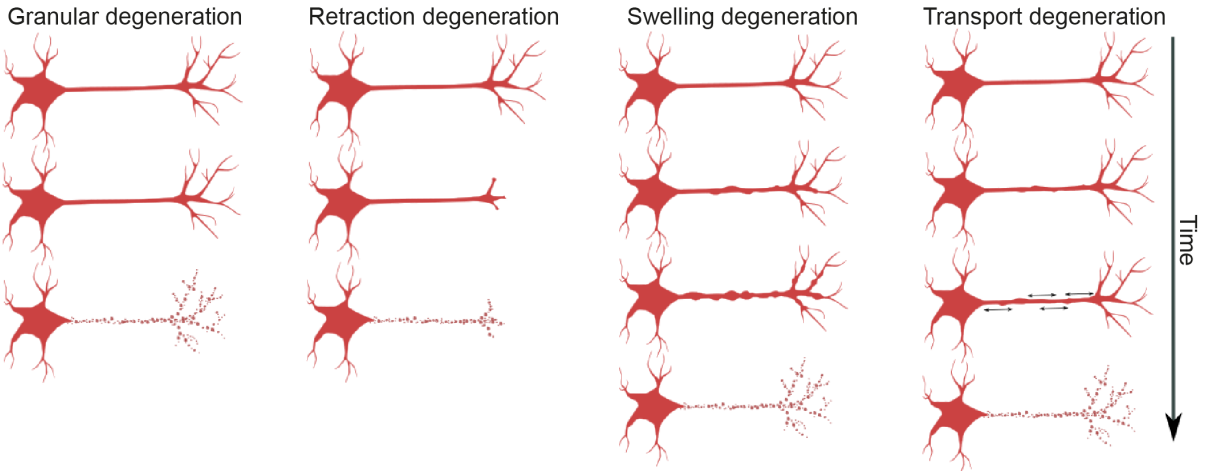

Fig. 16 Schematic illustrations of the four morphological patterns of AxD
Each morphological pattern of AxD undergoes different morphological changes over time that result in axonal fragments. Image courtesy: Maulana Ikhsan.

We trained the EntireAxon RNN with 162 images for 60 epochs applying the lamb optimizer[115] with a batch size of 128. The initial learning rate of 0.01 was decreased by a factor of ten after every 15 epochs with an additional weight decay of 0.0001. Furthermore, Philipp Grüning applied dropout with a *P*-value of 0.9 for all Gated Recurrent Units that consisted of three layers. As axon thickness varied in our training dataset, we used erosion with a cross-shape as kernel in various sizes (three, five, and seven) in the segmentation data to obtain the original training image at a 50 % probability. Six versions of each image (three eroded versions and three unchanged copies) were generated.

2.2.5.2.8. Ten-fold cross-validation of the RNN

The performance of the RNN was validated by Phillip Grüning applying ten-fold cross-validation[100]. Ten separate validation datasets (nine sets consisting of 17 images and one set containing nine images) were extracted from the overall 162 training images. The RNN was trained ten times, each time using nine of the datasets and the remaining dataset was used to compute the recall, precision, and F1 score for each set. The mean recall, precision, and F1 score were then calculated as described above in **section 2.2.5.2.3**.

2.2.5.2.9. The application of the EntireAxon RNN to analyze the morphological patterns of AxD

The segmentation masks of the time-lapse recordings were automatically analyzed in a pixel-wise manner by the EntireAxon RNN to quantify the appearance of the four

different morphological patterns of AxD after hemin treatment. A pixel can belong to none, one, or multiple morphological patterns. Only the pixels classified as 'no-background pixels' that changed to pixels of the classes 'axonal fragments' or 'background' over time were considered for the "fragmentation mask". For each experimental condition (i.e., hemin concentration), the percentage of the occurrence of each morphological pattern was calculated as follows[109]:

$$'morphological\ pattern'[\%] = \frac{\sum \text{pixel of morphological pattern}_i}{\sum \text{pixel no background}\rightarrow\text{background or fragments}} * 100 \quad (5).$$

2.2.6. The analysis of the expression of cell death markers

To assess the occurrence of cell death markers, Yamil Abdala Villanueva Maluje pre-processed the immunofluorescent and corresponding phase-contrast images as described in **section 2.2.5.2.4.**. The phase-contrast images were binarized with the "default" auto-threshold and despeckled three times in ImageJ. Masks of the axons were generated and the area measured. Next, the masks were applied on the corresponding immunofluorescence images that were binarized either with the "Li" (caspase-3 and MDA) or with the "default" (TfR1) auto-threshold before the area covered by the immunofluorescent signal was measured. The percentage of area covered in the immunofluorescence images compared to the axon mask of the phase-contrast images was calculated and normalized to vehicle or 0 hours.

2.2.7. Statistical analysis

The statistical analyses were performed by Marietta Zille (Institute for Experimental and Clinical Pharmacology and Toxicology, University of Lübeck) with IBM SPSS version 23 and GraphPad Prism version 8 (for linear regressions only). Since this project aimed to examine the effects of hemin on AxD and the underlying molecular mechanisms as an exploratory study, an *a priori* power analysis has not been conducted.

Normality was assessed using the Kolmogorov-Smirnov test, variance homogeneity by the Levené test, and sphericity by the Mauchly test. In case the data fulfilled prerequisites for parametric testing (normal distribution and variance homogeneity), two groups were compared using Student's t test and multiple comparisons were performed by one-way ANOVA followed by the Bonferroni *post hoc* test. When only two groups were analyzed and the data was nonparametric, the Mann-Whitney U test

was performed. For multiple comparisons of independent groups with nonparametric data, the Kruskal-Wallis test followed by the Mann-Whitney U post hoc test was conducted. As multiple testing causes the inflation of type I error, α-correction according to Bonferroni was additionally performed. The data of the repeated testing with covariates were assessed for statistical significance with repeated measures ANOVA following Greenhouse-Geisser adjustment in case sphericity was violated. Linear regressions were used to examine the correlation between hemin concentration and the AxD patterns.

Parametric data are shown as means, while nonparametric data are presented as medians. All data include ± 95 % confidence interval (CI), if not indicated otherwise. Statistical significance was set at $P < 0.05$. Statistical significance of the Kruskal-Wallis test followed by the Mann-Whitney U *post hoc* test was set as $P = 0.05/k$, in which k represents the number of single hypotheses. For AUC analyses that included three comparisons among all concentrations, i.e., $\alpha = 0.0167$ was regarded as statistically significant. For the comparison of the linear regression slopes of the four AxD patterns, $K = 6$ and hence $\alpha = 0.0083$ was regarded as statistically significant. For the analyses of the chemical inhibitors, $\alpha = 0.0125$ was regarded as statistically significant. The analysis of the contingency table for comparing the protective effects of the chemical inhibitors was performed using Fisher's exact test.

3. Results

3.1. The development of tools to study AxD *in vitro*

3.1.1. The parallel and enhanced-throughput spatial separation of axons from their somata by a novel microfluidic device

Microfluidic devices allowing to separate axons from their somata have been manufactured to investigate isolated axons[49]. As each of these devices represents an individual system, they do not allow to assess multiple experimental conditions in parallel.

We developed a monolithic microfluidic device containing 16 individual microfluidic units (**Fig. 17a**). The process involved milling and lasering the structures into a PMMA plate that was subsequently used to fabricate an epoxy negative casting mold. The epoxy negative casting mold contained all structures to manufacture the microfluidic device. The microfluidic units were arranged in equal distances among each other and to the edges of the device. This allowed not only to parallelize the cultivation and treatment of somata and isolated axons *in vitro* but also to automatize the microscopy as the recording settings need to be adjusted only once and can subsequently be used immediately.

We were able to demonstrate the successful spatial separation of axons of primary cortical neurons from their somata (**Fig. 17b**). The neurites in the soma compartment were MAP2-positive, a marker for dendrites, while in the axonal compartment only synaptophysin-positive neurites, indicating axons, were detected. Furthermore, DAPI staining revealed that the microfluidic device was tightly bonded onto the glass as no cells passed through the microgrooves to the axonal compartment.

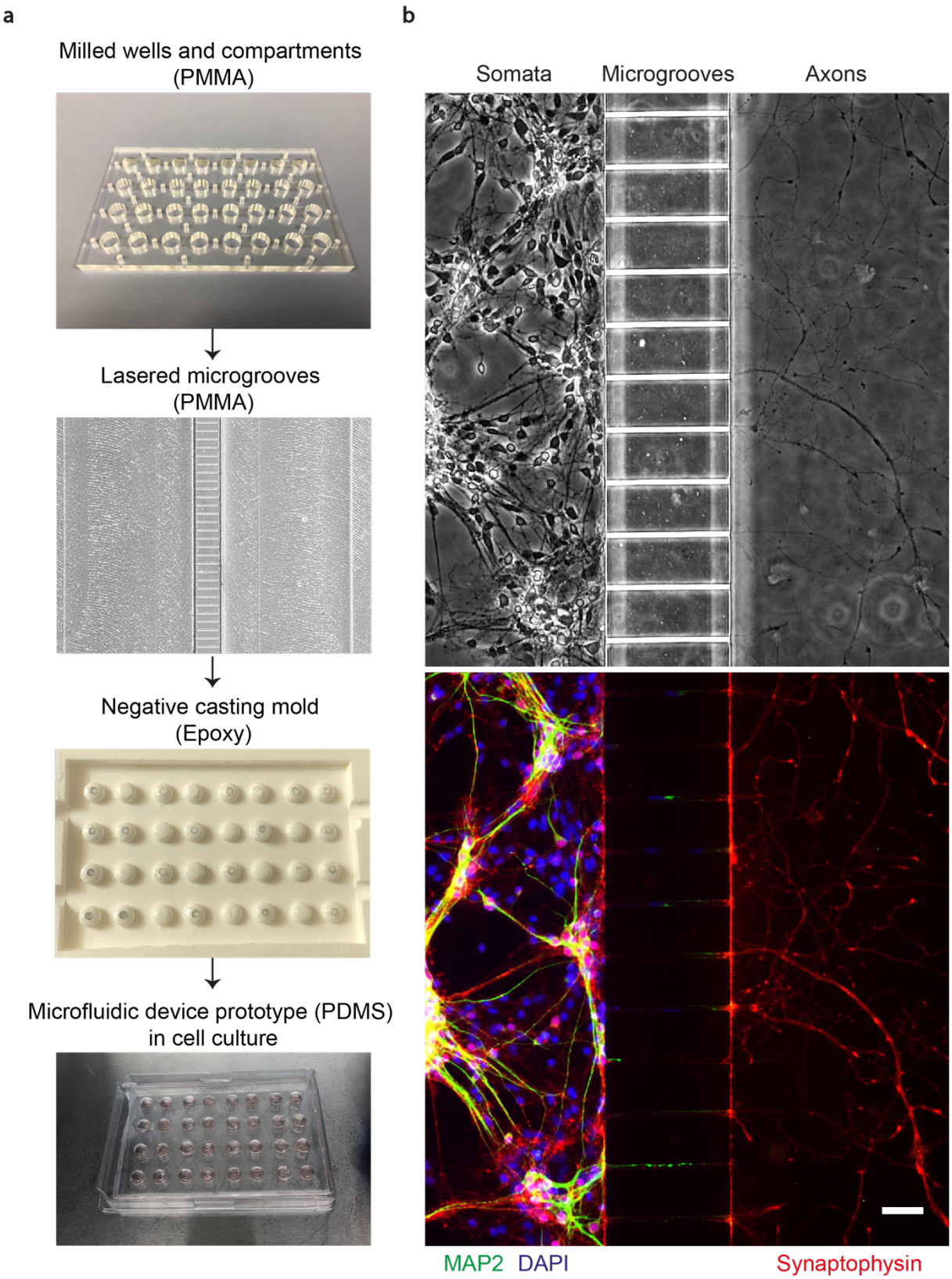

Fig. 17 The fabrication of the microfluidic device to spatially separate axons from their somata. **a**, Manufacturing steps of the development of the microfluidic device for cell culture application. **b**, Phase-contrast image (top) and immunofluorescence staining (bottom) of isolated axons at DIV 7. Axons were spatially separated from their somata by growing through the microgrooves along the microflow. MAP2 (green) and synaptophysin (red) were used as dendritic and axonal markers, respectively. Nuclei were stained with DAPI (blue). Scale bar = 50 µm. Image courtesy: Svenja Kim Landt (phase-contrast and fluorescence images).

To determine how long isolated axons can be cultivated, we examined axonal vitality up to DIV 29 with calcein AM (**Fig. 18**). At DIV 7, axons appeared morphologically intact. The axons were of different thickness and each possessed an axonal growth cone on the distal end and some axonal swellings in the axonal shaft. The axonal growth cones also contained very bright calcein AM signals. Calcein AM was taken up by all axons. At DIV 11 and DIV 15, the axonal morphology was more aberrated. Specifically, the edges of the axons were less smooth. Moreover, the axons were more punctate representing axonal swellings. At DIV 22 and 29, axons continued to grow into network-like structures. Axons tended to be thicker especially in close proximity to the microgrooves. The distal parts of the axons showed signs of degeneration, in particular axonal fragmentation. Despite the accumulation of calcein AM in the thicker and more numerous axons near the microgrooves, the calcein AM signal faded towards the distal part of the axons. At DIV 22 this effect was only detected in singular axons. However, many distal regions of axons were not stained with calcein AM one week later (DIV 29).

In summary, the microfluidic device allowed the spatial separation of axons from their somata and prevented cells of the soma compartment to enter the axon compartment. Although axons grew out and were stained with calcein AM until DIV 29, qualitative evaluation revealed that axons sometimes show axonal swellings starting from DIV 11. Thus, we decided to perform the experiments at DIV 7 or even earlier as soon as axons had grown through at least 80 % of microgrooves into the axonal compartment.

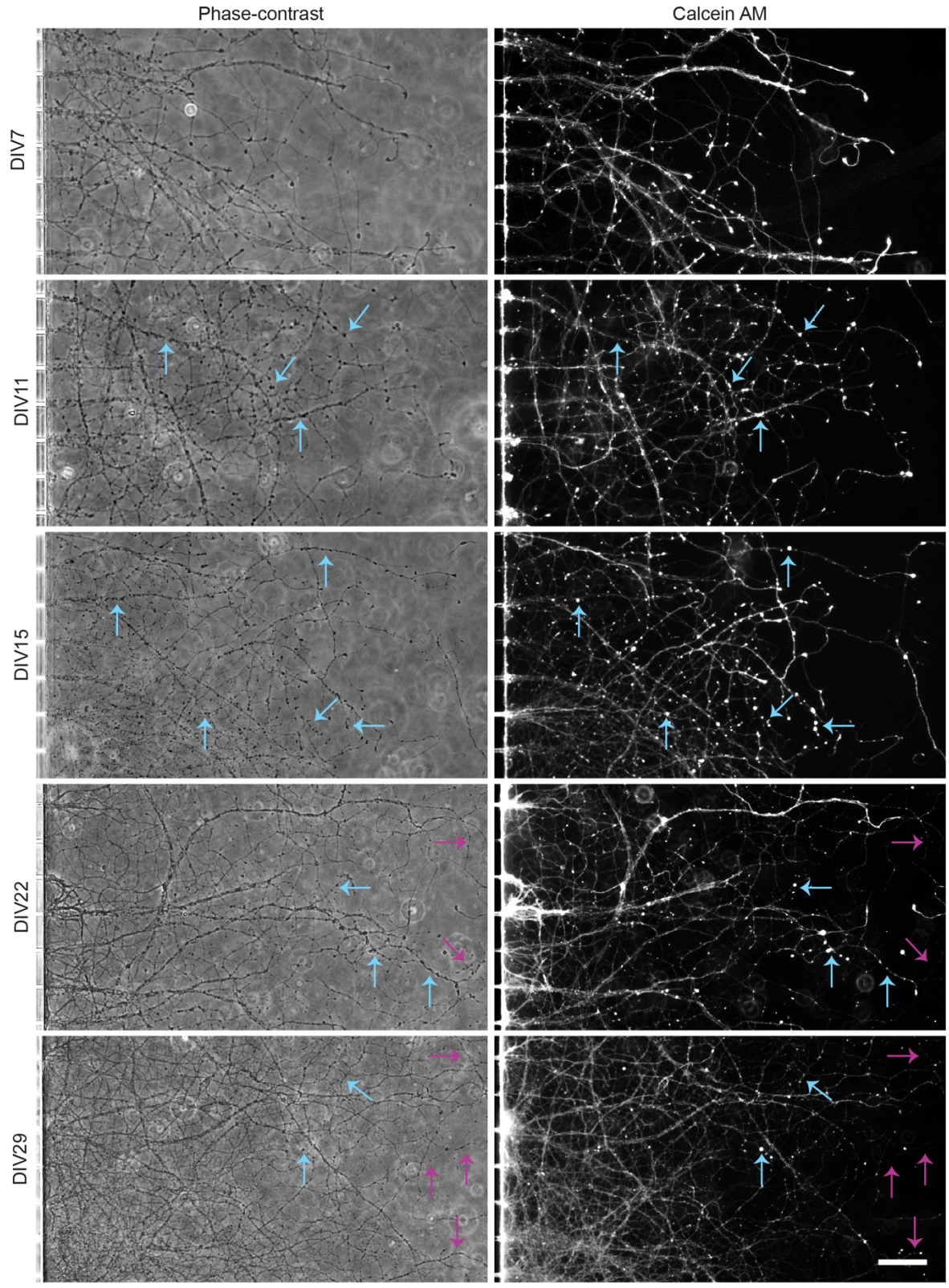

Fig. 18 Long-term cultivation of isolated axons.
Phase-contrast and calcein AM imaging of isolated axons confirmed that primary cortical neurons can be cultivated in the microfluidic devices until at least DIV 29. Axons showed axonal swellings (blue arrows) and fragments (purple arrows) starting from DIV 11, while axons did not reveal any aberrations at DIV 7. Scale bar = 100 µm.

3.1.2. Conventional image binarization approaches lead to information loss

To analyze the morphology of axons, we established a protocol based on the widely employed approach of image binarization[54,57]. All axons were binarized by the “find edges”-processing tool and the “Phansalkar” local auto-threshold (**Fig. 19a**). However, false positive signals such as microscopic artifacts were recognized by the “find edges”-processing tool. The specific ability of the local auto-threshold “Phansalkar” to recognize low-contrast structures led to the detection of many background signals.

Removing the background signals by excluding pixels of small size decreased the recognition of axons in both the 0 and 24 hours phase-contrast images (**Fig.19b**). Excluding particles of the size of 45 pixels removed not only all background signals but also some structures of the axons. Excluding particles of the size of 25 pixels recovered axonal structures at 0 and 24 hours but background signals emerged. Although the number of background signals was low, the axons lacked many structures. Excluding particles of the size of 15 pixels only partly segmented the axonal morphology. Furthermore, more background signals appeared.

Taken together, the image binarization approach failed to properly segment axons without the inclusion of background signals. However, excluding background signals resulted in axonal structures that appeared as non-connected particles. These structures may falsely be recognized as axonal fragments since the original 24 hours phase-contrast image did not contain any axonal fragments in the region of interest. Furthermore, image binarization does not allow to quantify axonal swellings.

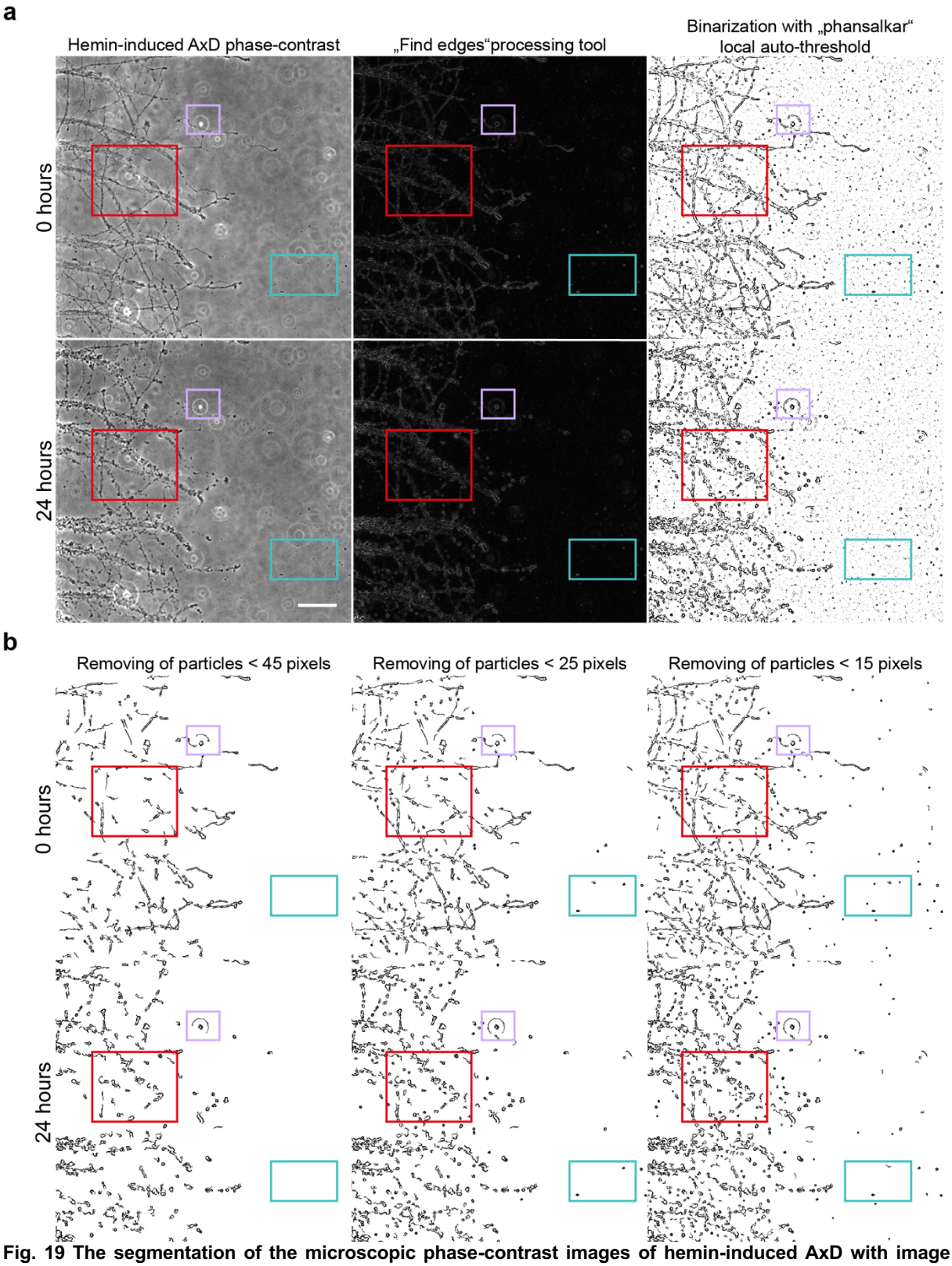

Fig. 19 The segmentation of the microscopic phase-contrast images of hemin-induced AxD with image binarization results in information loss.

a, Phase-contrast images of hemin-induced AxD at 0 and 24 hours processed with the “find edges”-processing tool of ImageJ and binarized with the “Phansalkar” local auto-threshold. While axonal structures (red box) were recognized in the binarized image, it also contained artifacts (purple box) and noise signals (cyan box). Scale bar = 100 µm. **b**, The noise (cyan box) of the binarized images (image size and dimensions are not changed) was removed by particle size selection leading to information loss (red box). Image processing did not exclude artifacts (purple box).

3.1.3. The EntireAxon CNN recognizes axons and the morphological hallmarks of AxD while bypassing the limitations of image binarization

We developed the EntireAxon CNN to overcome the limitations of the image binarization approach to properly segment axons. The EntireAxon CNN serves as a tool to extract information from microscopic images by objectively recognizing and classifying different structures. To this end, the EntireAxon CNN was trained with several images of healthy and degenerating axons that contained the morphological hallmarks of AxD.

We assessed the performance of the EntireAxon CNN by comparing its segmentation output on an unknown dataset versus a labeled ground truth (human evaluator 1) (**Table 10**). The class 'background' was recognized better (mean F1 score 0.995) than the classes 'axon' (0.780), 'axonal swelling' (0.567), and 'axonal fragment' (0.301). The lower ability of the EntireAxon CNN to recognize axonal swellings and fragments was likely based on the imbalance of the class distribution on the images (i.e., 96.42 % 'background', 2.77 % 'axon', 0.58 % 'axonal swelling', and 0.23 % 'axonal fragment' pixels in the training dataset).

Table 10 The validation of the EntireAxon CNN

Class	Precision	Recall	Mean F1-score
Background	0.993	0.996	0.995
Axon	0.789	0.774	0.780
Axonal swelling	0.609	0.534	0.567
Axonal fragment	0.805	0.196	0.301

We then compared the performance of the EntireAxon CNN to human evaluators. To this end, two additional evaluators (human evaluator 2 and 3) labeled the validation dataset (**Table 11**). The EntireAxon CNN accurately classified axons and axonal swellings more often (axon: mean F1 score 0.780, axonal swelling: 0.567) than human evaluator 2 (axon: 0.654, axonal swelling: 0.485) and human evaluator 3 (axon: 0.704, axonal swelling: 0.489). However, the EntireAxon CNN recognized axonal fragments better (0.301) than human evaluator 3 (0.221), but not better than human evaluator 2 (0.548).

Table 11 Mean F1 scores of the EntireAxon CNN compared to human evaluators on the validation dataset

	Mean F1-score			
Class	**Background**	**Axon**	**Axonal swelling**	**Axonal fragment**
EntireAxon CNN	0.995	0.780	0.567	0.301
Human evaluator 2	0.991	0.654	0.485	0.548
Human evaluator 3	0.993	0.704	0.489	0.221

As human evaluator 1 not only labeled the ground truth for the validation dataset but also for the training dataset, it was not surprising that the EntireAxon CNN performed better than the other evaluators because it learned the segmentation from that evaluator. To measure the generalizability of the EntireAxon CNN, we created consensus labels (merging of the individual labeled masks) among two human evaluators and compared the EntireAxon CNN to the remaining human evaluator. While there was a high degree of agreement between the human evaluators on 'background', 'axon', and 'axonal swelling', 'axonal fragments' represented the most challenging class to label (**Fig. 20**).

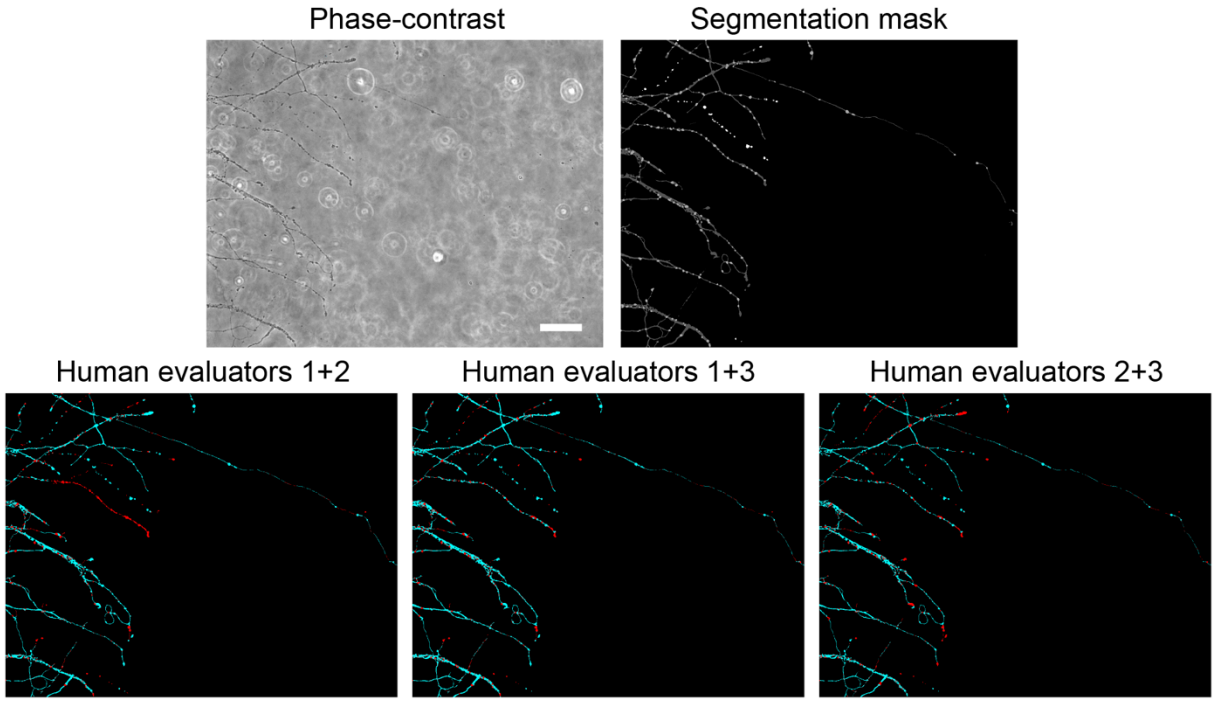

Fig. 20 The EntireAxon CNN segmentation and consensus labeling by human evaluators.
Phase-contrast image of the validation dataset and the resulting segmentation mask by the EntireAxon CNN. The consensus labeling masks of two human evaluators showed labeling agreement (cyan) or disagreement (red) between the two evaluators. Scale bar = 100 µm.

Regardless of the consensus, the EntireAxon CNN exceeded human abilities to recognize all classes demonstrating higher mean F1 scores (**Table 12**). The EntireAxon CNN and the human evaluators performed equally well in recognizing

'background' (EntireAxon CNN: 0.998, human evaluator 3: 0.998, human evaluator 2: 0.996 and human evaluator 1: 0.996). Based on the consensus labels of the human evaluators 1 and 2, the EntireAxon CNN outperformed human evaluator 3 in all classes (axon: 0.847 vs. 0.808, axonal swelling: 0.667 vs. 0.647, axonal fragment: 0.400 vs. 0.376). This was also the case when the EntireAxon CNN was compared to human evaluator 2 on the consensus labels of the human evaluators 1 and 3 (axon: 0.870 vs. 0.759, axonal fragment: 0.647 vs. 0.564), except for the class 'axonal swelling' (EntireAxon CNN: 0.710, human evaluator 2: 0.716). The EntireAxon CNN also exceeded human evaluator 1 on the consensus labels of the human evaluators 2 and 3 (axon: 0.781 vs. 0.747, axonal swelling: 0.607 vs. 0.592, axonal fragment: 0.590 vs. 0.421).

Table 12 Mean F1 scores of the EntireAxon CNN and the human evaluator in the consensus labeling.

		Mean F1-score			
Consensus	**Class**	**Background**	**Axon**	**Axonal swelling**	**Axonal fragment**
Evaluators 1 and 2	EntireAxon CNN	0.998	0.847	0.667	0.400
	Evaluator 3	0.998	0.808	0.647	0.376
Evaluators 1 and 3	EntireAxon CNN	0.998	0.870	0.710	0.674
	Evaluator 2	0.996	0.759	0.716	0.564
Evaluators 2 and 3	EntireAxon CNN	0.998	0.781	0.607	0.590
	Evaluator 1	0.996	0.747	0.592	0.421

The EntireAxon recognized axonal structures in phase-contrast images more accurately compared to the binarization approach conducted with ImageJ. (**Fig. 21**). The EntireAxon CNN fully segmented the axons without interruptions and properly recognized axonal swellings. While artifacts were recognized in the images that were binarized with ImageJ, these structures were not recognized by the EntireAxon CNN. A comparison with the original image revealed that the noise in the image binarization was falsely recognized as fragments. These structures were not recognized by the EntireAxon CNN. Taken together, the EntireAxon CNN is a reliable tool to recognize axons and the morphological hallmarks of AxD. It also allows the automatic analysis of the images after successful training.

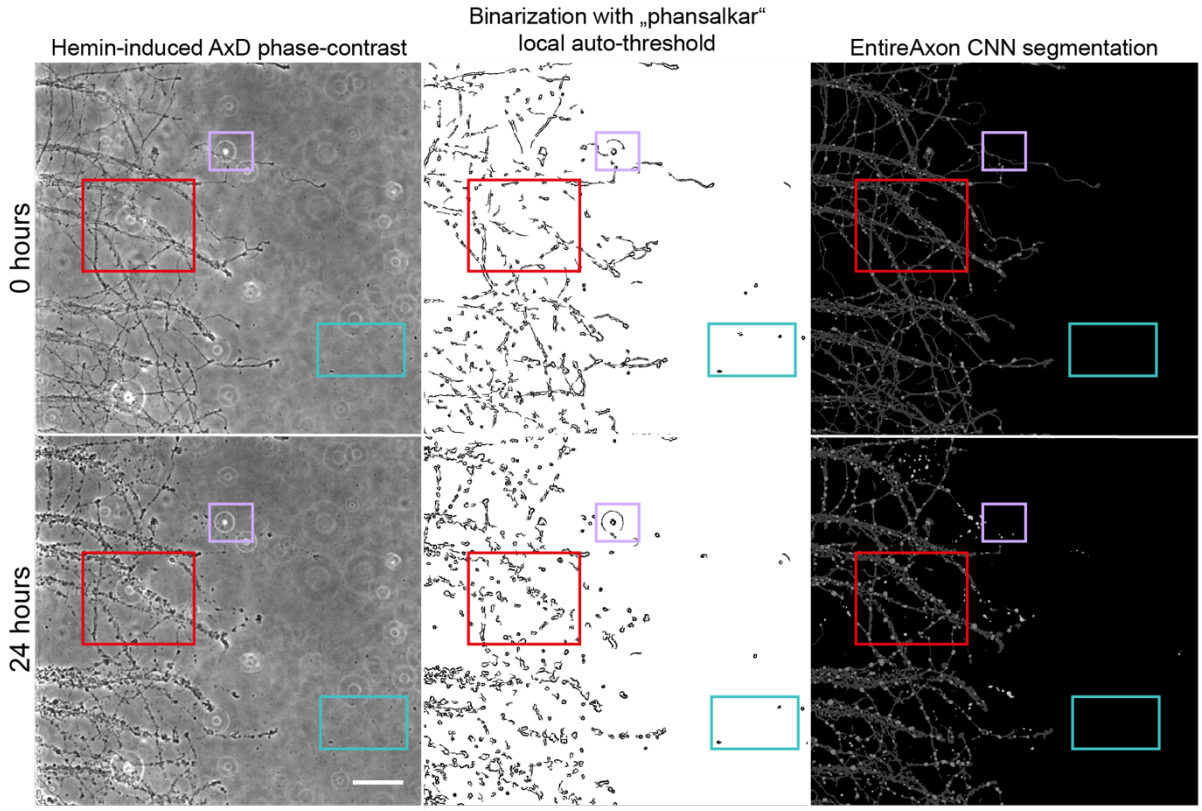

Fig. 21 The EntireAxon CNN output includes fully segmented axons but not microscopic artifacts in contrast to the binarization of phase-contrast images.
Upon image binarization, microscopic artifacts (purple boxes) and noise (cyan boxes) were recognized as false positive signals, while axons and axonal swellings (red boxes) were not fully recognized. The EntireAxon CNN did not consider microscopic artifacts (purple boxes) or noise (cyan boxes) and was able to fully segment axons (red boxes), axonal swellings (red boxes), and axonal fragments (purple box at 24 hours). Scale bar = 100 µm.

3.2. The morphological characterization of AxD

3.2.1. The progression of hemin-induced AxD

Using time-lapse microscopy, we recorded axons for 24 hours upon treatment with the hemolysis product hemin, as an *in vitro* model of intracerebral hemorrhage[79]. In contrast to vehicle-treated axons (0 µM), hemin-treated axons underwent morphological changes at different concentrations resulting in AxD (**Fig. 22** and **Videos 1-4** in[109]).

Axons that were not exposed to hemin (0 µM) grew continuously over 24 hours, not showing any retraction or compromisation. Axons treated with hemin did not grow continuously and degenerated. While axonal swellings emerged after 4-12 hours of hemin treatment (8-12 hours for 50 and 100 µM; 4-8 hours for 200 µM), individual axons disintegrated into axonal fragments between 8-20 hours after hemin treatment (20-24 hours for 50; 16-20 hours for 100 µM; 8-12 hours for 200 µM). In summary, visual inspection of the morphological hallmarks of AxD suggested that hemin-treated axons degenerated in a concentration-dependent manner.

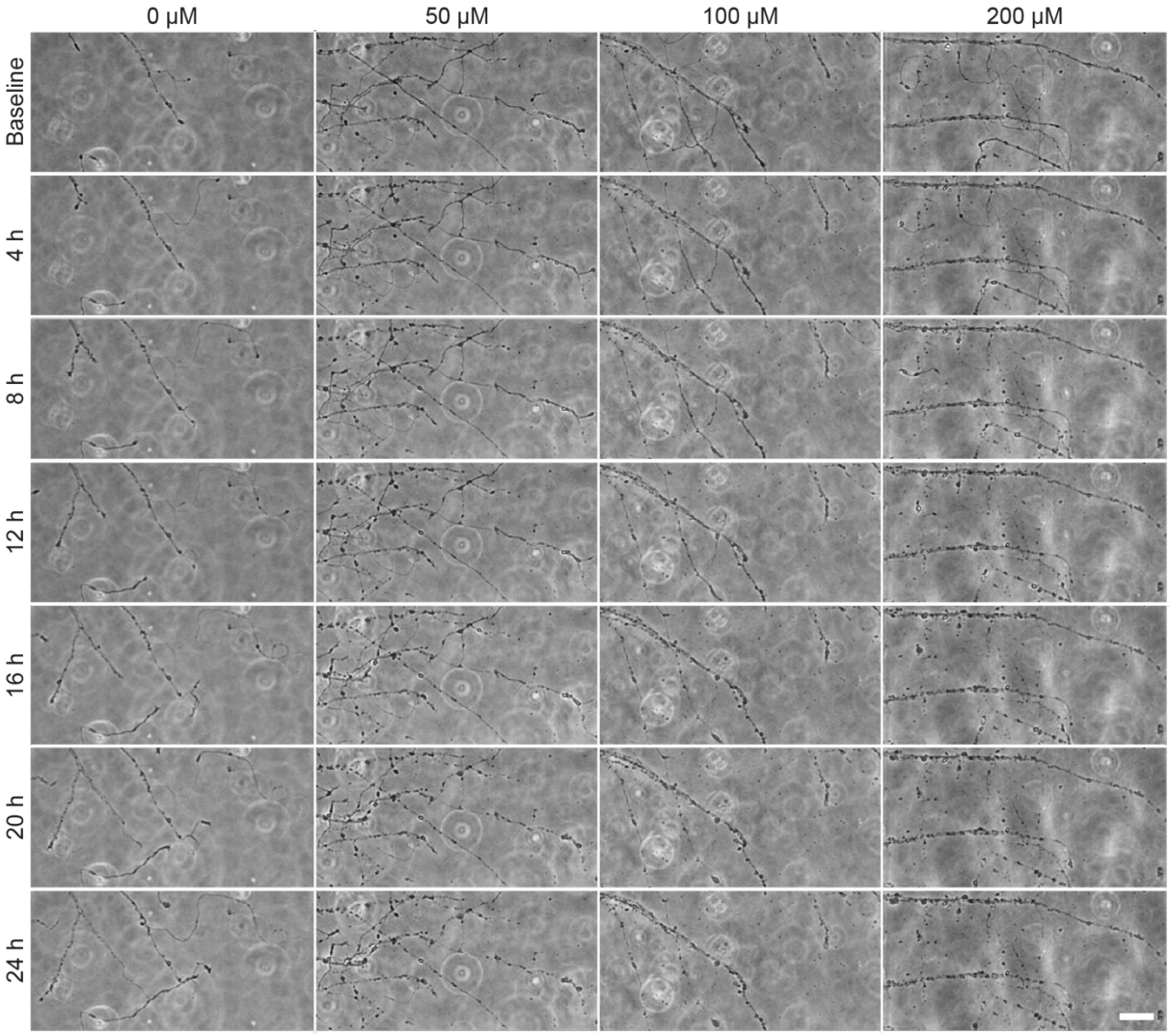

Fig. 22 The time-lapse recordings of degenerating axons upon hemin treatment.
Vehicle-treated (0 µM) axons grew over 24 hours, while hemin-treated (50, 100, and 200 µM) axons degenerated. Scale bar = 50 µm.

We used the EntireAxon CNN to determine the progression of AxD over 24 hours in time-lapse recordings of hemin-treated axons. According to area under the curve (AUC) analyses (**Fig. 23**), all three concentrations of hemin reduced the axon area (50 µM vs. 0 µM: $P = 0.026$; 100 µM vs. 0 µM: $P = 0.018$, 200 µM vs. 0 µM: $P < 0.001$), and elevated the axonal swelling area (50 µM vs. 0 µM: $P = 0.012$, 100 µM vs. 0 µM: $P = 0.005$, 200 µM vs. 0 µM: $P = 0.016$). Only 100 and 200 µM of hemin led to an increase of the axonal fragment area (vs. 0 µM: $P = 0.004$).

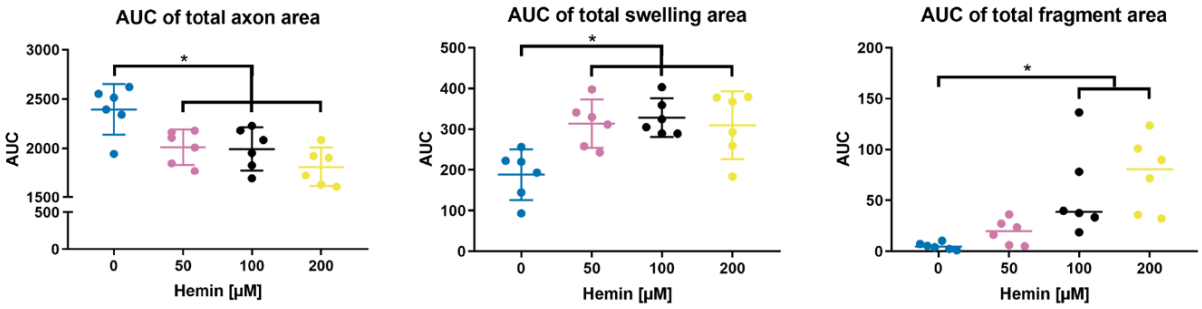

Fig. 23 The AUC analyses of axon, axonal swelling, and axonal fragment area in hemin-induced AxD. AxD was induced by hemin and recorded over 24 hours. The AUC of the total axon area decreased in hemin-treated axons, whereas axonal swelling and axonal fragment area increased. *N* = 6 biological replicates. Means ± 95% CI are shown for axon and axonal swelling area, medians are given for fragment area. * *P* < 0.05 vs. 0 µM for axon and swelling area, * *P* < 0.0167 for axonal fragment area (Bonferroni correction for nonparametric data). Please see Table S1 in the appendix for statistical details.

Time-course analyses revealed a concentration- and time-dependent degeneration of axons upon hemin exposure (**Fig. 24**). Specifically, hemin-induced AxD induced a reduction of the axon area starting at 15 hours for 50 µM (*P* = 0.018), at 14 hours for 100 µM (*P* = 0.040) and at 11.5 hours for 200 µM (*P* = 0.020). The axonal fragment area started to increase at 9 hours at 200 µM (*P* = 0.037) and at 17 hours for 100 µM hemin (*P* = 0.044). Interestingly, the axonal swelling area started to elevate several hours before the effects of the reduced axon area due to axonal fragments were detected, namely at 6 hours for 200 µM (*P* = 0.010) and 100 µM (*P* = 0.019), and at 8 hours for 50 µM hemin (*P* = 0.030).

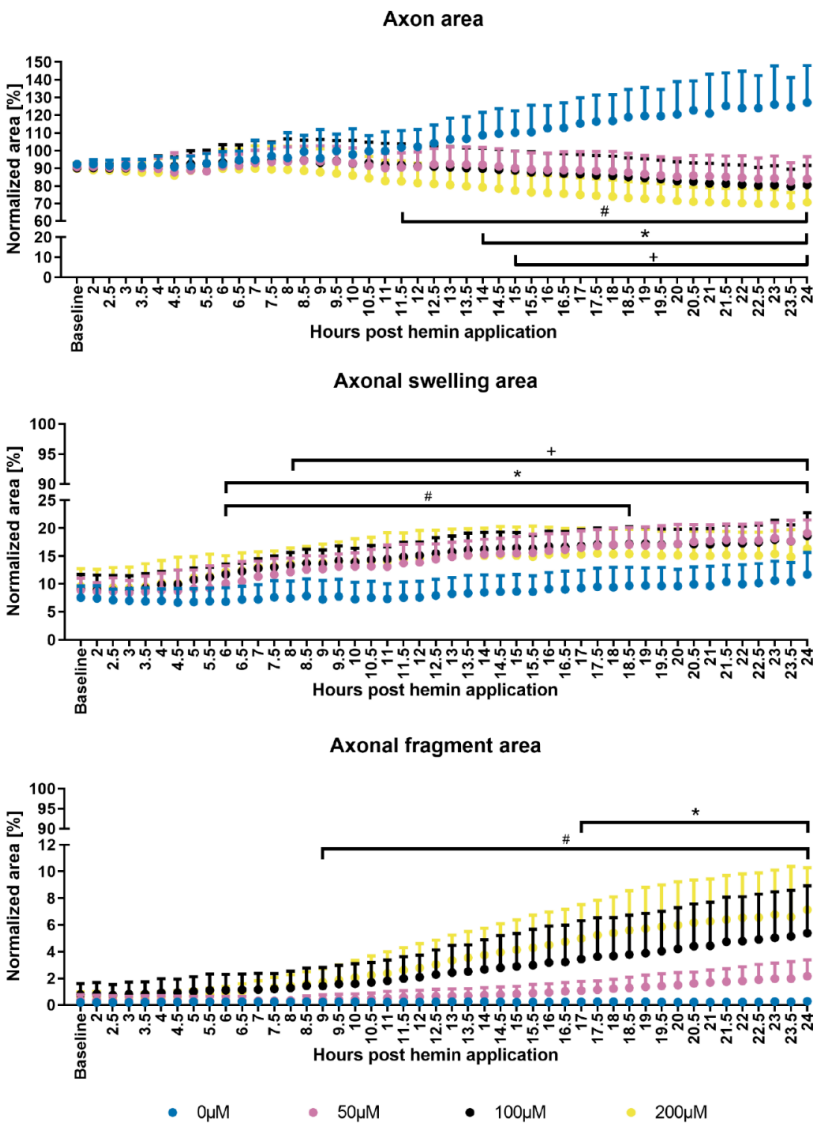

Fig. 24 The progression of hemin-induced AxD.
AxD was induced by hemin and recorded over 24 hours leading to a concentration-dependent decrease in axon area, while axonal swelling and axonal fragment area increased. Values were normalized to baseline. $N = 6$ biological replicates, means ± 95% CI are shown.
+, *, # $P < 0.05$; + for 50 µM vs. 0 µM, * for 100 µM vs. 0 µM, # for 200 µM vs. 0 µM. Please see Table S2 in the appendix for statistical details.

Further fluorescent live cell staining with calcein AM confirmed the time course analysis as it showed the initiation of AxD between 16 and 20 hours for 50 µM hemin, between 12 and 16 hours for 100 µM hemin, and between 4 and 12 hours for 200 µM hemin (**Fig. 25**). The initiation of AxD was characterized by a punctate axonal staining with calcein AM. In the following hours, axons were stained less consistently for each hemin concentration representing AxD. Taken together, the morphological analysis of AxD with the EntireAxon CNN revealed a concentration- and time-dependent progression of hemin-induced AxD.

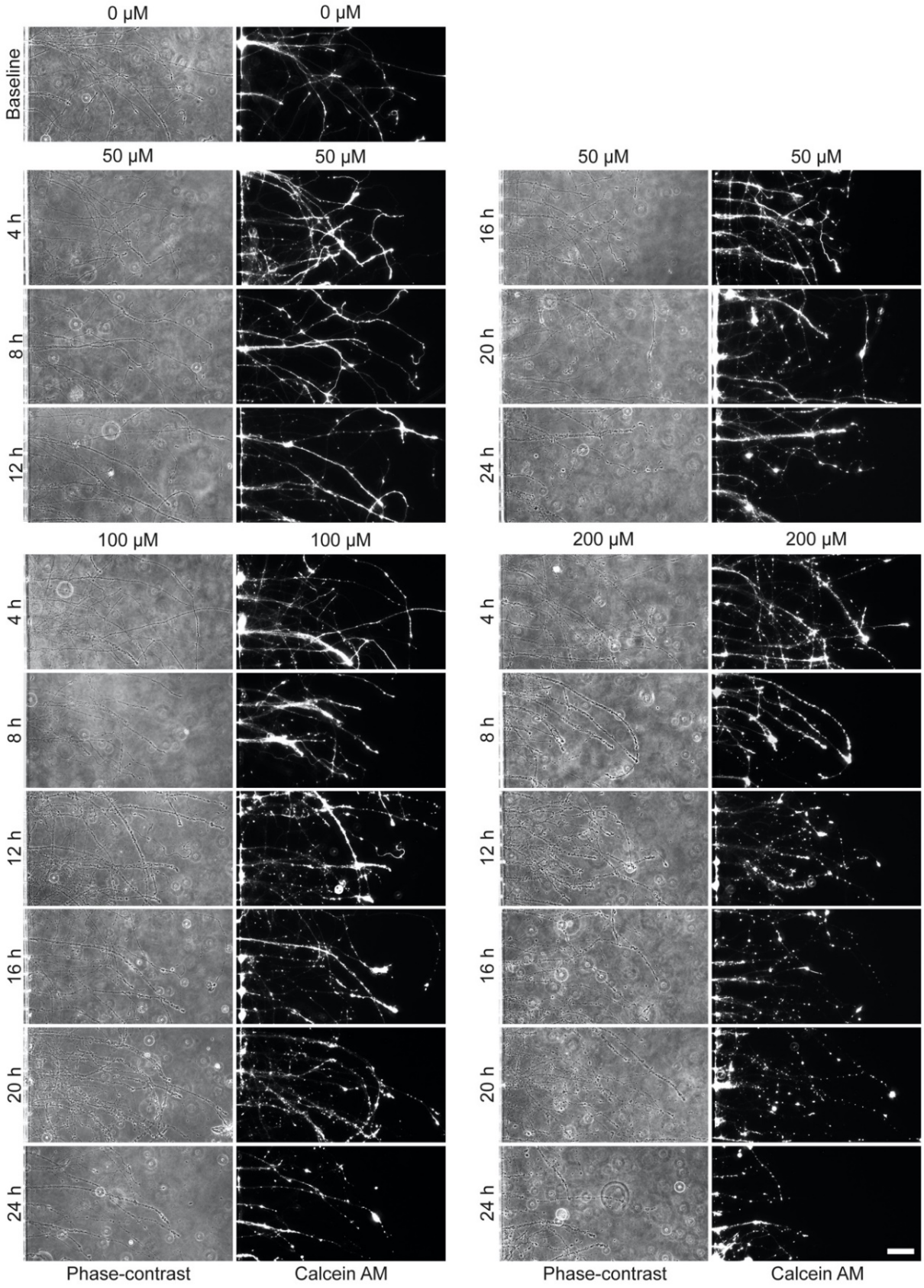

Fig. 25 AxD time course by calcein AM staining.
Calcein AM staining of axons appeared more punctate over time confirming the starting time point (after 16 hours for 50 µM, after 12 hours for 100 µM and after 4 hours for 200 µM hemin) and ending time points (following 4 hours for all concentrations) of hemin-induced AxD via fluorescence microscopy. *N* = 3 biological replicates. Scale bar = 50 µm.

3.2.2. Morphological heterogeneity of AxD

3.2.2.1. The EntireAxon RNN recognizes four morphological patterns of AxD

The visual inspection of the time-lapse data revealed that axons degenerate according to four morphological patterns that can occur in the same axons over time (**Fig. 26** and **Videos 5-8** in[109]). We therefore classified the following four morphological patterns of AxD based on the time-lapse recordings:

1) Granular degeneration: AxD resulting in granular separated fragments.
2) Retraction degeneration: AxD in which the distal part of the axon retracts ultimately resulting in granular degeneration.
3) Swelling degeneration: AxD with the enlargement of axonal swellings and subsequent granular degeneration.
4) Transport degeneration: AxD in which axonal swellings of constant size, which do not enlarge, are transported along the axon resulting in granular degeneration.

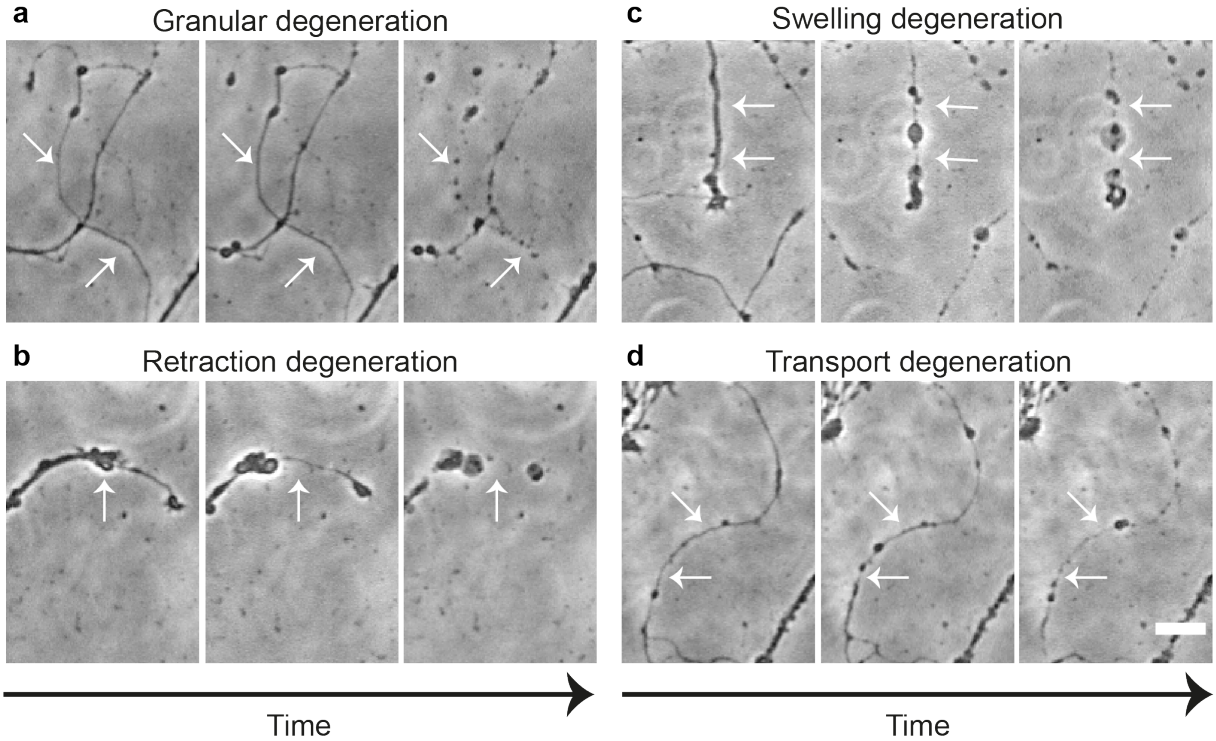

Fig. 26 Axons undergo the four morphological patterns of AxD.
Examples of the four morphological patterns of AxD in microscopic phase-contrast recordings. White arrows indicate the location of degeneration in each pattern: granular (**a**), retraction (**b**), swelling (**c**), and transport (**d**) degeneration. Scale bar = 20 µm.

We created a training dataset that contained examples of the four different morphological patterns of AxD in the 24-hour segmentation recordings and trained the EntireAxon RNN to identify changes in class segregation over time (**Fig. 27**).

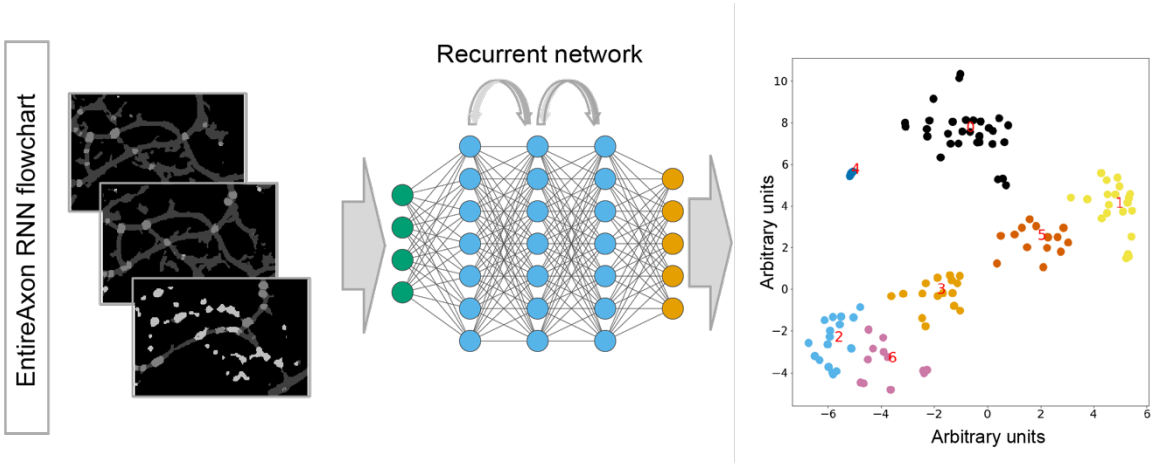

Fig. 27 Cluster generation for the training of the EntireAxon RNN.
The workflow of the EntireAxon RNN included training with the segmentation masks and cluster generation to determine the morphological patterns of AxD (cluster 0-6).

For each time point, the EntireAxon RNN computed the probability of a change in class for each pixel of an image relative to the previous time point. As each class can change to any of the three remaining classes or remain the same over time (4 possible changes per class), 16 different class pairs can emerge. The EntireAxon RNN determined seven clusters (cluster 0-6) that were characterized by an idiosyncratic segmentation pattern over 24 hours (**Fig. 28**). All clusters showed a decrease in the class ‘axon’ and an increase in the class ‘background’. The decline of the class ‘axon’ and rise of the class ‘background’ differed in the extent and temporal progression among the clusters. Simultaneously, the classes ‘axonal swelling’ and/or ‘axonal fragment’ changed in some clusters.

In cluster 0, there was a steep early decrease in the class ‘axon’, which then continued more linearly. There was also a later rise in the class ‘axonal fragment’. In contrast to cluster 0, cluster 1 showed no increase in the class ‘axonal fragment’ and a linear decrease in the class ‘axon’ from the start. In cluster 2, there was a strong increase in the class ‘axonal swelling’. Cluster 3 demonstrated an early and lasting high level of the class ‘axonal swelling’ with a later increase in the class ’axonal fragment’. Cluster 4 showed a rapid decrease in the class ‘axon’ concomitant with an increase in the classes ‘background’ and ‘axonal swelling’. Cluster 5 was similar to cluster 1, but with an early drop in the class ‘axon’. Cluster 6 showed an increase in the class ‘axonal swelling’ similar to but to a greater extent than cluster 2.

Fig. 28 Class changes over time in segmentation inform cluster analysis of the four morphological patterns of AxD via the EntireAxon RNN.
The EntireAxon RNN related each time point to the previous time point to characterize each cluster (0-6) by an distinct segmentation pattern that was based on the probability of a pixel-wise change in class of an image over 24 hours resulting in 16 possible class pairs. Image courtesy: Philipp Grüning.

The EntireAxon RNN categorized each cluster to one of the four morphological patterns (**Fig. 29**): i) Granular degeneration was defined by clusters that describe the degeneration of axons into axonal fragments, i.e., clusters 0, 1, 3, and 5; ii) Retraction degeneration only included the clusters 1 and 5, indicating the retraction of the axon followed by its fragmentation; iii) Swelling degeneration was characterized by the three clusters that included the class ‘axonal swelling, i.e., clusters 2, 3, and 6, as well as cluster 5 showing the exchange of the class ‘axon’ for ‘background’; iv) Transport degeneration was the only pattern that relied on cluster 4 and was also characterized

partly on clusters 0, 1, 2, and 6. Although some clusters overlapped in some morphological patterns, the unique combination of the different clusters allowed to clearly distinguish all four morphological patterns.

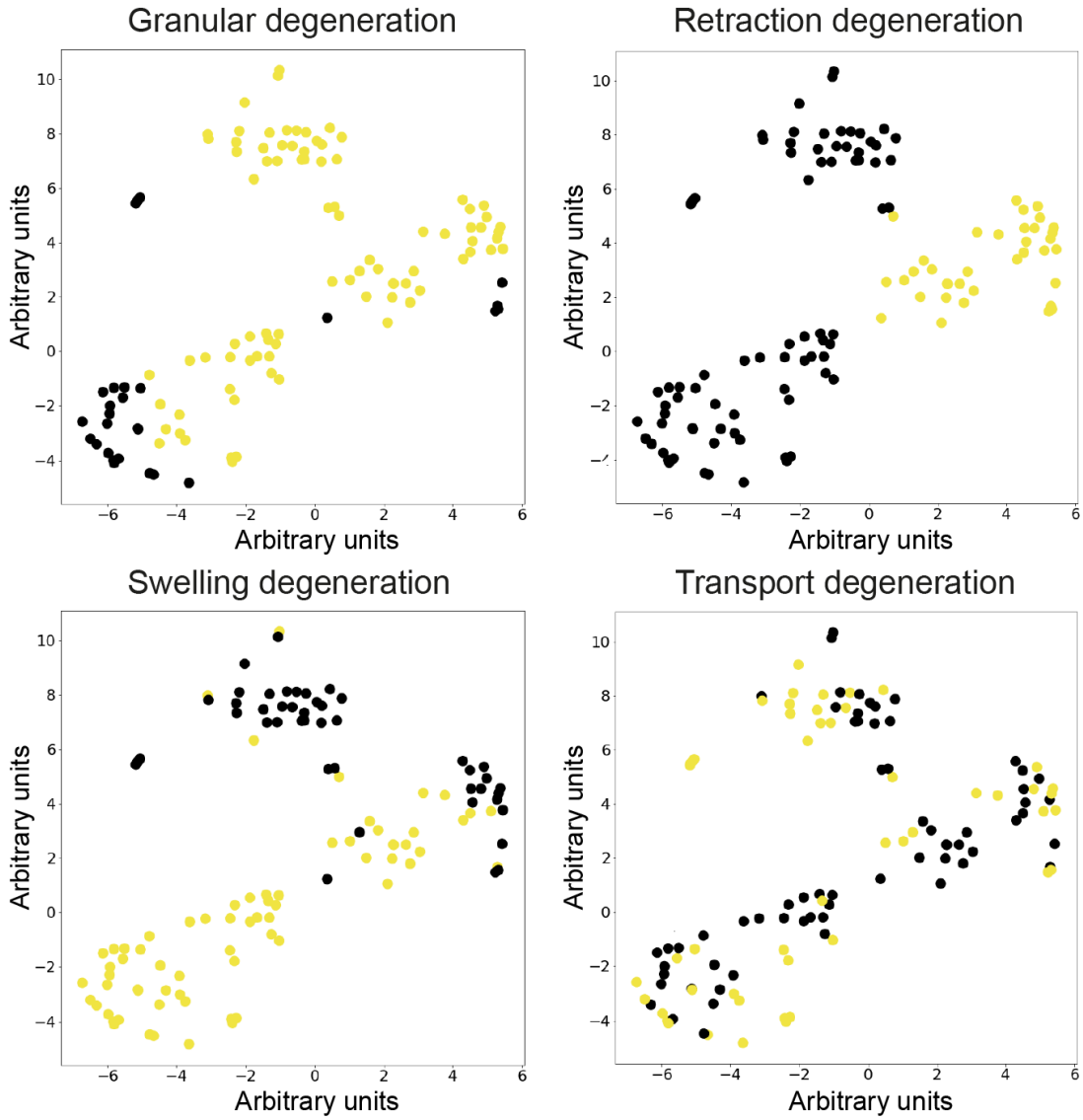

Fig. 29 The EntireAxon RNN recognizes all four morphological patterns of AxD.
Each morphological pattern of AxD was classified according to included (yellow) or excluded (black) images. Image courtesy: Philipp Grüning.

A 10-fold cross-validation was performed to validate the EntireAxon RNN and confirmed the ability of the EntireAxon RNN to distinguish between the four morphological patterns of AxD (**Table 13**). The EntireAxon RNN recognized the morphological pattern ‘granular degeneration’ better (mean F1 score 0.868) than the morphological patterns ‘swelling degeneration’ (0.681), ‘transport degeneration’ (0.575), and ‘retraction degeneration’ (0.456).

Table 13 The performance of the EntireAxon RNN to distinguish the four morphological patterns of AxD assessed by ten-fold cross-validation.

AxD patterns	Precision	Recall	Mean F1-score
Granular degeneration	0.796	0.953	0.868
Retraction degeneration	0.419	0.500	0.456
Swelling degeneration	0.681	0.681	0.681
Transport degeneration	0.442	0.824	0.575

3.2.2.2. The concentration-dependent occurrence of the morphological patterns of AxD upon hemin exposure

We then applied the EntireAxon RNN to quantify the occurrence of the four morphological patterns of AxD in axons exposed to the different concentrations of hemin (0, 50, 100, and 200 µM; **Fig. 30**). Axons exposed to hemin underwent granular, retraction, swelling, and transport degeneration concomitantly as these patterns emerged either close to each other or at the same locations (**Fig. 30a**). All morphological patterns eventually resulted in granular and separated fragments. Thus, the detection of granular degeneration overlapped with all other patterns. However, retraction, swelling, and transport degeneration only partly overlapped, suggesting that an axon does not strictly disintegrate according to one specific pattern only.

We therefore examined the extent of the area of the degenerated axons that was affected by a respective morphological pattern. Granular, retraction, and swelling degeneration covered larger parts of the axon than transport degeneration (**Fig. 30b**). The areas of granular ($P < 0.001$), swelling ($P < 0.001$) and transport degeneration ($P = 0.025$) correlated positively with increasing hemin concentrations. Retraction degeneration did not increase upon hemin exposure ($P = 0.800$). Linear regression analyses revealed that the slopes of granular and swelling degeneration were significantly steeper than the slope of transport degeneration (granular vs. transport degeneration: $P = 0.005$; swelling vs. transport degeneration: $P = 0.007$; **Table 14**). Furthermore, the slope of swelling degeneration was steeper than the slope of retraction degeneration (swelling vs. retraction degeneration: $P = 0.008$). The steepness of the slopes between granular and swelling degeneration ($P = 0.655$) and retraction and transport degeneration ($P = 0.528$) were not significantly different. Collectively, our data suggest a morphological heterogeneity through which axons disintegrate in hemin-induced AxD.

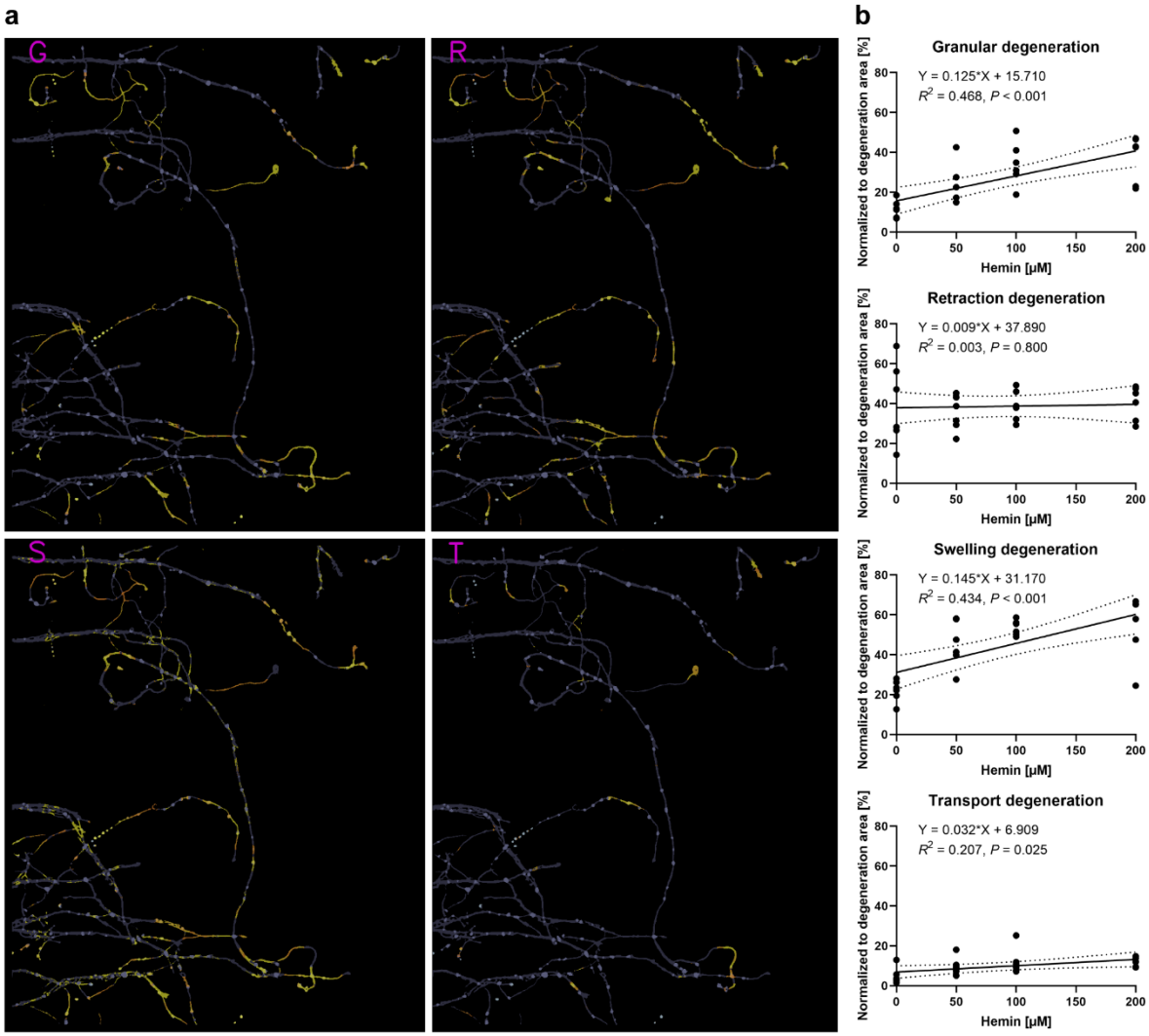

Fig. 30 The occurrence of the morphological patterns of AxD depends on the hemin concentration.
a, The occurrence of the four morphological patterns of AxD (granular = G, retraction = R, swelling = S, and transport = T degeneration) in hemin-treated axons (200 µM). **b**, Linear regressions of the four patterns of AxD in hemin-induced AxD. The area classified for each pattern was normalized to the total degeneration area. Dotted lines represent 95 % confidence bands. *N* = 6 biological replicates. Please see Table S3 in the appendix for statistical details.

3.3. The systematic characterization of the molecular mechanisms underlying hemin-induced AxD

Axons exposed to hemin undergo morphological changes during which axonal swellings and axonal fragments emerge. However, the molecular mechanisms underlying hemin-induced AxD are unknown.

Treating axons with 100 µM hemin affected all three readouts (i.e., the axon, axonal swelling, and axonal fragment area) in contrast to 50 µM hemin, and did not induce AxD as fast as 200 µM hemin (axon area: 14 hours (100 µM) vs. 11.5 hours (200 µM), axonal fragments: 17 hours (100 µM) vs. 9 hours (200 µM). Thus, we decided to treat axons with 100 µM hemin to examine whether the axonal morphology can be rescued

by chemical inhibitors of several molecular mechanisms, including calpain/cathepsin activation, transcription and translation, necroptosis, autophagy, apoptosis and ferroptosis. Specifically, we exposed axons to hemin for 24 hours to induce AxD, and simultaneously treated somata and axons with different chemical inhibitors over 24 hours. The choice of the concentrations for each chemical inhibitor was based on their previous employment in protecting primary cortical neurons from hemin, or was derived from further studies[30,40,46,79,116–122].

3.3.1. AxD at 24 hours upon hemin exposure (positive control)

The axon area of vehicle-treated axons increased within 24 hours after treatment, while it decreased in hemin-treated axons ($P < 0.001$, **Fig. 31**). The axonal swelling area ($P = 0.003$) and the axonal fragment area ($P < 0.001$) were both higher in axons treated with hemin as compared to vehicle-treated axons. The values of hemin-treated axons served as a positive control and the results of the chemical inhibitors were compared to axons treated with hemin alone.

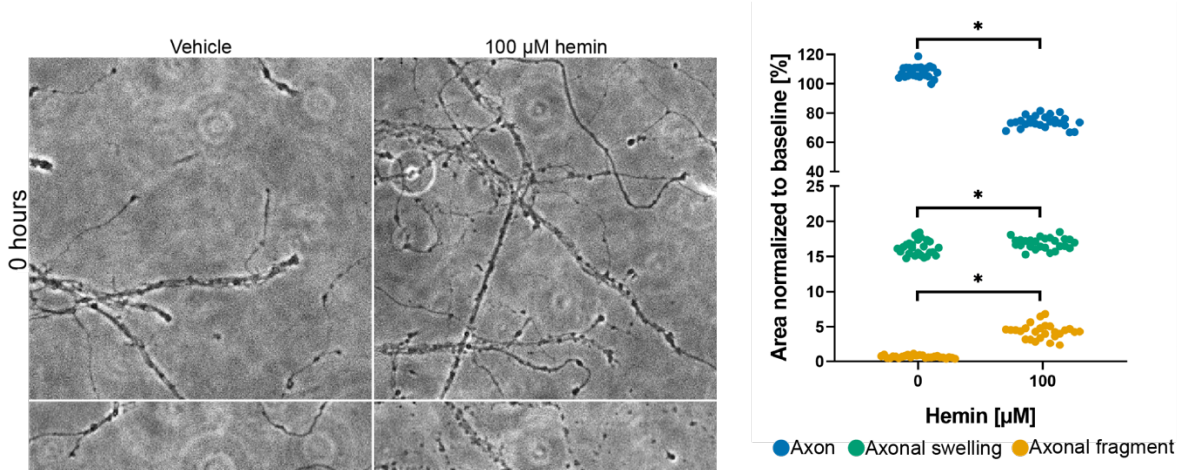

Fig. 31 The positive control of hemin-induced AxD.
Axons were treated with vehicle (0 µM hemin) or hemin (100 µM) and recorded at 0 and 24 hours after treatment. Images show phase-contrast recordings. Scale bar = 100 µm. The graph shows the quantification of axon, axonal swelling, and axonal fragment areas at 24 hours relative to 0 hours over all experimental days of the rescue experiments, $N = 26$ biological replicates. * $P < 0.05$ vs. 0 µM. Please see Table S4 in the appendix for statistical details.

3.3.2. The inhibition of calpains and cathepsins exacerbates hemin-induced AxD

Calpains has been demonstrated to be activated upon mechanical injury to axons and was associated with the formation of axonal swellings[10,123], while cathepsins has been linked to degradative lysosomes in axons undergoing local degradation[124]. Thus, we investigated whether hemin-induced AxD can be prevented by the calpain/cathepsin inhibitors ALLN, E64d, and MDL28170 (**Fig. 32**). The axonal morphology was still compromised after administration of each of the three inhibitors with all axons showing morphological AxD hallmarks, i.e., axonal swellings and fragments. While ALLN led to a decrease of the axon area (for 100 µM, P = 0.004) and axonal swelling area (for 100 µM, P = 0.01) and to an increase in axonal fragment area (for 10 µM, P = 0.01) after 24 hours treatment, 100 µM of MDL28170 only decreased the axon area (P = 0.004). E64d did not affect any class. These results suggest that the inhibition of calpains/cathepsins may exacerbate AxD rather than rescue axonal morphology.

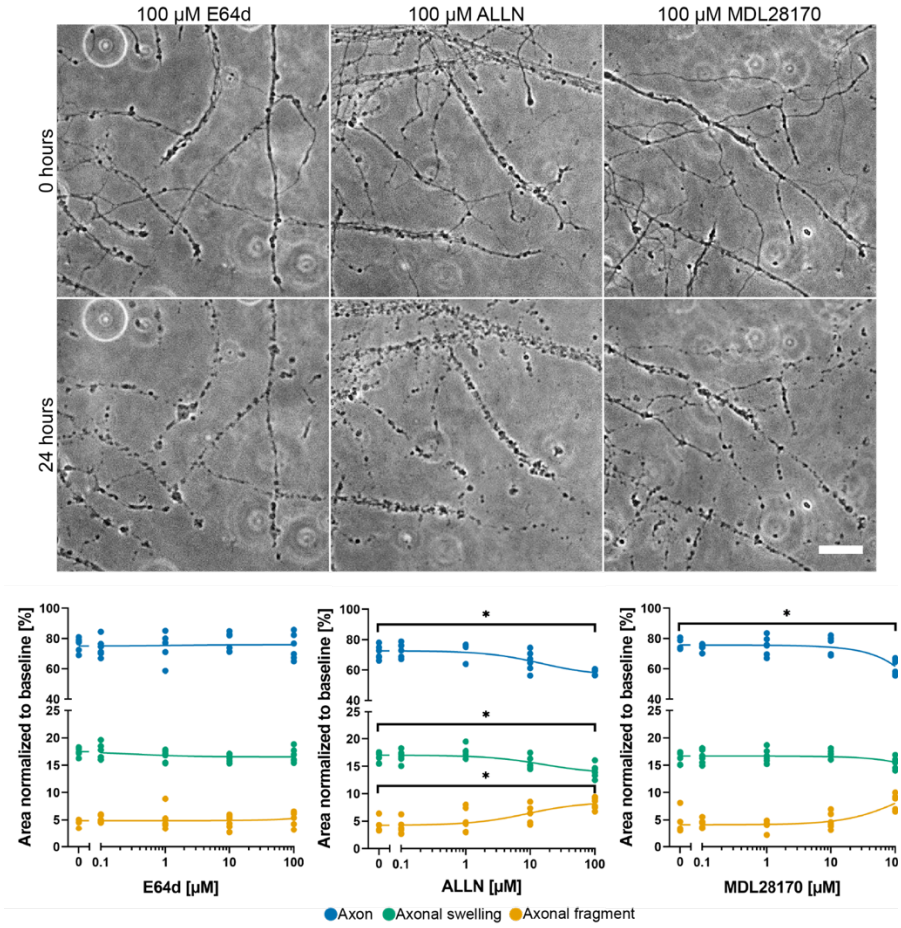

Fig 32 Inhibitors of calpain/cathepsin do not rescue axons in hemin-induced AxD. Phase-contrast microscopy images of axons treated with hemin (100 µM) and the three inhibitors ALLN, E64d, and MDL28170. Scale bar = 100 µm. Concentration-responses of the inhibitors in hemin-treated axons at 24 hours. N = 6 biological replicates. Each biological replicate is displayed around the regression of axon (blue), axonal swelling (green), and axonal fragment (yellow). * P < 0.05 vs. 0 µM. Please see Table S5 in the appendix for statistical details.

3.3.3. The inhibition of translation exacerbates axonal morphology in hemin-induced AxD

Nuclear transcription and local axonal protein synthesis represent underlying mechanisms of axonal response after injury[51]. As genetic deletion or silencing of RNA of pro-degenerative molecules has been demonstrated to rescue axonal morphology[27,30], we examined the effect of the transcription inhibitor Act-D and the translation inhibitor Chx in hemin-induced AxD (**Fig. 33**).

Axons were not significantly affected by Act-D compared to hemin treatment alone. Chx concentration-dependently decreased the axon area (for 1 µM, $P = 0.004$) and the axonal swelling area (for 10 µM, $P = 0.004$), while elevating the axonal fragment area (for 10 µM, $P = 0.006$). In summary, the inhibition of translation aggravated the axonal morphology.

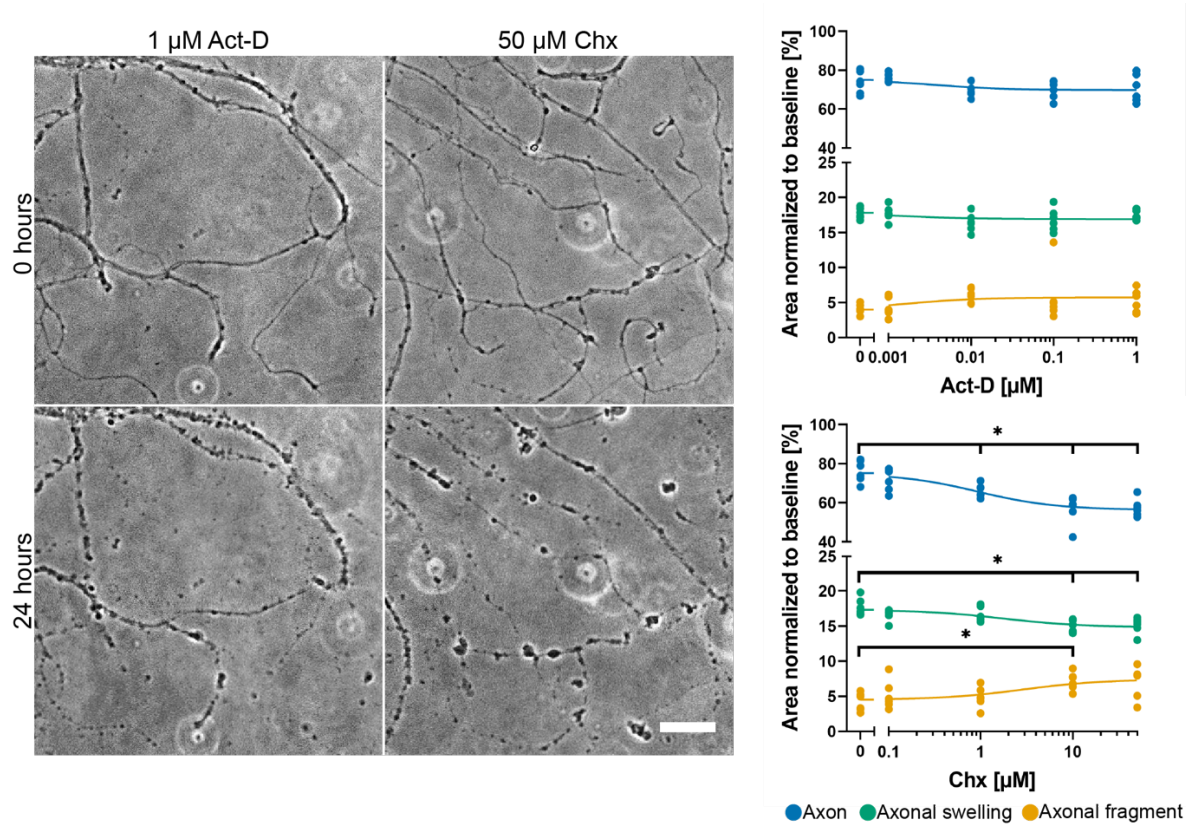

Fig. 33 Transcription and translation inhibition do not prevent hemin-induced AxD.
Phase-contrast microscopy images of degenerating axons treated with hemin (100 µM) and Act-D and Chx for 24 hours. Scale bar = 100 µm. Concentration-responses of Act-D and Chx in hemin-treated axons at 24 hours. $N = 6$ biological replicates. Each biological replicate is displayed around the regression of axon (blue), axonal swelling (green) and axonal fragment (yellow). * $P < 0.05$ vs. 0 µM. Please see Table S6 in the appendix for statistical details.

3.3.4. The inhibition of necroptosis did not rescue the axonal morphology in hemin-induced AxD

As the necroptotic pathway has been demonstrated to contribute to AxD[41,46], we assessed different necroptosis inhibitors, i.e., Nec-1 (compared with its inactive control Nec-1i; where possible, we used inactive controls of the chemical inhibitors to ensure target specificity) to target RIPK1, GSK872 for RIPK3, and NSA for MLKL. Co-treatment with these inhibitors did not prevent the disintegration of axons after 24 hours as they still displayed similar axonal swelling and axonal fragment areas (**Fig. 34**). Axons co-treated with 10 µM NSA even exhibited an elevated axonal fragment area (P = 0.010).

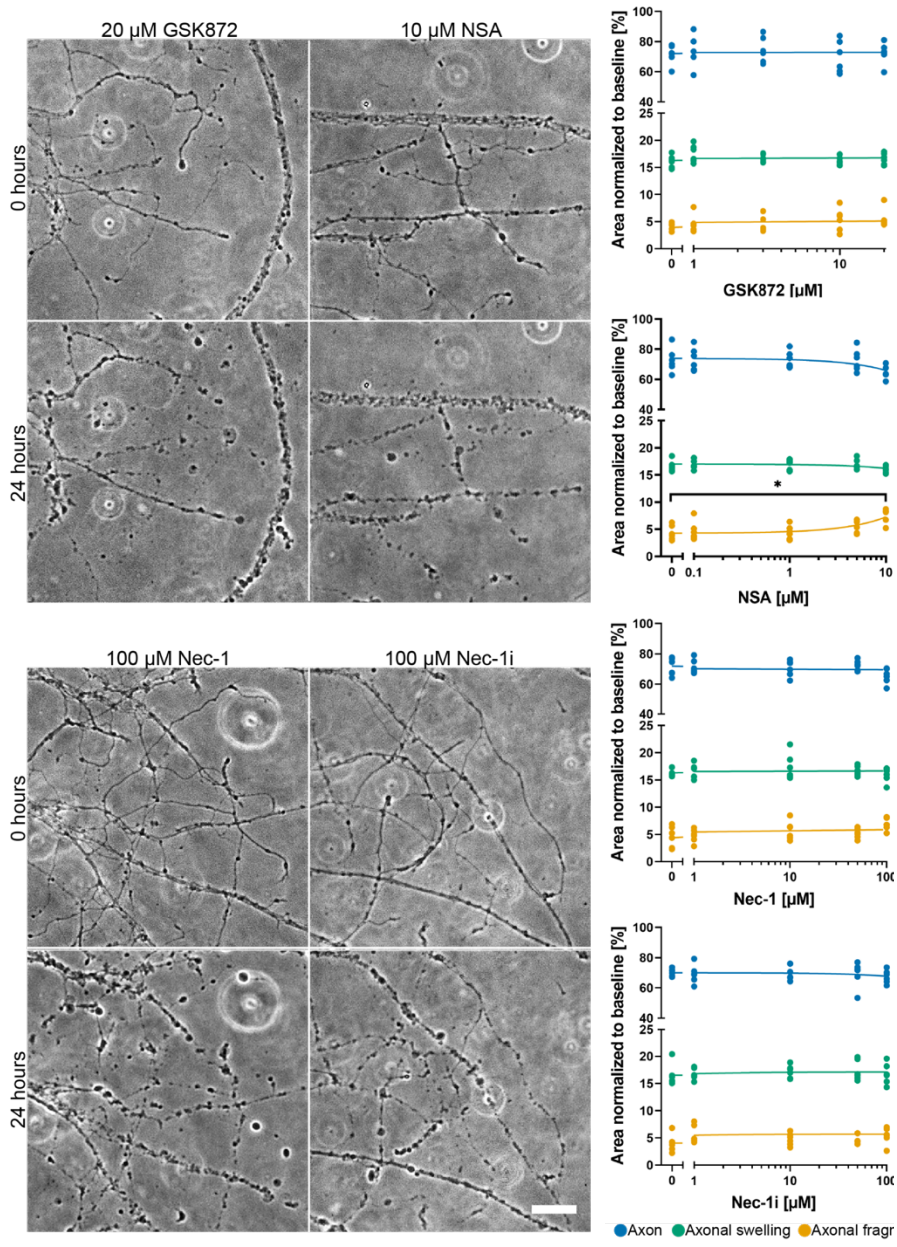

Fig. 34 Inhibitors of necroptosis do not rescue axons in hemin-induced AxD. Phase-contrast microscopy images of degenerating axons treated with hemin (100 µM) and necroptosis inhibitors and inactive controls (Nec-1i) at 24 hours. Scale bar = 100 µm. Concentration-responses of necroptosis inhibitors in hemin-treated axons for 24 hours. N = 6 biological replicates. Each biological replicate is displayed around the regression of axon (blue), axonal swelling (green) and axonal fragment (yellow). * P < 0.05 vs. 0 µM. Please see Table S7 in the appendix for statistical details.

3.3.5. The inhibition of autophagy and mitochondrial fission fail to rescue axons in hemin-induced AxD

Necroptosis inhibition during AxD has also been associated with mitochondrial fragmentation[41]. Furthermore, impaired axonal transport of degradative lysosomes leads to axonal autophagy and autophagosome accumulation in axons upon optic nerve crush injury[37,124]. We employed the lysosomal degradation inhibitor BafA1 and the mitochondrial fission inhibitor Mdivi-1 in an attempt to rescue the axonal morphology in hemin-induced AxD (**Fig. 35**).

Treating axons and their somata with Mdivi-1 and BafA1 did not rescue axons exposed to hemin. BafA1 even further decreased the axon area (for 0.01 µM, $P = 0.006$) as well as the axonal swelling area (for 0.1 µM, $P = 0.004$), while the axonal fragment area was not significantly increased. Taken together, hemin-induced AxD was not prevented by both inhibitors.

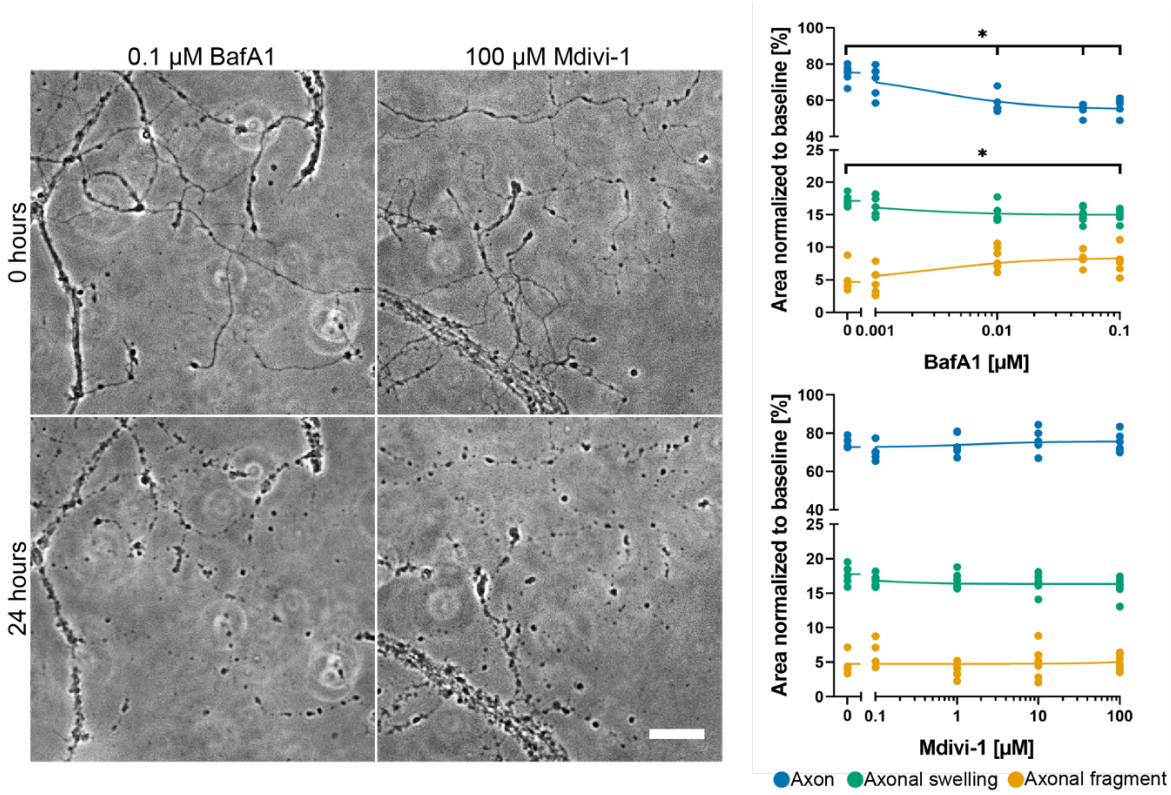

Fig. 35 Autophagy and mitochondrial fission inhibitors do not prevent hemin-induced AxD.
Phase-contrast microscopy images of degenerating axons treated with hemin (100 µM) and BafA1 and Mdivi-1 for 24 hours. Scale bar = 100 µm. Concentration-responses of BafA1 and Mdivi-1 in hemin-treated axons at 24 hours. $N = 6$ biological replicates. Each biological replicate is displayed around the regression of axon (blue), axonal swelling (green) and axonal fragment (yellow). * $P < 0.05$ vs. 0 µM. Please see Table S8 in the appendix for statistical details.

3.3.6. No association between hemin-induced AxD and apoptosis

Since caspases have been reported to play a pivotal role in chemo-induced AxD[58], we used the broad spectrum caspase inhibitor z-VAD-fmk[118] as a potential strategy

against hemin-induced AxD. The treatment with z-VAD-fmk did not protect axons from AxD (**Fig. 36**).

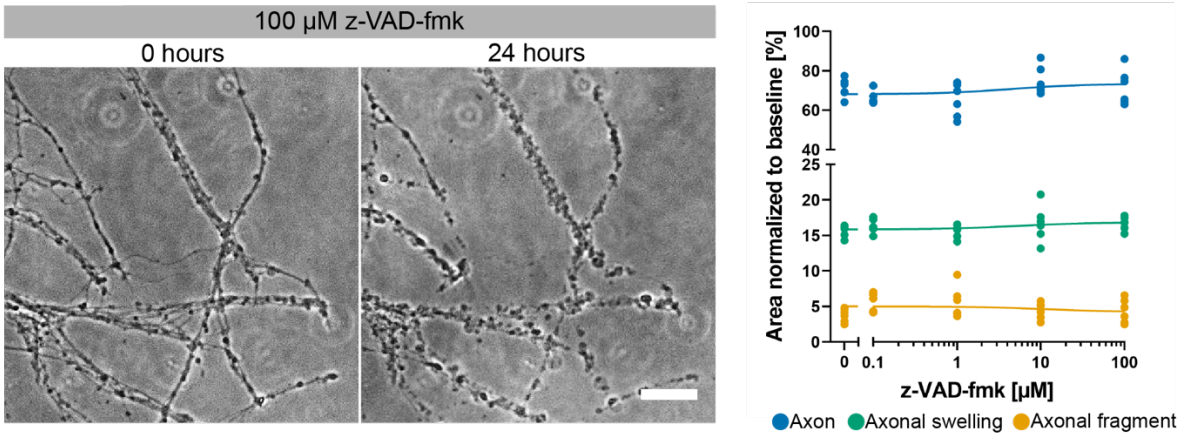

Fig. 36 The broad spectrum caspase inhibitor z-VAD-fmk does not prevent hemin-induced AxD.
Phase-contrast microscopy images of degenerating axons treated with hemin (100 µM) and z-VAD-fmk for 24 hours. Scale bar = 100 µm. Concentration-response of z-VAD-fmk in hemin-treated axons at 24 hours. *N* = 6 biological replicates. Each biological replicate is displayed around the regression of axon (blue), axonal swelling (green) and axonal fragment (yellow). * *P* < 0.05 vs. 0 µM. Please see Table S9 in the appendix for statistical details.

Next, we assessed the cleavage of caspase-3 as a marker for apoptosis. First, we confirmed the specificity of the cleaved caspase-3 antibody by treating the somata of primary cortical neurons with staurosporine that is known to induce caspase-dependent apoptosis[125]. As expected, treatment with 0.3 µM staurosporine for 9 hours led to an increased expression of cleaved caspase-3 in the axons (*P* = 0.014) (**Fig. 37**).

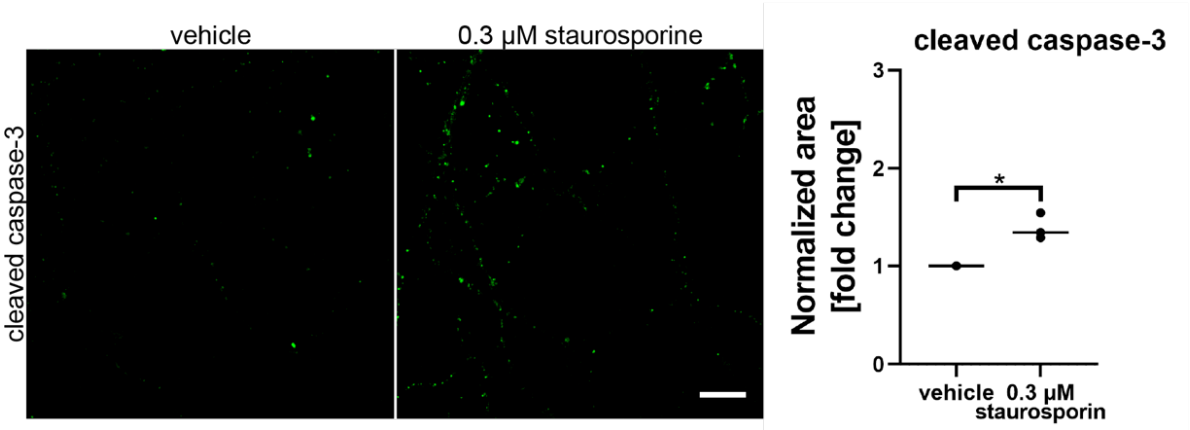

Fig. 37 Cleaved caspase-3 detection upon staurosporine treatment.
Immunofluorescence microscopy images and analysis of cleaved caspase-3 detection in axons treated with vehicle (0 µM hemin) and staurosporine (0.3 µM) as a positive control by fluorescence microscopy. Scale bar = 100 µm. The area covered by cleaved caspase-3 relative to the area of the axon was measured and then normalized to 0 hours. *N* = 4 biological replicates. * *P* < 0.05. Please see Table S10 in the appendix for statistical details.

Since the axonal swelling area was affected by 100 µM hemin after 6 hours and since caspase activation has been described to be upstream of axonal swelling formation in a model of nutrient deprivation[7], we investigated the expression of cleaved caspase-3 at time points prior and after changes of the axonal swelling area. The levels of cleaved

caspase-3 at 2, 4, and 8 hours of 100 µM hemin treatment were not different from axons subjected to vehicle treatment (**Fig. 38**). At 24 hours, the area positive for cleaved caspase-3 seemed to be increased but the increase was not statistically significant. Based on this data, the inhibition of apoptosis does not affect axonal morphology and the expression of cleaved caspase-3 is not changed in hemin-treated axons.

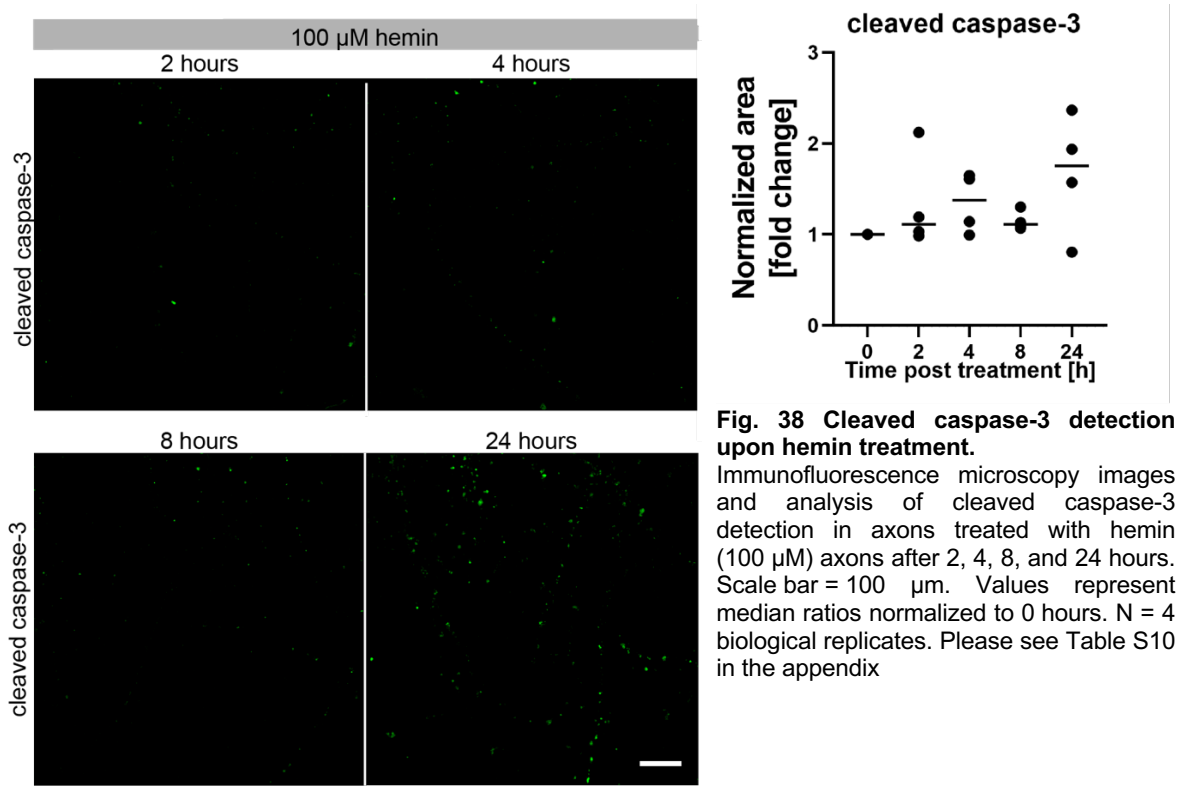

Fig. 38 Cleaved caspase-3 detection upon hemin treatment.
Immunofluorescence microscopy images and analysis of cleaved caspase-3 detection in axons treated with hemin (100 µM) axons after 2, 4, 8, and 24 hours. Scale bar = 100 µm. Values represent median ratios normalized to 0 hours. N = 4 biological replicates. Please see Table S10 in the appendix

3.3.7. Hemin-induced AxD may be mediated by ferroptosis

As hemin has been demonstrated to induce ferroptotic neuronal cell death in primary cortical neurons[79], we investigated whether the inhibition of ferroptosis also prevents AxD. We employed different chemical inhibitors that collectively define ferroptosis[126]: DFO, NAC, Fer-1, Trolox, U0126 (compared with its inactive control U0124) (**Fig. 39**). The investigated inhibitors did not substantially block hemin-induced AxD, except for DFO that increased the axon area in a concentration-dependent manner (for 100 µM, $P = 0.004$). It did not affect the axonal swelling and axonal fragment areas.

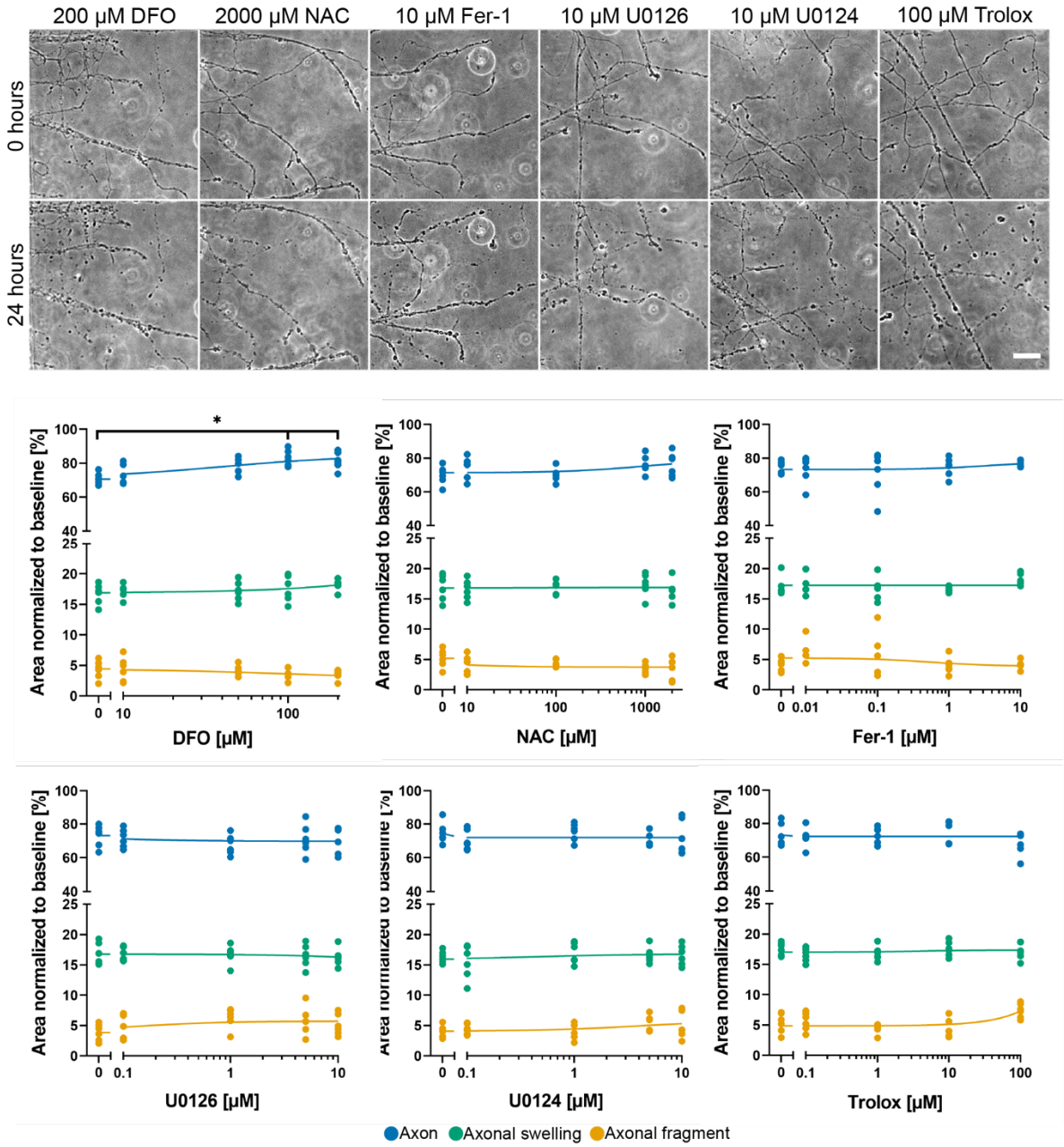

Fig. 39 Ferroptosis inhibitors do not prevent hemin-induced AxD.
Phase-contrast microscopy images of degenerating axons treated with hemin (100 µM) and ferroptosis inhibitors for 24 hours. Scale bar = 100 µm. Concentration-responses of ferroptosis inhibitors in hemin-treated axons at 24 hours. *N* = 6 biological replicates. Each biological replicate is displayed around the regression of axon (blue), axonal swelling (green) and axonal fragment (yellow). * $P < 0.05$ vs. 0 µM. Please see Table S11 in the appendix for statistical details.

Next, we investigated whether hemin induced the expression of the ferroptosis markers MDA and TfR1[127] (**Fig. 40**). MDA and TfR1 expression increased at 8, 16, and 24 hours compared to 0 hours ($P = 0.014$) in hemin-induced AxD. In summary, the increase of the axon area by DFO in hemin-induced AxD and the expression of the ferroptotic markers MDA and TfR1 suggest an axonal response to hemin treatment that may involve ferroptosis.

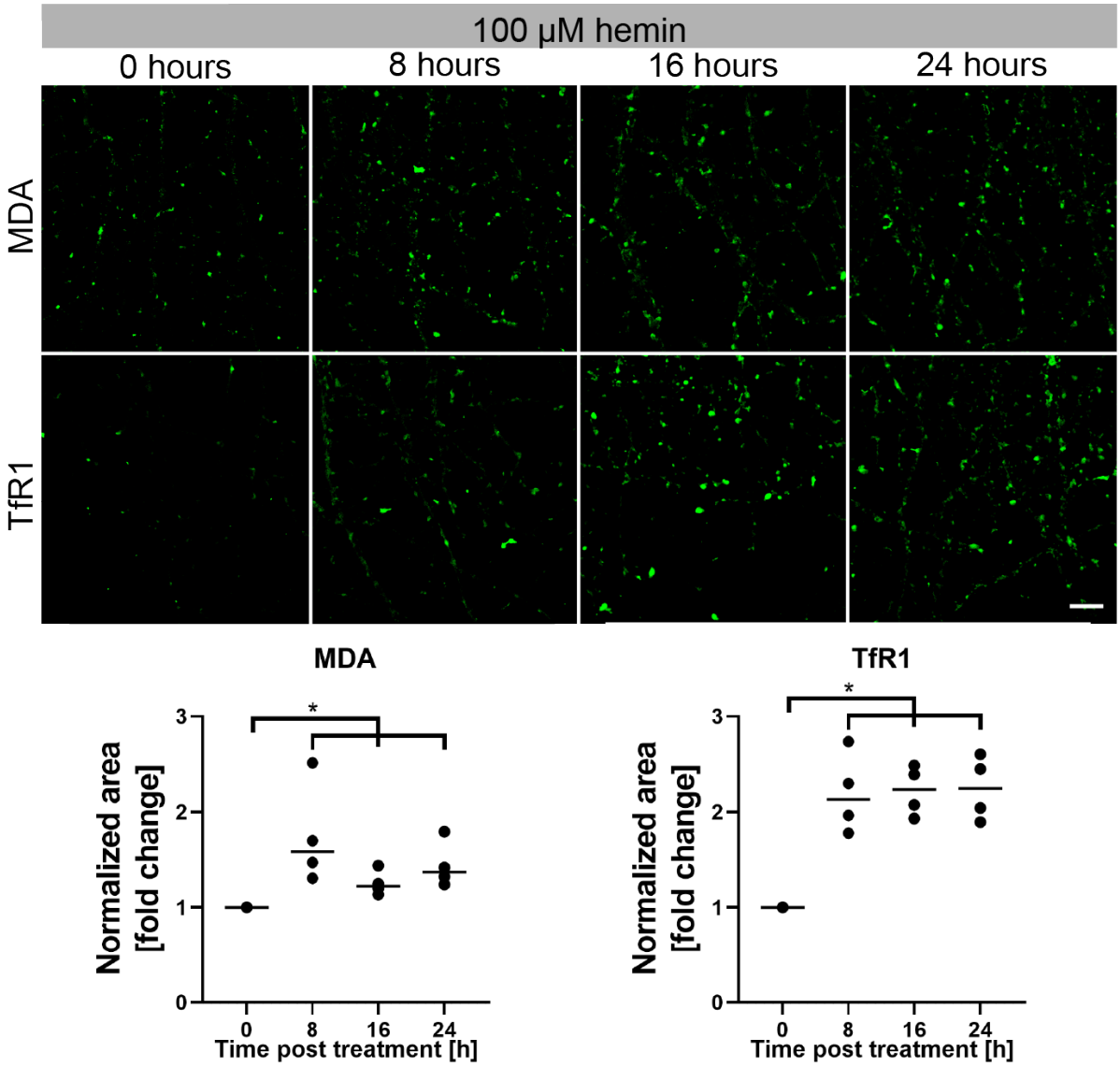

Fig. 40 MDA and TfR1 expression in hemin-induced AxD.
Axons were subjected to 100 µM hemin for 8, 16, and 24 hours and MDA as well as TfR1 immunofluorescence were assessed. Scale bar = 100 µm. MDA and TfR1 expression were analyzed by area relative to the area of the axon and then normalized to 0 hours. *N* = 4 biological replicates. * *P* < 0.017 for all time points due to manual Mann-Whitney U test correction of nonparametric data. Please see Table S12 in the appendix for statistical details.

3.3.8. Summary of the effects of chemical inhibitors on axonal morphology

The different molecular mechanisms underlying AxD have not been investigated in the context of hemolysis products such as hemin. We employed chemical inhibitors that addressed several molecular mechanisms, including inhibitors of calpain/cathepsin activity, transcription and translation, necroptosis, autophagy, apoptosis, and ferroptosis. However, none of the chemical inhibitors rescued the axonal morphology, while some even further exacerbated AxD (**Fig. 41**).

Model of Hemorrhagic Stroke				Axon area (IQR) [%]	Axonal swelling area (IQR) [%]	Axonal fragment area (IQR) [%]
Hemin Toxicity	Vehicle			107.45 (105.30, 110.80)	16.25 (15.52, 16.86)	0.63 (0.56, 0.77)
	100 µM Hemin			73.45 (72.40, 75.80)	17.05 (16.43, 17.34)	4.34 (3.99, 4.72)
Mechanism	**Inhibitor**	**Target**	**Conc.**	**Axon area (IQR) [%]**	**Axonal swelling area (IQR) [%]**	**Axonal fragment area (IQR) [%]**
Calpain and Cathepsin activity	ALLN	Calpain I/II and Cathepsin B/L	100 µM	58.06 (56.50, 60.69)	14.16 (12.46, 16.07)	8.21 (6.75, 9.42)
	E64d	Calpain I/II and Cathepsin B/H/L	100 µM	73.22 (64.96, 85.81)	16.46 (15.41, 18.82)	5.76 (3.14, 6.52)
	MDL28170	Calpain I/II/III and Cathepsin B	100 µM	61.34 (55.48, 57.07)	15.67 (14.01, 16.87)	7.93 (6.52, 10.00)
Transcription	Actinomycin D	mRNA synthesis	1 µM	69.42 (62.99, 79.76)	17.19 (16.70, 18.41)	5.26 (3.43, 7.44)
Translation	Cycloheximide	Protein synthesis	50 µM	56.79 (52.67, 65.47)	15.41 (13.00, 16.19)	8.00 (3.42, 9.57)
Necroptosis	GSK872	RIPK3	20 µM	72.98 (59.74, 81.05)	16.60 (15.35, 17.91)	4.86 (4.49, 8.98)
	NSA	MLKL	10 µM	63.52 (58.63, 70.76)	16.02 (15.23, 16.84)	8.24 (5.22, 8.72)
	Nec-1	RIPK1	100 µM	65.96 (57.34, 70.52)	16.32 (13.63, 17.13)	6.78 (5.23, 8.20)
	Nec-1i	Inactive Nec-1 analog	100 µM	67.52 (61.66, 73.61)	16.58 (14.31, 19.55)	5.52 (2.64, 6.96)
Autophagy	Bafilomycin A1	Lysosomal proton pump V-ATPase	0.1 µM	58.54 (48.89, 61.28)	15.27 (13.30, 15.95)	7.81 (5.29, 11.15)
Mitochondrial fission	Mdivi-1	GTPase activity in Drp1	100 µM	73.83 (69.96, 83.48)	16.14 (13.06, 17.42)	5.07 (3.54, 6.41)
Apoptosis	z-VAD-fmk	Caspases	100 µM	70.08 (63.05, 85.99)	16.81 (15.23, 17.79)	4.24 (2.49, 6.58)
Ferroptosis	DFO	Iron	200 µM	81.18 (73.74, 87.80)	18.28 (16.53, 19.27)	3.73 (2.06, 4.22)
	NAC	Reactive oxygen species (ROS)	2000 µM	75.93 (68.27, 86.04)	16.47 (13.93, 19.32)	4.11 (1.28, 5.60)
	Fer-1	Reactive lipid species (RLS)	10 µM	76.26 (74.74, 79.07)	17.80 (17.11, 19.53)	4.10 (3.04, 5.24)
	U0126	MEK 1/2	10 µM	72.85 (60.33, 77.49)	16.20 (14.42, 18.85)	4.66 (3.17, 7.51)
	U0124	Inactive U0126 analog	10 µM	68.35 (62.70, 85.44)	16.59 (14.54, 18.85)	4.28 (2.43, 7.86)
	Trolox	RLS	100 µM	70.06 (56.08, 73.78)	17.08 (15.18, 18.68)	7.44 (5.81, 8.86)

Fig. 41 The effects of the chemical inhibitors on axonal morphology.
Summarized effects of the chemical inhibitors at their highest concentration employed in this study in hemin-induced AxD. Numbers show medians and CI 95% for axon, axonal swelling, and axonal fragment area normalized to baseline (0 hours). The yellow-black coding indicates the continuum from intact axons (yellow) to degenerated axons (black).

3.3.9. Different effects of hemin on isolated axons and neurons

A previous study showed that the chemical inhibitors of ferroptosis and necroptosis protect neurons from hemin toxicity[79]. In our study, however, these chemical inhibitors did not rescue the axonal morphology in hemin-induced AxD. To discriminate between the molecular responses of neurons and isolated axons to hemin exposure, we statistically compared the effects of the applied chemical inhibitors between hemin-treated axons and neurons. We performed a Fisher's exact test upon extracting the data from Zille et al.[79] (**Table 14**). We considered a total of 15 chemical inhibitors. Fisher's exact test revealed that the protective effects of the chemical inhibitors differed between hemin-treated axons and neurons (P = 0.0063). In summary, the molecular effects of hemin on neurons and isolated axons are statistically different from each other.

Table 14 Chemical inhibitors preventing neuronal cell death do not rescue axons upon hemin exposure. x indicates protective, – indicates not protective.

	Protective in	
Chemical inhibitor	**Axons**	**Neurons**
Act-D	-	-
Chx	-	x
GSK872	-	-
NSA	-	-
Nec-1	-	x
Nec-1i	-	-
BafA1	-	-
Mdivi-1	-	-
z-VAD-fmk	-	-
DFO	-	x
NAC	-	x
Fer-1	-	x
U0126	-	x
U0124	-	-
Trolox	-	x

Fisher's exact test	two-tailed *P* = 0.0063		
2x2 contingency table	**Protective**	**Not protective**	Total
Axons	0	15	15
Neurons	7	8	15
Total	7	23	30

4. Discussion

In this study, we first developed two tools to analyze AxD. While the microfluidic device allowed the spatial separation of axons from their somata, the EntireAxon deep learning tool recognized the axonal morphology better than trained human evaluators. Using both tools, we quantified the concentration- and time-dependent appearance of the morphological hallmarks of AxD, namely axonal swellings and axonal fragments, in hemin-induced AxD. The exposure of axons to hemin led to their degeneration according to four morphological patterns of AxD. Attempts to rescue the axonal morphology with different chemical inhibitors revealed that hemin affects isolated axons differently from neurons. Different chemical inhibitors of calpain/cathepsin activity, transcription, translation, necroptosis, autophagy, apoptosis, and ferroptosis did not rescue hemin-induced AxD, while the ferroptosis markers MDA and TfR1 increased upon hemin exposure.

4.1. The monolithic microfluidic device standardizes the cultivation, treatment, and recording of isolated axons *in vitro*

To enhance the experimental throughput of AxD induction in spatially separated axons, we manufactured a monolithic microfluidic device composed of 16 single microfluidic systems that allows the isolated treatment and investigation of axons (**Fig. 17**). This microfluidic device outperforms currently available microfluidic devices that consist of only a single microfluidic system and therefore do not enable enhanced-throughput screenings[49,128].

Although a previously described, radial array of axonal compartments around a single soma compartment may increase the experimental yield[52], different treatments in the axonal compartments may affect the other treatment conditions. This is because the treatment may induce axonal retrograde signaling that leads to changes in the somata of these projecting axons. In turn, those neurons may release mediators into the somata compartment medium that affect neurons whose axons project into another axonal compartment. Another option is to use twelve individual microfluidic devices in parallel in a 12-well plate[53]. However, this approach requires more time in manufacturing and adjustments for recording. Our microfluidic device bypasses these limitations as it allows the parallelization of axonal cultivation and treatment due to its monolithic composition.

The microfluidic units were arranged to facilitate the seeding and treatment of multiple compartments at once with a multichannel pipette. The size of the compartments was selected to enable axonal outgrowth in high numbers for long-term cultivation and we successfully demonstrated that the cells survived up to 4 weeks in the devices (**Fig. 18**). However, axonal swellings started to appear at DIV11 despite changing the medium every three to four days. In some axons, the distal part degenerated two to three weeks later as demonstrated by the absence of calcein AM fluorescence (**Fig. 18**). According to another study using microfluidic devices, axons were electrophysiologically active *in vitro* at least up to DIV 28[129], which is in line with our observations.

As calcein AM is a vitality marker based on enzymatic conversion and does not measure axonal health *per se*, it may be possible that the axons may be compromised much before axonal enzymatic and electric activity are affected. Axonal metabolites such as nicotinamide mononucleotide (NMN) and nicotinamide adenine dinucleotide $(NAD)^+$, whose ratio determine the activation of AxD, may be useful parameters to investigate axonal health in future studies[130,131].

4.2. The EntireAxon CNN recognizes axons and the morphological hallmarks of AxD

Axonal health has so far been determined by quantifying axons and their fragments with image binarization in the context of AxD[57]. However, background noise removal in binarized images, for instance with ImageJ, can cause a significant loss of information (**Fig. 19**). Thus, results based on the detection of axons and axonal fragments are of low sensitivity and noisy, limiting firm conclusions. Furthermore, image binarization with ImageJ does not consider axonal swellings as an important morphological hallmark of AxD[7,132]. Previous attempts to analyze axonal swellings included the manual annotation of the region of interest at individual time points[7]. However, this procedure is time-consuming and subjective as manual annotations may differ among researchers. To thoroughly study AxD over time, the occurrence of axonal fragments and swellings needs to be investigated continuously, and analyses should be performed in an automated manner to ensure objective and fast quantification.

Current deep learning tools allow the objective and fast analysis of the axonal morphology in cross-sectional or three-dimensional images[59,60,133]. These tools are inspired by u-net architectures to extract microscopic features. The EntireAxon CNN

developed in this study was also based on a u-net architecture and was trained in a supervised manner with a dataset that resembled different scenarios of image acquisition and axonal morphology. Hence, the EntireAxon CNN learned to recognize axons, axonal swellings, and axonal fragments to decide the corresponding class for each pixel.

The EntireAxon CNN was able to learn the specific classes 'background', 'axon', 'axonal swelling', and 'axonal fragment' in phase-contrast microscopy images (**Fig. 20**). The class 'axonal fragment' had the lowest (mean) F1 score, resulting from the low recall value in this class. This means that the EntireAxon CNN recognized fewer axonal fragments than actually present. However, the EntireAxon CNN still outperformed trained human evaluators in recognizing axons, axonal swellings, and axonal fragments (**Table 12**).

Although we assessed the performance of the CNN compared to human evaluators by incorporating a consensus labeling between two evaluators, the EntireAxon CNN was still trained on labeled data from a single human evaluator. One possibility to increase the generalizability of the CNN would be to train it on training images with their respective consensus labels derived from the labeling of different human evaluators. However, manual labeling is very labor intense. Here, an active learning method, in which the CNN identifies the images with the best training performance ability[134], may be useful to reduce labeling time.

To the best of our knowledge, the EntireAxon CNN represents the only tool available so far to segment automatically axons and the morphological hallmarks of AxD (axonal swellings and axonal fragments) in two-dimensional phase-contrast images.

4.3. The occurrence of axonal swellings precedes the changes in axon and axonal fragment area in hemin-induced AxD

In the context of ICH, AxD is associated with poor motor and functional recovery[81,82] and therefore is of high interest to the field[135]. Electron microscopy revealed that axons start to degenerate and decrease their diameter three days after ICH in mice[80]. AxD endures until 28 days after ICH as axons show aberrations leading to a decrease of the number of axons and a loss of their myelination. The extended time window of three days may be enough to intervene with therapeutic strategies that address secondary injuries affecting axons. Thus, investigating axonal morphology can determine the extent and progression of AxD.

The progression of AxD has been subdivided into a latent and catastrophic phase in *in-vitro* models of injury and nutrient deprivation[7,8,136]. While the axon does not undergo morphological changes in the latent phase, axonal swellings emerge prior to the subsequent fragmentation of the axon in the catastrophic phase.

The morphological characterization of AxD by specifically considering the appearance of axonal swellings and fragments with the EntireAxon CNN revealed that both of these phases also prevail in our *in vitro* ICH model of hemin-induced AxD (**Fig. 24**). While the duration of the latent phase in axons treated with 50 µM hemin was 2 hours longer than in axons treated with 200 µM hemin, the duration of the catastrophic phase among both concentrations differed for at least 6 hours. In our model, the underlying reason for the time differences of the latent and catastrophic phase may be caused by the different concentrations. However, our findings also differed from findings in other models of AxD.

The duration of the latent phase in axons treated with 200 µM hemin was 12 hours shorter than in nutrient-deprived axons and 5 hours longer compared to injured axons of sympathetic neurons[8,136]. Interestingly, the duration of the catastrophic phase of injured and nutrient-deprived axons of sympathetic neurons was similar to axons treated with 200 µM hemin[8,136]. The comparison of the latent and catastrophic phases raises the question how degenerating axons regulate the formation of axonal swellings and axonal fragments.

In general, the determination of the transition from the latent to the catastrophic phase is based on the appearance of axonal swellings[7]. The increase of the relative axonal swelling area preceded the changes in the axon and axonal fragment area in hemin-induced AxD. This finding is partly in line with another study in which axonal swellings also preceded axonal fragmentation in an *in vivo* model of experimental autoimmune encephalomyelitis[6].

In our model, the spatially separated axons do not possess any myelin sheath. It could be argued that the axons may be more susceptible to insults due to the lack of myelin, which may serve as a protective sheet. However, myelin does not protect axons *per se* since demyelinated axons do not degenerate without any injury and are thought to be supported by the increased synthesis of neurotrophic factors from glia cells[137]. Although the isolated axons in our model were not co-cultivated with glial cells, the soma compartment may contain some glia cells as they cannot be fully eliminated during the cell preparation process. Neuron-glia interactions involve the shuttle of

lactate to ensure neuronal and axonal survival[138,139]. Indeed, it has been demonstrated that axon-glia metabolic coupling prevents AxD by a glycolytic adaptation of Schwann cells upon sciatic nerve injury[50]. Similar metabolic coupling between neurons and glia cells may have an effect in our model. Future studies should employ co-cultures and examine whether neuron-glia or axon-glia interactions affect the progression of hemin-induced AxD.

To allow a more sophisticated understanding of AxD in the context of ICH, future studies should also investigate the exposure of axons to other hemolysis products such as hemoglobin[140]. Although hemoglobin induces neuronal cell death in primary cortical and hippocampal neurons[79,141], its effect on axons is not known. Understanding the progression of AxD facilitates the search for potential new therapeutics.

4.4. The four morphological patterns of AxD potentially reveal a so far unknown intricacy in hemin-induced AxD

Axons exposed to hemin disintegrated according to four morphological patterns (**Fig. 26**). Each morphological pattern of AxD has been described in specific biological contexts: i) granular degeneration has been detected as an endpoint measure of pathological conditions (retrograde, anterograde, and Wallerian degeneration)[5,142–144]; ii) retraction degeneration has been characterized in the context of axonal development (retraction and shedding)[142,145]; iii) swelling degeneration has been observed in both development and disease models[6,7]; iv) transport degeneration has been described as a pathological consequence of microtubules breaking where axonal transport is impeded[146].

Using segmentation output maps from a new dataset of hemin-treated axons, we trained the EntireAxon RNN to recognize each of the four morphological patterns of AxD by detecting class changes over time (**Table 13**). While the EntireAxon RNN performed better for granular and swelling degeneration, retraction and transport degeneration had a lower mean F1 score. The underlying reason may be that retraction and transport degeneration represent more dynamic patterns as either the axon itself or the axonal swellings within the axon consistently change their position. The resulting spatiotemporal information may be too challenging for a correct recognition in this case.

Although different morphological patterns of AxD have been described in different experimental models, we here describe that multiple patterns can also occur at the

same time in one model (**Fig. 30**). This raises the question whether different neuronal subtypes give rise to the morphological patterns of AxD that may indicate different underlying mechanisms. For example, single-cell RNA sequencing revealed that subtypes of retinal ganglion cells were differently susceptible to degeneration upon optic nerve crush injury due to changes in gene expression[147]. This may also be the case in our model as our culture likely contained different neuronal subtypes.

Future studies should examine whether other chemo-toxic compounds such as vincristine or paclitaxel induce the morphological patterns of AxD described in our study. Furthermore, it should be investigated whether axons of specific neuronal subtypes differ in their degenerative processes. To this end, neuronal subtypes may be sorted using fluorescence-activated cell sorting and exposed to chemo-toxic compounds. Further analyses of the neuronal subtypes, that are responsive to a chemo-toxic compound and induce a specific morphological pattern, may be performed when harvesting these axons to subject them to molecular profiling using proteomics or metabolomics. Taken together, the EntireAxon RNN represents a helpful tool for further investigations that may unravel the underlying molecular mechanisms of each morphological pattern of AxD.

4.5. Chemical inhibitors do not rescue the axonal morphology in hemin-induced AxD

Hemin-induced AxD progressed differently depending on the hemin concentration. As 50 µM hemin did not lead to an increase in the relative axonal fragment area and 200 µM of hemin elevated the axonal fragment area eight hours prior to 100 µM hemin, we decided to evaluate the potential rescue of the axonal morphology in axons exposed to 100 µM hemin. This concentration has also been applied to study the molecular mechanisms of neuronal cell death in the context of ICH[79]. Thus, the choice of this concentration allowed us to compare the effects of the chemical inhibitors between both studies. However, Zille et al. employed conventional neuronal cell culture and did not spatially separate axons from their somata. The molecular investigation in Zille et al. does not exclude axons and the molecular effects of hemin on axons and somata cannot be precisely discriminated.

In our study, axons were co-treated with different chemical inhibitors in an isolated manner to rescue hemin-treated axons for 24 hours (**Fig. 32-36, 39**). The chemical inhibitors have been employed simultaneously with hemin to mimic the best-case

scenario in which axons are immediately treated with potential rescuing compounds. This may nevertheless be translated into the clinics as secondary injuries due to hemolysis occur after several hours or even days in patients[67]. Indeed, the scope of this part of our study was to rescue the axonal morphology in AxD and not to regenerate the axons upon hemin-induced AxD. The removal of hemin after 24 hours was not considered as AxD already occurred within 24 hours upon 100 µM hemin exposure.

4.5.1. Calpain/cathepsin inhibitors do not rescue the axonal morphology in hemin-induced AxD

In our study, the calpain and cathepsin inhibitors ALLN and MDL28170 aggravated AxD (**Fig. 32**). This is in contrast to findings in models of optic nerve injury and *in vitro* axotomy in which inhibiting calpain with calpastatin prevented AxD[148]. Differences in the specificity between the herein used calpain inhibitors and the previously used calpastatin may be a reason for our observation[10]. ALLN, E64d, and MDL28170 represent synthetic inhibitors that target the active site cysteine of calpains, while calpastatin is an endogenous inhibitor that also targets the active site cysteine of calpains but in a calcium-dependent manner[15,149].

However, cathepsin also possesses an active cysteine site and is involved in lysosomal cell death[150]. Thus, ALLN, E64d, and MDL28170 may also inhibit cathepsins[151–155]. Cathepsin has been detected in degradative lysosomes in axons of both primary cortical neurons and dorsal root ganglia[124]. Although gene expression and immunohistochemistry analyses revealed an increased expression of cathepsins upon spinal cord injury[156,157], none of the three inhibitors used in this study have been employed in other models of AxD.

Calcium-influx plays a pivotal role in AxD[9,15,18]. Intraaxonal calcium levels that determine the progression of AxD arise from either axonal plasma membrane ruptures as shown in a model of multiple sclerosis[9] or from intracellular storages of the ER[18]. The chelation of calcium prevented AxD in the multiple sclerosis model[9] and the knockdown of ER channels reduced the degeneration index upon both axotomy and chemotoxicity-induced AxD[18]. Thus, future studies should apply a combinatorial approach of calpain inhibitors, calcium chelators and intraaxonal calcium channel blockers to prevent hemin-induced AxD. This approach may exclude the activation of both synthetic and endogenous calcium-dependent calpains in hemin-induced AxD.

4.5.2. Inhibition of translation but not transcription aggravates axonal morphology in hemin-induced AxD

Axonal response to injury relies on nuclear transcription and local protein synthesis[51]. It may be possible that pro-degenerative transcripts or proteins are synthesized in hemin-induced AxD as is the case in developmental AxD[27,28,30].

It has been previously demonstrated that neither Act-D nor Chx change the cell viability of primary cortical neurons exposed to 100 µM hemin[79]. In our study, Act-D also did not affect the axonal morphology (**Fig. 33**).

In contrast, inhibiting overall transcription with Act-D has been demonstrated to decrease the expression of pro-apoptotic proteins that mediate AxD upon trophic withdrawal[121]. RNA sequencing in dorsal root ganglion axons revealed that the neuronal transcriptional response upon crush injury is attenuated[158].

Strikingly, inhibiting translation with Chx further aggravated hemin-induced AxD in our study (**Fig. 33**). Local axonal translation of proteins such as importin β1 has been reported and its translation can be inhibited by Chx[116]. Importin β1 plays a role in retrograde signaling to induce the transcription and translation of axonal and neuronal survival factors[51,116]. Thus, it may be possible that in our model Chx downregulated importin β1 or other locally translated proteins and prevented the retrograde signaling to synthesize pro-survival transcripts and proteins.

In future studies, Act-D and Chx should be applied individually in the axon and soma compartment to disentangle the contribution of transcription and translation in the axon and soma to hemin-induced AxD. Further RNA sequencing experiments should be performed to examine the transcriptional profiling of spatially separated axons and somata. These approaches will determine whether pro-survival or pro-degenerative signaling is involved in hemin-induced AxD.

4.5.3. AxD cannot be prevented by necroptosis inhibitors

Necroptosis has been shown to play a role in ICH. The inhibition of necroptosis in hemin-treated neurons led to increased neuronal survival[79]. Indeed, RIPK1 and RIPK3 were elevated in primary cortical neurons treated with 100 µM hemin and in a mouse model of ICH[79]. Genetic ablation of RIPK1 inactivating its kinase function ameliorated functional outcome in mice with ICH[159]. However, none of the necroptosis inhibitors prevented the axonal integrity loss after hemin exposure in our study (**Fig. 34**).

In previous studies, Nec-1 prevented AxD at four days upon *ex vivo* optic nerve injury, at 48 hours after *ex vivo* sciatic nerve injury, and at twelve hours upon *in vitro* axotomy and vinblastine treatment[41]. It may be possible that the protective effect of Nec-1 vanished after 24 hours in our model. To allow a more precise comparison between the effect of Nec-1 in axotomy-mediated AxD, vinblastine- and hemin-induced AxD, the axonal morphology in our model should also be investigated upon twelve hours and the role of Nec-1 upon axotomy and vinblastine treatment should be examined for 24 hours.

However, RIPK1 does not necessarily result in necroptosis. RIPK1 may also lead to apoptosis by the formation of the complexes IIa and IIb that involve caspase-8 (for review, see[160]). The necroptotic pathway is ultimately defined by the assembly of RIPK1 and RIPK3 that activate MLKL[42–45]. The participation of RIPK3 and MLKL in AxD has been confirmed by knockdown experiments[41]. RNA silencing of RIPK3 and MLKL via lentiviral shRNA delivery protected axons by 30 % upon axotomy and vinblastine treatment *in vitro* compared to axons receiving non-specific targeting shRNA[41]. In our model, RIPK3 and MLKL inhibitors did not rescue the axons.

Thus, further studies are needed to confirm the absence of the involvement of the necroptotic machinery in hemin-induced AxD. This may be feasible by investigating the phosphorylation of RIPK and MLKL as they are required for necroptosis execution[160]. As a positive control, isolated axons may be treated with TNF and z-VAD-fmk, which has been demonstrated to induce the expression of RIPK1 in HT22 cells as well as RIPK3 and MLKL in axons[41,79]. Such studies will help unravel the potential molecular regulation of necroptosis in hemin-induced AxD.

4.5.4. The inhibition of autophagy and mitophagy does not prevent hemin-induced AxD

ICH has been reported to induce autophagy. Western Blot analyses revealed the increased expression of the autophagic marker LC3-II in a rat ICH model[161]. The presence of autophagosomes in neurons after ICH in mice were confirmed by electron microscopy[80]. Recent findings also suggest the involvement of autophagy in AxD. Quantitative analyses of immunohistochemistry experiments of degenerating axons revealed an increased expression of autophagy-related genes at 24 hours after spinal cord injury[38]. The deletion of the autophagy-related gene 7 prevented chemotoxicity-induced axonal swelling formation and subsequent AxD[162]. As autophagy and

mitochondria dynamics are involved in AxD, we applied the autophagy inhibitor BafA1 and the mitochondrial fission inhibitor Mdivi-1 that did not rescue axons in hemin-induced AxD (**Fig. 35**).

The non-protective effect of BafA1 in hemin-treated axons in our study is in line with the observation that BafA1 does not protect primary cortical neurons from cell death upon hemin exposure[79]. Other autophagy inhibitors such as 3-methyladenine did not protect neurons either. However, hemin treatment of primary cortical neurons led to an increased expression of the autophagic marker LC3-II and the decreased expression of p62 suggesting the activation of autophagy[163]. The inhibition of autophagy with 3-methyladenine reversed the expression of these autophagic markers. The application of different hemin concentrations between Zille et al. and Shen et al. may be the possible underlying reason for the failure of BafA1 and 3-methyladenine to protect primary cortical neurons upon hemin exposure. Consequently, it may be possible that either AxD induction with 100 µM hemin for 24 hours is too harsh and counteracts any potential beneficial effect of BafA1 or autophagy inhibition with BafA1 over 24 hours leads to AxD.

As BafA1 inhibits the acidification of lysosomes[164], negatively affects axonal transport of autophagosomes[40,120], and prevents autophagosome clearance at the distal tip of axons of primary cortical neurons[124], the potential accumulation of axonal autophagosomes by BafA1 treatment in our model may be a reason for its non-protective effects in hemin-induced AxD. However, the 'autophagosome flux' also involves the synthesis of novel autophagosomes at the distal tip of the axon[165].

Although rapamycin represents an inducer of autophagy[166,167] and exerts axonal protection upon intraocular pressure in glaucoma models[168,169], the precise underlying mechanism is not known yet. For instance, it is not clear whether underlying feedback mechanisms regulate the clearance and biogenesis of autophagosomes in axonal autophagy during AxD.

Further studies are needed to examine whether autophagic markers such as LC3-II or p62 are expressed in a time-dependent manner during hemin-induced AxD. This may help to understand not only when autophagy is active during hemin-induced AxD but also if axons undergo a molecular switch after a certain time. Using molecular techniques such as evaluating gene expression and protein synthesis may be useful to further determine the activation of autophagy-related genes in the signaling pathway of axonal autophagy.

In our study, Mdivi-1 did not prevent hemin-induced AxD. However, our finding is solely based on the examination of the axonal morphology in phase-contrast microscopy and does not allow us to discriminate mitochondria-specific effects in hemin-induced AxD. In fact, Mdivi-1 has been demonstrated to act on mitochondria dynamics preventing mitochondrial fission[170]. A recent study reported the inhibition of AxD by Mdivi-1 upon axotomy and vinblastine treatment *in vitro*[41]. Mdivi-1 decreased mitochondrial number and increased mitochondrial size, which may hint towards an increase in mitochondrial fusion[171].

Future studies should characterize mitochondrial shape and size and track mitochondria by immunofluorescence tracing techniques. A genetic manipulation of mitochondrial fusion and fission proteins may further allow to determine how mitochondrial dynamics are related to hemin-induced AxD.

4.5.5. The caspase inhibitor z-VAD-fmk does not prevent hemin-induced AxD

In rat models of ICH, DNA fragmentation suggestive of apoptosis has been detected by Terminal deoxynucleotidyl transferase dUTP nick end labeling (TUNEL) in the striatum and hippocampus[172,173]. However, TUNEL staining cannot discriminate the molecular origin of DNA fragmentation. A recent study demonstrated that the expression of cleaved caspase-3, another marker of apoptosis, was significantly increased after ICH in rats[174]. The infusion of the broad spectrum caspase inhibitor z-VAD-fmk reduced the number of dead cells upon ICH, and improved the memory impairment after ICH *in vivo*[172,173].

However, in our *in vitro* model of ICH, z-VAD-fmk did not rescue the axonal morphology upon hemin treatment and cleaved caspase-3 expression was not detected in hemin-induced AxD (**Fig. 36**). These findings are in contrast to another study in which z-VAD-fmk prevented AxD, and cleaved caspase-3 was expressed and active in degenerating axons upon nutrient deprivation[119]. However, the inhibition of caspase-3 with z-DEVD-FMK and siRNA knockdown of caspase-3 did not prevent AxD in nutrient-deprived axons but prevented somatic cell death[27]. In contrast, blocking caspase-6 with z-VEID-FMK and the downregulation of caspase-6 by siRNA knockdown preserved axons upon nutrient deprivation but did not rescue the somata[27].

As z-VAD-fmk is a broad spectrum caspase inhibitor[118], the treatment of axons exposed to hemin may counteract the effects of caspase-3 and caspase-6 inhibition in hemin-induced AxD. In another study, Cusack and colleagues demonstrated that the genetic ablation of caspase-3 and caspase-6 in axons prevented AxD upon axon-

selective nutrient deprivation[28]. The authors concluded that the molecular regulation of apoptosis in AxD depends on whether both axons and somata or axons alone are deprived from nutrients[28]. In contrast, Nikolaev et al. proposed that caspase-3 leads to neuronal apoptosis while caspase-6 solely contributes to AxD[27].

In our positive control, the treatment of the somata with staurosporine induced the expression of cleaved caspase-3 in the axons suggesting an apoptotic response (**Fig. 37**). This finding is in line with a previous study reporting that staurosporine increases caspase-3 in nutrient-deprived axons of dorsal root ganglia explants[29]. However, chemotoxicity-induced AxD may be more comparable to hemin-induced AxD than nutrient deprivation. Indeed, the loss of caspase-3 did not protect axons treated with vincristine suggesting that caspase-3 does not contribute to vincristine-induced AxD[29].

A potential strategy to fully understand the involvement of caspases in AxD would be to genetically manipulate the activation of caspases in either axons or somata. Since caspase inhibitors have different specificity and potency for each caspase, future studies may also consider further caspase inhibitors[118]. For instance, the caspase inhibitor Q-VD-OPH has been demonstrated to prevent the cell death of serum-deprived primary cortical neurons more efficiently than Boc-D-fmk or z-VAD-fmk[117].

4.5.6. Targeting iron may be relevant to rescue hemin-treated axons

Ferroptosis is characterized by the peroxidation of polyunsaturated fatty acids due to the depletion of the glutathione peroxidase 4 (GPX4) enzyme, a peroxidase that converts lipid hydroperoxides to lipid alcohols, and the activation of lipoxygenases, which are iron-containing enzymes that oxidize polyunsaturated fatty acids into lipid hydroperoxides[175,176]. As lipid peroxidation is one of the hallmarks of ferroptosis, inhibiting reactive lipid species and contributing proteins and molecules such as mitogen-activated protein kinase kinase 1/2 (MEK1/2) and iron represent a promising strategy to prevent ferroptotic cell death[126,177].

Fer-1, an inhibitor of reactive lipid species, prevents neuronal cell death in organotypic hippocampal slice cultures upon hemoglobin and ferrous iron exposure, reduced MDA levels and improved functional outcome in an ICH mouse model[122]. In our *in vitro* ICH model, Fer-1 did not prevent hemin-induced AxD (**Fig. 39**). As Fer-1 treatment did not rescue AxD of dorsal root ganglia induced by the mitochondrial depolarizing agent carbonyl cyanide 3-chlorophenylhydrazone (CCCP)[178], it may be possible that the lack

of protection of Fer-1 does not involve mitochondrial dysfunction in hemin-induced AxD.

Further reactive lipid species inhibitors NAC and Trolox prevented ferroptosis in an *in vitro* ICH model of hemin-treated primary cortical neurons[179]. However, neither NAC nor Trolox rescued hemin-treated axons (**Fig. 39**). Trolox decreased superoxide levels in axotomized axons of dorsal root ganglia[18]. Villegas et al. suggested a model in which superoxide production depends on the elevation of calcium levels[18]. This model may be in line with the lacking effect of Trolox in our model, as the non-protective effects of the inhibitors addressing calcium-dependent calpain/cathepsin suggest that calcium may not be involved in our model and eventually superoxides may not be synthesized. However, future studies should directly address the contribution of calcium in hemin-induced AxD by using calcium chelators.

U0126 is another ferroptosis inhibitor that targets MEK1/2[177] . Although U0126 prevented hemin-induced neuronal ferroptosis[79], it did not hinder axons from degenerating upon hemin exposure (**Fig. 39**). While axons of superior cervical ganglia of Slow Wallerian degeneration (*Wld*^{S}) mutant mice are protected from axotomy, the application of U0126 led to AxD after 48 hours by off-target effects since alternative MEK inhibitors prevented AxD[180]. Although we applied the chemical inactive control of U0126, namely U0124, to exclude possible off-target effects of U0126 in our model, future studies should also employ alternative inhibitors of U0126.

The iron chelator DFO prevented ferroptosis in primary cortical neurons exposed to hemin[79] and rescued axons exposed to the ferroptosis inducer erastin in conventional cell culture[181]. In our model, DFO was the only chemical inhibitor to increase the axon area (**Fig. 39**). However, DFO did neither affect the axonal swelling area nor did it decrease the axonal fragment area. As in case of the other chemical ferroptosis inhibitors described above, axons fragmented after 24 hours in phase-contrast microscopy images suggesting that DFO may only delay hemin-induced AxD. In a model of spinal cord injury, DFO increased neuronal survival when administered prior to the injury and once daily in the subsequent seven days[182]. A pre-treatment and a continuous supply of DFO may also be beneficial in our model of hemin-induced AxD. Although it was not examined whether DFO affects the axonal morphology *per se*, molecular investigations in the spinal cord epicenters revealed a lower expression of glutathione peroxidase 4 and the cysteine-glutamate antiporter system X_c^- light chain that have been described to play a role in ferroptosis[182].

It has long been suggested that the protective effect of DFO in ferroptosis is mediated by its function to chelate iron (for review, see[176,177,183–185]). However, *in silico* modeling in combination with luminescence experiments showed that not iron chelation *per se* but the inhibition of the enzyme hypoxia-inducible factor prolyl hydroxylase domain (HIF-PHD) prevents ferroptosis[186]. Indeed, the decrease of HIF-PHD activity *in vivo* abrogated the activating transcription factor 4 (ATF4)-mediated transcription of pro-degenerative genes[177,186]. Although DFO has been identified as an inhibitor of HIF-PHD in a cell-based luciferase assay[187], the *in vivo* application in the brain of mice did not show any inhibitory activity[186]. In a phase-II clinical trial, DFO application did not improve outcome based on the modified ranking scale score in ICH patients[188]. Although the underlying reason has not fully been identified yet, one explanation may be that DFO also chelates iron that is required for the other functional enzymes.

Besides demonstrating protective effects of chemical inhibitors, the occurrence of ferroptosis can also be detected using the marker MDA[127]. In an ICH rat model, MDA levels were increased up to 14 days after the insult[189]. Since MDA is a product of lipid peroxidation, the involvement of lipid peroxidation in ICH has also been demonstrated by measuring the other lipid peroxidation product 4-hydroxynonenal (4-HNE). 4-HNE levels has been shown to be elevated 3 days after ICH in mice[190]. In an independent study, increased levels of 4-HNE have also been detected at 24 hours after ICH[191]. In our *in vitro* ICH model, the ferroptotic marker MDA was elevated in hemin-treated axons (**Fig. 40**). This finding suggests a role of lipid peroxidation in hemin-induced AxD.

Axonal lipid peroxidation has been detected upon spinal cord injury[192,193]. Using the thiobarbituric acid (TBA) test, a chemical analytical test to measure MDA by its interaction with TBA[194], spinal cord homogenates showed increased TBA reactive substances in cats and in rats[192,193]. A further study was able to detect the lipid peroxidation intermediates hydroperoxides in unsheathed axons of the sciatic nerve upon ischemia reperfusion[195]. However, it is still not clear yet whether axonal lipid peroxidation products originate from somatic or axonal lipids.

Further approaches to investigate the contribution of ferroptosis in hemin-induced AxD may rely on measuring the activity of the GPX4 enzyme and its inhibition as GPX4 reduces lipid peroxides into lipid alcohols[175,196]. GPX4 overexpression in ICH has been demonstrated to counteract the formation of reactive oxygen species and improved neuronal survival[197]. In an experimental autoimmune encephalomyelitis mouse model,

GPX4 mRNA and protein levels and lipid peroxidation products have been decreased in the spinal cords[198]. It may be possible that the upregulation of the GPX4 enzyme protects axons upon hemin exposure.

In addition to MDA, ferroptosis can also be assessed by TfR1 detection as TfR1 serves as an antigen in ferroptosis and was highly expressed in a fibrosarcoma cell line upon ferroptosis induction[127]. Rats experiencing ICH also showed elevated levels of the ferroptosis marker TfR1 after 3 days[68]. In our study, TfR1 expression was increased in hemin-induced AxD (**Fig. 40**). This finding implies the contribution of ferroptosis in hemin-induced AxD and raises the question whether hemin-treated axons can autonomously regulate their iron uptake.

A previous study using Campenot chambers and immunoprecipitation reported the transcytosis of transferrin-bound iron from dendrites and somata to axons and the upregulation of axonal TfR1[199]. In contrast to our model, in which only the axons have been treated with the iron-containing hemin, Hémar et al. treated the somata with bound transferrin-iron and did not investigate whether bound transferrin-iron on either somata or axons elevated axonal TfR1[199]. It may be possible that axonal TfR1 upregulation is mediated by iron that enters the axons either bound to transferrin or via the cytosol by the divalent metal transporter 1 (DMT1) after being released from hemin due to interactions between hemin and the axonal plasma membrane[200].

Alternatively, iron may be taken up by axons within the hemin chemical structure and is subsequently released into the axonal cytosol due to hemin degradation[201]. Measurements of radioactive hemin in cell lysates revealed that primary cortical neurons take up hemin[77]. Neuronal hemin uptake is controlled by the heme carrier protein 1 (HCP1)[202].

Future investigations should aim at a detailed understanding of the role of iron in AxD. A radioactive iron isotope may be used in addition to iron-chelating agents such as DFO or ethylenediaminetetraacetic acid to confirm whether iron is taken up in axons by TfR1[203]. This may help to understand whether the upregulation of axonal TfR1 expression is a specific response to iron stemming from hemin. To further examine the potential entry routes, the experimental conditions should be controlled for exogenous transferrin present in the medium and the expression of hemin-specific transporters such as HCP1, and potential axonal plasma membrane ruptures should be investigated (**Fig. 42**).

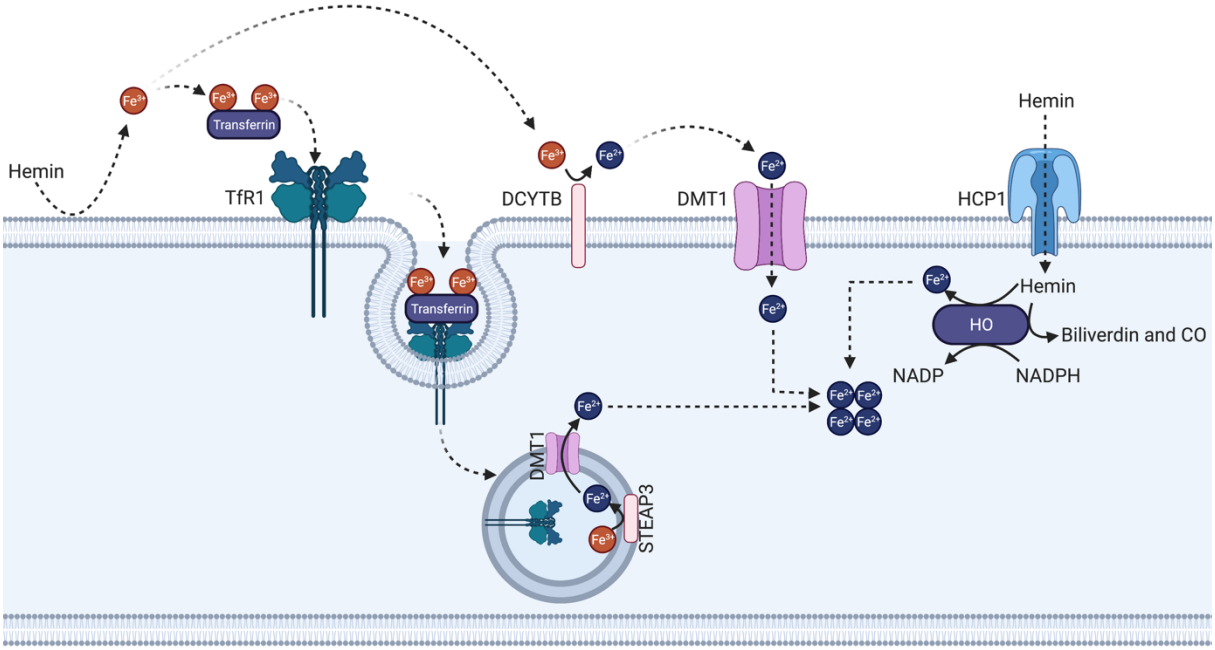

Fig. 42 Potential axonal iron and hemin uptake.
The interaction of hemin with the axonal plasma membrane releases ferric iron that is either oxidized by duodenal cytochrome B (DCYTB) and transported into DMT1 or bound to transferrin and taken up by TfR1. Eventually, the ferric iron is oxidized to ferrous iron via the six-transmembrane epithelial antigen of prostate 3 (STEAP3) metalloreductase and transported into the cytosol through DMT1. Upon uptake of ferric iron-containing hemin by HCP1, hemin is catabolized by heme oxygenase (HO) to biliverdin and carbon monoxide (CO) resulting in the release of ferrous iron in the cytosol.

4.5.7. Differences of hemin-induced neuronal death and AxD

Finally, we statistically compared hemin-induced neuronal death and AxD, which were significantly different from each other. In both cases, somata and axons were exposed to the chemical inhibitors. However, the location of the insult differed between both studies as axons have selectively been exposed to hemin in our model while in the conventional cell culture model of Zille et al., somata and axons were treated with hemin[79].

Different pathway signals may be activated depending on the deprivation of either somata and axons together or axons alone[28]. Although somata and axons are molecularly connected by antero- and retrograde injury signaling[51], axons are also capable to regulate their local protein synthesis autonomously[204]. In a model of sciatic nerve injury, the protein mechanistic target of rapamycin was synthesized in axons and regulated the local translation of importin β1 and signal transducer and activator of transcription 3 in axons[205].

To exclude the possibility that hemin-treated axons fail to sustain themselves by a lack of local protein synthesis and retrograde injury signaling, future studies may investigate the transcriptome and proteome of axons in hemin-induced AxD.

However, the somata should also be investigated as they represent the site of signal integration[51]. In a model of nutrient deprivation, the genetic ablation of signaling molecules in nutrient-deprived axons upregulated pro-degenerative factors in the somata that led to AxD[30]. Simon et al. argued that the retrograde injury signaling activated a somatic response that induced an anterograde pro-degenerative signal[30]. Future studies may use fluorescently-tagged signaling molecules to trace the transport of retrograde injury signals in hemin-induced AxD. The same approach may be used to examine whether hemin-treated somata induce anterograde injury signals that are potentially transported to untreated axons. This approach will help to understand whether injury signals do not reach the somata or axon in time in this model, in which the distal parts of the axons are spatially separated from their somata over several hundreds of micrometers.

Injury signals may also be associated with regeneration. In a model of axotomy of dorsal root ganglion axons, HIF-1α induces the expression of regenerative genes[206]. As HIF-1α knockdown or knockout fail to regenerate axons *in vitro* and *in vivo*[206], it may be interesting to investigate whether HIF-PHD activation affects the somatic or axonal translation of HIF-1α- and ATF4-dependent transcripts upon hemin exposure. Such investigations are necessary since therapeutic strategies addressing axons and somata individually will be clinically challenging and neurons need to be considered as a whole.

4.6. Limitations

Our studies have a number of limitations:

i) The design of the herein presented microfluidic device does not allow to induce AxD more proximally to the soma and hampers the harvesting of axons for molecular profiling. Axotomy proximal to the somata led to an increased loss of rubrospinal neurons and facial motor neurons compared to more distal axotomy[207,208]. Indeed, the location of AxD either at main, ascending, or descending axonal branches affected the progression of AxD and regenerative potential of axons of the spinal cord[209]. In our model of hemin-induced AxD, we observed differences between thin and thick axons. However, we were not able to detect the location of the insult since the axons are exposed to hemin in their whole length.

The impact of different AxD locations on the outcome can be investigated by either reducing the length of the microgrooves, including a third compartment that is more

proximal, or using an open structure of the compartments, in which axons can be injured at different locations. The open structure of the compartments inspired by the design of the Campenot chambers may facilitate harvesting axons for molecular analyses. These approaches may help to understand regional differences in the axonal responses to injury in more detail.

ii) In this study, axons were treated with chemical inhibitors and hemin simultaneously for 24 hours. We are uncertain whether treating axons with the chemical inhibitors for different time periods may have resulted in axonal protection. For example, bortezomib-treated axons of dorsal root ganglia were not protected by Act-D and z-VAD-fmk treatment within 24 hours[210]. However, both inhibitors showed a protective effect starting from 36 and 48 hours, respectively. Since they were added one hour prior to the bortezomib treatment, we cannot exclude the possibility that a pre-treatment may have affected the progression of AxD.

Furthermore, we cannot confirm whether the ferroptotic inhibitor DFO either delayed the start of the catastrophic phase of hemin-induced AxD or indeed rescued the axonal morphology. A pre-treatment of hemin-treated axons and a longer time period of co-treatment with the chemical inhibitors may be a further option to examine either the rescuing effect of the chemical inhibitors or the potential effect of delaying the catastrophic phase of hemin-induced AxD.

iii) This study did not investigate the metabolic regulation during hemin-induced AxD. In a neuroinflammatory glaucoma model, the SARM1 inhibitors SCG10 and NMAT2 were lost in axonal necroptosis and SARM1 executed its NADase activity[46]. It may be possible that, for instance, NAD^+ consumption by SARM1 protein contributes to hemin-induced AxD (for review, see[47]). NAD^+ levels declined in axons of dorsal root ganglia upon axotomy due to increased NAD^+ consumption by the NDAse activity of SARM1[211]. The genetic ablation of SARM1 also prevented NAD^+ consumption in chemotoxicity-induced AxD by vincristine and bortezomib in axons of dorsal root ganglia[210]. As SARM1 is involved in AxD in different biological scenarios, addressing SARM1 may be a potential strategy to rescue the axonal morphology in hemin-induced AxD.

Future studies may use the two proposed tools from this study to examine differences in the progression, morphology and molecular mechanisms of hemin-induced AxD in axons of primary cortical neurons from $SARM1^{-/-}$ mice. Further measurements of metabolites such as NAD^+ may help indicating how hemin affects axonal metabolism.

4.8. Conclusion

This study reveals the morphological characteristics of AxD in an *in vitro* model of ICH using a novel fabricated microfluidic device and new deep learning tool. The “EntireAxon” deep learning tool expands our possibilities to track AxD by detecting axons, axonal swellings and axonal fragments and allows the characterization of the morphology of AxD. The demise of axons according to the four morphological patterns of AxD reveals a morphological heterogeneity that needs to be further examined in the future. Despite using chemical inhibitors that address different molecular mechanism, axons exposed to hemin were not rescued.

Taken together, this study underlines the relevancy of characterizing axonal morphology to understand AxD. The herein presented findings and tools may benefit researchers in the axonal biology field to discriminate more precisely the progression of AxD in different *in vitro* models. This will generate a more profound understanding of AxD in the context of ICH and other neurological diseases that may form the basis for the development of novel therapeutic approaches.

5. Acknowledgments

Who am I without consciousness? Who am I without blood supply? Who am I without neighboring cells? Who am I without other organs? Who am I without the surrounding system? It is me the axon.

This section is devoted to the people who supported me during the last couple of years. Without you, I would have been degenerated like an axon.

Prof. Dr. Dr. Johannes Boltze and Dr. Marietta Zille are the mentors that I needed to grow as a scientist and a human being and represent the unparalleled example of unconditional sacrifice. I adore their genuine kindness, their openness to new ideas and their calmness in stressful situations. I admire their ability to instill their humble astuteness and moral and ethical principles into the minds of their students. I thank them for their never ending patience and the indescribable support from the first day. I thank them for believing in me from the beginning of this journey, supplying me with the blood in the form of faith and awaking my consciousness every time I am in deep sleep. Thanks to them, I build up the neural circuits.

Lara Eleen Heckmann, Svenja Kim Landt, Alessa Pabst, Luisa Bartram, Charlotte Flory, Yamil Abdala Villanueva Maluje and Maulana Ikhsan represent the neighboring neurons. I thank them for offering me the support and discussions throughout this period. Thanks to them, I know which neurotransmitter I have to release.

PD Dr. Amir Madany Mamlouk, Philipp Grüning supported me in the sense of glia cells. I thank them for fueling essential energy and knowledge in the area of deep learning into this study. Thanks to them, I was able to visualize this study as a computer.

The involvement of Sören Pietsch, Reinhard Schulz, Norbert Koop, and Christopher Kren in this study show that interdisciplinarity and collaborations enable to tackle challenges of any size if several organs unify. I thank all of them for their interest and investing their resources. Thanks to them, I was able to connect to fields outside of my system.

The Fraunhofer Research Institution of Marine Biotechnology and Cell Technology and the Institute for Experimental and Clinical Pharmacology and Toxicology of the University of Lübeck both represent the body. I thank Prof. Dr. Charli Kruse and Prof. Dr. Markus Schwaninger for offering me the infrastructure of their institutes to conduct this study. Thanks to them, I was able to function within the system.

To all other people that I encountered during this time: I thank you.

6. Bibliography

1. Azevedo, F. A. C. *et al.* Equal numbers of neuronal and nonneuronal cells make the human brain an isometrically scaled-up primate brain. *J. Comp. Neurol.* **513**, 532–541 (2009).
2. *Principles of neural science*. (McGraw-Hill, 2013).
3. Salvadores, N., Sanhueza, M., Manque, P. & Court, F. A. Axonal Degeneration during Aging and Its Functional Role in Neurodegenerative Disorders. *Front. Neurosci.* **11**, 451 (2017).
4. Krauss, R., Bosanac, T., Devraj, R., Engber, T. & Hughes, R. O. Axons Matter: The Promise of Treating Neurodegenerative Disorders by Targeting SARM1-Mediated Axonal Degeneration. *Trends in Pharmacological Sciences* **41**, 281–293 (2020).
5. Coleman, M. P. Axon degeneration mechanisms: commonality amid diversity. *Nat Rev Neurosci* **6**, 889–898 (2005).
6. Nikić, I. *et al.* A reversible form of axon damage in experimental autoimmune encephalomyelitis and multiple sclerosis. *Nat Med* **17**, 495–499 (2011).
7. Yong, Y. *et al.* p75NTR and DR6 Regulate Distinct Phases of Axon Degeneration Demarcated by Spheroid Rupture. *J. Neurosci.* **39**, 9503–9520 (2019).
8. Yong, Y., Gamage, K., Cushman, C., Spano, A. & Deppmann, C. Regulation of degenerative spheroids after injury. *Sci Rep* **10**, 15472 (2020).
9. Witte, M. E. *et al.* Calcium Influx through Plasma-Membrane Nanoruptures Drives Axon Degeneration in a Model of Multiple Sclerosis. *Neuron* **101**, 615-624.e5 (2019).
10. Ma, M. Role of calpains in the injury-induced dysfunction and degeneration of the mammalian axon. *Neurobiology of Disease* **60**, 61–79 (2013).
11. Stys, P., Waxman, S. & Ransom, B. Ionic mechanisms of anoxic injury in mammalian CNS white matter: role of Na+ channels and Na(+)-Ca2+ exchanger. *J. Neurosci.* **12**, 430–439 (1992).
12. Stys, P. K., Sontheimer, H., Ransom, B. R. & Waxman, S. G. Noninactivating, tetrodotoxin-sensitive Na+ conductance in rat optic nerve axons. *Proceedings of the National Academy of Sciences* **90**, 6976–6980 (1993).
13. Iwata, A. *et al.* Traumatic axonal injury induces proteolytic cleavage of the voltage-gated sodium channels modulated by tetrodotoxin and protease inhibitors. *J Neurosci* **24**, 4605–4613 (2004).
14. Kamakura, K., Ishiura, S., Sugita, H. & Toyokura, Y. Identification of Ca2+-activated neutral protease in the peripheral nerve and its effects on neurofilament degeneration. *J Neurochem* **40**, 908–913 (1983).
15. Hanna, R. A., Campbell, R. L. & Davies, P. L. Calcium-bound structure of calpain and its mechanism of inhibition by calpastatin. *Nature* **456**, 409–412 (2008).
16. von Reyn, C. R., Mott, R. E., Siman, R., Smith, D. H. & Meaney, D. F. Mechanisms of calpain mediated proteolysis of voltage gated sodium channel α-subunits following in vitro dynamic stretch injury: Mechanisms of calpain mediated NaCh proteolysis. *Journal of Neurochemistry* **121**, 793–805 (2012).
17. Barrientos, S. A. *et al.* Axonal Degeneration Is Mediated by the Mitochondrial Permeability Transition Pore. *Journal of Neuroscience* **31**, 966–978 (2011).
18. Villegas, R. *et al.* Calcium Release from Intra-Axonal Endoplasmic Reticulum Leads to Axon Degeneration through Mitochondrial Dysfunction. *Journal of Neuroscience* **34**, 7179–7189 (2014).
19. Kamakura, K., Ishiura, S., Suzuki, K., Sugita, H. & Toyokura, Y. Calcium-activated neutral protease in the peripheral nerve, which requires microM order Ca2+, and its effect on the neurofilament triplet. *J Neurosci Res* **13**, 391–403 (1985).
20. Malik, M. N., Fenko, M. D., Iqbal, K. & Wisniewski, H. M. Purification and characterization of two forms of Ca2+-activated neutral protease from calf brain. *J Biol Chem* **258**, 8955–8962 (1983).
21. Schlaepfer, W. W., Lee, C., Lee, V. M. & Zimmerman, U. J. An immunoblot study of neurofilament degradation in situ and during calcium-activated proteolysis. *J Neurochem* **44**, 502–509 (1985).
22. Billger, M., Wallin, M. & Karlsson, J. O. Proteolysis of tubulin and microtubule-associated proteins 1 and 2 by calpain I and II. Difference in sensitivity of assembled and disassembled microtubules. *Cell Calcium* **9**, 33–44 (1988).
23. Sorimachi, H., Hata, S. & Ono, Y. Expanding Members and Roles of the Calpain Superfamily and Their Genetically Modified Animals. *Exp. Anim.* **59**, 549–566 (2010).
24. Kroemer, G. *et al.* Classification of cell death: recommendations of the Nomenclature Committee on Cell Death 2009. *Cell Death Differ* **16**, 3–11 (2009).
25. Galluzzi, L. *et al.* Molecular mechanisms of cell death: recommendations of the Nomenclature Committee on Cell Death 2018. *Cell Death Differ* **25**, 486–541 (2018).

26. Singh, R., Letai, A. & Sarosiek, K. Regulation of apoptosis in health and disease: the balancing act of BCL-2 family proteins. *Nat Rev Mol Cell Biol* **20**, 175–193 (2019).
27. Nikolaev, A., McLaughlin, T., O'Leary, D. D. M. & Tessier-Lavigne, M. APP binds DR6 to trigger axon pruning and neuron death via distinct caspases. *Nature* **457**, 981–989 (2009).
28. Cusack, C. L., Swahari, V., Hampton Henley, W., Michael Ramsey, J. & Deshmukh, M. Distinct pathways mediate axon degeneration during apoptosis and axon-specific pruning. *Nat Commun* **4**, 1876 (2013).
29. Simon, D. J. *et al.* A Caspase Cascade Regulating Developmental Axon Degeneration. *Journal of Neuroscience* **32**, 17540–17553 (2012).
30. Simon, D. J. *et al.* Axon Degeneration Gated by Retrograde Activation of Somatic Pro-apoptotic Signaling. *Cell* **164**, 1031–1045 (2016).
31. Mizushima, N. & Komatsu, M. Autophagy: Renovation of Cells and Tissues. *Cell* **147**, 728–741 (2011).
32. Maday, S., Wallace, K. E. & Holzbaur, E. L. F. Autophagosomes initiate distally and mature during transport toward the cell soma in primary neurons. *Journal of Cell Biology* **196**, 407–417 (2012).
33. Maday, S. & Holzbaur, E. L. F. Autophagosome Biogenesis in Primary Neurons Follows an Ordered and Spatially Regulated Pathway. *Developmental Cell* **30**, 71–85 (2014).
34. Fu, M., Nirschl, J. J. & Holzbaur, E. L. F. LC3 Binding to the Scaffolding Protein JIP1 Regulates Processive Dynein-Driven Transport of Autophagosomes. *Developmental Cell* **29**, 577–590 (2014).
35. Wang, Q. J. *et al.* Induction of autophagy in axonal dystrophy and degeneration. *J Neurosci* **26**, 8057–8068 (2006).
36. White, K. E. *et al.* OPA1 Deficiency Associated with Increased Autophagy in Retinal Ganglion Cells in a Murine Model of Dominant Optic Atrophy. *Invest. Ophthalmol. Vis. Sci.* **50**, 2567 (2009).
37. Knöferle, J. *et al.* Mechanisms of acute axonal degeneration in the optic nerve in vivo. *Proceedings of the National Academy of Sciences* **107**, 6064–6069 (2010).
38. Ribas, V. T. *et al.* Early and Sustained Activation of Autophagy in Degenerating Axons after Spinal Cord Injury: Autophagy Activation in Spinal Cord Damaged Axons. *Brain Pathology* **25**, 157–170 (2015).
39. Vahsen, B. F. *et al.* Inhibition of the autophagic protein ULK1 attenuates axonal degeneration in vitro and in vivo, enhances translation, and modulates splicing. *Cell Death Differ* **27**, 2810–2827 (2020).
40. Lee, S., Sato, Y. & Nixon, R. A. Lysosomal Proteolysis Inhibition Selectively Disrupts Axonal Transport of Degradative Organelles and Causes an Alzheimer's-Like Axonal Dystrophy. *Journal of Neuroscience* **31**, 7817–7830 (2011).
41. Arrázola, M. S. *et al.* Axonal Degeneration Is Mediated by Necroptosis Activation. *J. Neurosci.* **39**, 3832–3844 (2019).
42. Li, J. *et al.* The RIP1/RIP3 Necrosome Forms a Functional Amyloid Signaling Complex Required for Programmed Necrosis. *Cell* **150**, 339–350 (2012).
43. Sun, L. *et al.* Mixed Lineage Kinase Domain-like Protein Mediates Necrosis Signaling Downstream of RIP3 Kinase. *Cell* **148**, 213–227 (2012).
44. Wu, X.-N. *et al.* Distinct roles of RIP1–RIP3 hetero- and RIP3–RIP3 homo-interaction in mediating necroptosis. *Cell Death Differ* **21**, 1709–1720 (2014).
45. Wang, H. *et al.* Mixed Lineage Kinase Domain-like Protein MLKL Causes Necrotic Membrane Disruption upon Phosphorylation by RIP3. *Molecular Cell* **54**, 133–146 (2014).
46. Ko, K. W., Milbrandt, J. & DiAntonio, A. SARM1 acts downstream of neuroinflammatory and necroptotic signaling to induce axon degeneration. *Journal of Cell Biology* **219**, e201912047 (2020).
47. Gerdts, J., Summers, D. W., Milbrandt, J. & DiAntonio, A. Axon Self-Destruction: New Links among SARM1, MAPKs, and NAD+ Metabolism. *Neuron* **89**, 449–460 (2016).
48. Campenot, R. B. Development of sympathetic neurons in compartmentalized cultures. *Developmental Biology* **93**, 13–21 (1982).
49. Park, J. W., Vahidi, B., Taylor, A. M., Rhee, S. W. & Jeon, N. L. Microfluidic culture platform for neuroscience research. *Nat Protoc* **1**, 2128–2136 (2006).
50. Babetto, E., Wong, K. M. & Beirowski, B. A glycolytic shift in Schwann cells supports injured axons. *Nat Neurosci* **23**, 1215–1228 (2020).
51. Rishal, I. & Fainzilber, M. Axon–soma communication in neuronal injury. *Nat Rev Neurosci* **15**, 32–42 (2014).
52. Park, J., Koito, H., Li, J. & Han, A. Multi-compartment neuron–glia co-culture platform for localized CNS axon–glia interaction study. *Lab Chip* **12**, 3296 (2012).
53. Li, Y. *et al.* AxonQuant: A Microfluidic Chamber Culture-Coupled Algorithm That Allows High-Throughput Quantification of Axonal Damage. *Neurosignals* **22**, 14–29 (2014).
54. Loreto, A. *et al.* Mitochondrial impairment activates the Wallerian pathway through depletion of

NMNAT2 leading to SARM1-dependent axon degeneration. *Neurobiology of Disease* **134**, 104678 (2020).
55. Chen, M. *et al.* A new method for quantifying mitochondrial axonal transport. *Protein Cell* **7**, 804–819 (2016).
56. Dong, A., Kulkarni, V. V. & Maday, S. Methods for Imaging Autophagosome Dynamics in Primary Neurons. in *Autophagy* (eds. Ktistakis, N. & Florey, O.) vol. 1880 243–256 (Springer New York, 2019).
57. Sasaki, Y., Vohra, B. P. S., Lund, F. E. & Milbrandt, J. Nicotinamide Mononucleotide Adenylyl Transferase-Mediated Axonal Protection Requires Enzymatic Activity But Not Increased Levels of Neuronal Nicotinamide Adenine Dinucleotide. *Journal of Neuroscience* **29**, 5525–5535 (2009).
58. Pease-Raissi, S. E. *et al.* Paclitaxel Reduces Axonal Bclw to Initiate IP3R1-Dependent Axon Degeneration. *Neuron* **96**, 373-386.e6 (2017).
59. Zaimi, A. *et al.* AxonDeepSeg: automatic axon and myelin segmentation from microscopy data using convolutional neural networks. *Sci Rep* **8**, 3816 (2018).
60. Ritch, M. D. *et al.* AxoNet: A deep learning-based tool to count retinal ganglion cell axons. *Sci Rep* **10**, 8034 (2020).
61. Schubert, P. J., Dorkenwald, S., Januszewski, M., Jain, V. & Kornfeld, J. Learning cellular morphology with neural networks. *Nat Commun* **10**, 2736 (2019).
62. Moen, E. *et al.* Deep learning for cellular image analysis. *Nat Methods* **16**, 1233–1246 (2019).
63. Keep, R. F., Hua, Y. & Xi, G. Intracerebral haemorrhage: mechanisms of injury and therapeutic targets. *The Lancet Neurology* **11**, 720–731 (2012).
64. Xi, G., Keep, R. F. & Hoff, J. T. Mechanisms of brain injury after intracerebral haemorrhage. *The Lancet Neurology* **5**, 53–63 (2006).
65. Mendelow, A. *et al.* Early surgery versus initial conservative treatment in patients with spontaneous supratentorial lobar intracerebral haematomas (STICH II): a randomised trial. *The Lancet* **382**, 397–408 (2013).
66. Hanley, D. F. *et al.* Efficacy and safety of minimally invasive surgery with thrombolysis in intracerebral haemorrhage evacuation (MISTIE III): a randomised, controlled, open-label, blinded endpoint phase 3 trial. *The Lancet* **393**, 1021–1032 (2019).
67. Aronowski, J. & Zhao, X. Molecular Pathophysiology of Cerebral Hemorrhage: Secondary Brain Injury. *Stroke* **42**, 1781–1786 (2011).
68. Wu, J. *et al.* Iron and Iron-Handling Proteins in the Brain After Intracerebral Hemorrhage. *Stroke* **34**, 2964–2969 (2003).
69. Wagner, K. R., Sharp, F. R., Ardizzone, T. D., Lu, A. & Clark, J. F. Heme and Iron Metabolism: Role in Cerebral Hemorrhage. *J Cereb Blood Flow Metab* **23**, 629–652 (2003).
70. van Wijk, R. & van Solinge, W. W. The energy-less red blood cell is lost: erythrocyte enzyme abnormalities of glycolysis. *Blood* **106**, 4034–4042 (2005).
71. Brantley, R. E., Smerdon, S. J., Wilkinson, A. J., Singleton, E. W. & Olson, J. S. The mechanism of autooxidation of myoglobin. *J Biol Chem* **268**, 6995–7010 (1993).
72. Shikama, K. The Molecular Mechanism of Autoxidation for Myoglobin and Hemoglobin: A Venerable Puzzle. *Chem. Rev.* **98**, 1357–1374 (1998).
73. Reeder, B. J. The Redox Activity of Hemoglobins: From Physiologic Functions to Pathologic Mechanisms. *Antioxidants & Redox Signaling* **13**, 1087–1123 (2010).
74. Svistunenko, D. A. Reaction of haem containing proteins and enzymes with hydroperoxides: The radical view. *Biochimica et Biophysica Acta (BBA) - Bioenergetics* **1707**, 127–155 (2005).
75. Kassa, T., Jana, S., Meng, F. & Alayash, A. I. Differential heme release from various hemoglobin redox states and the upregulation of cellular heme oxygenase-1. *FEBS Open Bio* **6**, 876–884 (2016).
76. Regan, R. F., Chen, J. & Benvenisti-Zarom, L. Heme oxygenase-2 gene deletion attenuates oxidative stress in neurons exposed to extracellular hemin. *BMC Neurosci* **5**, 34 (2004).
77. Chen-Roetling, J., Cai, Y., Lu, X. & Regan, R. F. Hemin uptake and release by neurons and glia. *Free Radical Research* **48**, 200–205 (2014).
78. Zhou, Y.-F. *et al.* Hepcidin Protects Neuron from Hemin-Mediated Injury by Reducing Iron. *Front. Physiol.* **8**, 332 (2017).
79. Zille, M. *et al.* Neuronal Death After Hemorrhagic Stroke In Vitro and In Vivo Shares Features of Ferroptosis and Necroptosis. *Stroke* **48**, 1033–1043 (2017).
80. Li, Q. *et al.* Ultrastructural Characteristics of Neuronal Death and White Matter Injury in Mouse Brain Tissues After Intracerebral Hemorrhage: Coexistence of Ferroptosis, Autophagy, and Necrosis. *Front. Neurol.* **9**, 581 (2018).
81. Venkatasubramanian, C. *et al.* Natural History and Prognostic Value of Corticospinal Tract Wallerian Degeneration in Intracerebral Hemorrhage. *JAHA* **2**, (2013).
82. Chen, X. *et al.* The Impact of Intracerebral Hemorrhage on the Progression of White Matter

Hyperintensity. *Front. Hum. Neurosci.* **12**, 471 (2018).
83. Welniarz, Q., Dusart, I. & Roze, E. The corticospinal tract: Evolution, development, and human disorders: Corticospinal Tract Human Disorders. *Devel Neurobio* **77**, 810–829 (2017).
84. Weibel, D. B., DiLuzio, W. R. & Whitesides, G. M. Microfabrication meets microbiology. *Nat Rev Microbiol* **5**, 209–218 (2007).
85. Xia, Y. *et al.* Replica molding using polymeric materials: A practical step toward nanomanufacturing. *Adv. Mater.* **9**, 147–149 (1997).
86. Qin, D., Xia, Y. & Whitesides, G. M. Soft lithography for micro- and nanoscale patterning. *Nat Protoc* **5**, 491–502 (2010).
87. Whitesides, G. M., Ostuni, E., Takayama, S., Jiang, X. & Ingber, D. E. Soft Lithography in Biology and Biochemistry. *Annu. Rev. Biomed. Eng.* **3**, 335–373 (2001).
88. McDonald, J. C. & Whitesides, G. M. Poly(dimethylsiloxane) as a Material for Fabricating Microfluidic Devices. *Acc. Chem. Res.* **35**, 491–499 (2002).
89. Lee, J. N., Jiang, X., Ryan, D. & Whitesides, G. M. Compatibility of mammalian cells on surfaces of poly(dimethylsiloxane). *Langmuir* **20**, 11684–11691 (2004).
90. Tan, S. H., Nguyen, N.-T., Chua, Y. C. & Kang, T. G. Oxygen plasma treatment for reducing hydrophobicity of a sealed polydimethylsiloxane microchannel. *Biomicrofluidics* **4**, 032204 (2010).
91. Zhou, J., Ellis, A. V. & Voelcker, N. H. Recent developments in PDMS surface modification for microfluidic devices. *Electrophoresis* **31**, 2–16 (2010).
92. Bowman, A. J., Scherrer, J. R. & Reiserer, R. S. Note: A single-chamber tool for plasma activation and surface functionalization in microfabrication. *Review of Scientific Instruments* **86**, 066106 (2015).
93. Dehmelt, L. & Halpain, S. The MAP2/Tau family of microtubule-associated proteins. *Genome Biol* **6**, 204 (2004).
94. Wiedenmann, B. & Franke, W. W. Identification and localization of synaptophysin, an integral membrane glycoprotein of Mr 38,000 characteristic of presynaptic vesicles. *Cell* **41**, 1017–1028 (1985).
95. Miles, F., Lynch, J. & Sikes, R. Cell-based assays using calcein acetoxymethyl ester show variation in fluorescence with treatment conditions. *J Biol Methods* **2**, 29 (2015).
96. Phansalkar, N., More, S., Sabale, A. & Joshi, M. Adaptive local thresholding for detection of nuclei in diversity stained cytology images. in *2011 International Conference on Communications and Signal Processing* 218–220 (IEEE, 2011). doi:10.1109/ICCSP.2011.5739305.
97. Yang, G. R. & Wang, X.-J. Artificial Neural Networks for Neuroscientists: A Primer. *Neuron* **107**, 1048–1070 (2020).
98. Lee, J. *et al.* Deep Learning in Medical Imaging: General Overview. *Korean J Radiol* **18**, 570 (2017).
99. Rojas, R. *Neural Networks*. (Springer Berlin Heidelberg, 1996). doi:10.1007/978-3-642-61068-4.
100. Hastie, T., Tibshirani, R. & Friedman, J. *The Elements of Statistical Learning*. (Springer New York, 2009). doi:10.1007/978-0-387-84858-7.
101. Aloysius, N. & Geetha, M. A review on deep convolutional neural networks. in *2017 International Conference on Communication and Signal Processing (ICCSP)* 0588–0592 (IEEE, 2017). doi:10.1109/ICCSP.2017.8286426.
102. Shorten, C. & Khoshgoftaar, T. M. A survey on Image Data Augmentation for Deep Learning. *J Big Data* **6**, 60 (2019).
103. Zhou, Z.-H., Wu, J. & Tang, W. Ensembling neural networks: Many could be better than all. *Artificial Intelligence* **137**, 239–263 (2002).
104. He, K., Zhang, X., Ren, S. & Sun, J. Deep Residual Learning for Image Recognition. *arXiv:1512.03385 [cs]* (2015).
105. Bishop, C. M. *Neural networks for pattern recognition*. (Clarendon Press ; Oxford University Press, 1995).
106. Ronneberger, O., Fischer, P. & Brox, T. U-Net: Convolutional Networks for Biomedical Image Segmentation. *arXiv:1505.04597 [cs]* (2015).
107. Forman, G. & Scholz, M. Apples-to-apples in cross-validation studies: pitfalls in classifier performance measurement. *SIGKDD Explor. Newsl.* **12**, 49 (2010).
108. Lowe, D. G. Distinctive Image Features from Scale-Invariant Keypoints. *International Journal of Computer Vision* **60**, 91–110 (2004).
109. Palumbo, A. *et al. Deep learning to decipher the progression and morphology of axonal degeneration*. http://biorxiv.org/lookup/doi/10.1101/2020.08.26.269092 (2020) doi:10.1101/2020.08.26.269092.
110. Lipton, Z. C., Berkowitz, J. & Elkan, C. A Critical Review of Recurrent Neural Networks for Sequence Learning. *arXiv:1506.00019 [cs]* (2015).

111. Chung, J., Gulcehre, C., Cho, K. & Bengio, Y. Empirical Evaluation of Gated Recurrent Neural Networks on Sequence Modeling. *arXiv:1412.3555 [cs]* (2014).
112. Hochreiter, S. & Schmidhuber, J. Long Short-Term Memory. *Neural Computation* **9**, 1735–1780 (1997).
113. Cho, K., van Merrienboer, B., Bahdanau, D. & Bengio, Y. On the Properties of Neural Machine Translation: Encoder-Decoder Approaches. *arXiv:1409.1259 [cs, stat]* (2014).
114. Bengio, Y., Simard, P. & Frasconi, P. Learning long-term dependencies with gradient descent is difficult. *IEEE Trans. Neural Netw.* **5**, 157–166 (1994).
115. You, Y. *et al.* Large Batch Optimization for Deep Learning: Training BERT in 76 minutes. *arXiv:1904.00962 [cs, stat]* (2020).
116. Hanz, S. *et al.* Axoplasmic Importins Enable Retrograde Injury Signaling in Lesioned Nerve. *Neuron* **40**, 1095–1104 (2003).
117. Chauvier, D. *et al.* Upstream control of apoptosis by caspase-2 in serum-deprived primary neurons. *Apoptosis* **10**, 1243–1259 (2005).
118. Chauvier, D., Ankri, S., Charriaut-Marlangue, C., Casimir, R. & Jacotot, E. Broad-spectrum caspase inhibitors: from myth to reality? *Cell Death Differ* **14**, 387–391 (2007).
119. Schoenmann, Z. *et al.* Axonal Degeneration Is Regulated by the Apoptotic Machinery or a NAD+-Sensitive Pathway in Insects and Mammals. *Journal of Neuroscience* **30**, 6375–6386 (2010).
120. Wang, T. *et al.* Control of Autophagosome Axonal Retrograde Flux by Presynaptic Activity Unveiled Using Botulinum Neurotoxin Type A. *J. Neurosci.* **35**, 6179–6194 (2015).
121. Maor-Nof, M. *et al.* Axonal Degeneration Is Regulated by a Transcriptional Program that Coordinates Expression of Pro- and Anti-degenerative Factors. *Neuron* **92**, 991–1006 (2016).
122. Li, Q. *et al.* Inhibition of neuronal ferroptosis protects hemorrhagic brain. *JCI Insight* **2**, e90777 (2017).
123. Kilinc, D., Gallo, G. & Barbee, K. A. Mechanical membrane injury induces axonal beading through localized activation of calpain. *Experimental Neurology* **219**, 553–561 (2009).
124. Farfel-Becker, T. *et al.* Neuronal Soma-Derived Degradative Lysosomes Are Continuously Delivered to Distal Axons to Maintain Local Degradation Capacity. *Cell Reports* **28**, 51-64.e4 (2019).
125. Belmokhtar, C. A., Hillion, J. & Ségal-Bendirdjian, E. Staurosporine induces apoptosis through both caspase-dependent and caspase-independent mechanisms. *Oncogene* **20**, 3354–3362 (2001).
126. Dixon, S. J. *et al.* Ferroptosis: An Iron-Dependent Form of Nonapoptotic Cell Death. *Cell* **149**, 1060–1072 (2012).
127. Feng, H. *et al.* Transferrin Receptor Is a Specific Ferroptosis Marker. *Cell Reports* **30**, 3411-3423.e7 (2020).
128. Van Laar, V., Arnold, B. & Berman, S. Primary Embryonic Rat Cortical Neuronal Culture and Chronic Rotenone Treatment in Microfluidic Culture Devices. *BIO-PROTOCOL* **9**, (2019).
129. Hong, N., Joo, S. & Nam, Y. Characterization of Axonal Spikes in Cultured Neuronal Networks Using Microelectrode Arrays and Microchannel Devices. *IEEE Trans. Biomed. Eng.* **64**, 492–498 (2017).
130. Sasaki, Y., Nakagawa, T., Mao, X., DiAntonio, A. & Milbrandt, J. NMNAT1 inhibits axon degeneration via blockade of SARM1-mediated NAD+ depletion. *eLife* **5**, e19749 (2016).
131. Figley, M. D. *et al.* SARM1 is a metabolic sensor activated by an increased NMN/NAD+ ratio to trigger axon degeneration. *Neuron* S0896627321000830 (2021) doi:10.1016/j.neuron.2021.02.009.
132. Cui, Y. *et al.* Axonal degeneration in an in vitro model of ischemic white matter injury. *Neurobiology of Disease* **134**, 104672 (2020).
133. Wang, Y. *et al.* TeraVR empowers precise reconstruction of complete 3-D neuronal morphology in the whole brain. *Nat Commun* **10**, 3474 (2019).
134. Grüning, P., Palumbo, A., Zille, M., Barth, E., & Madany Mamlouk, Amir. A task-dependent active learning method for axon segmentation with CNNs. *Proc AUTOMED* **1**, (2020).
135. Hemorrhagic Stroke Academia Industry (HEADS) Roundtable Participants. Basic and Translational Research in Intracerebral Hemorrhage: Limitations, Priorities, and Recommendations. *Stroke* **49**, 1308–1314 (2018).
136. Gamage, K. K. *et al.* Death Receptor 6 Promotes Wallerian Degeneration in Peripheral Axons. *Current Biology* **27**, 890–896 (2017).
137. Smith, C. M., Cooksey, E. & Duncan, I. D. Myelin Loss Does Not Lead to Axonal Degeneration in a Long-Lived Model of Chronic Demyelination. *Journal of Neuroscience* **33**, 2718–2727 (2013).
138. Magistretti, P. J. & Pellerin, L. The astrocyte-mediated coupling between synaptic activity and energy metabolism operates through volume transmission. in *Progress in Brain Research* vol. 125 229–240 (Elsevier, 2000).
139. Lee, Y. *et al.* Oligodendroglia metabolically support axons and contribute to neurodegeneration. *Nature* **487**, 443–448 (2012).
140. Schaer, D. J., Buehler, P. W., Alayash, A. I., Belcher, J. D. & Vercellotti, G. M. Hemolysis and

free hemoglobin revisited: exploring hemoglobin and hemin scavengers as a novel class of therapeutic proteins. *Blood* **121**, 1276–1284 (2013).
141. Garland, P. *et al.* Haemoglobin causes neuronal damage in vivo which is preventable by haptoglobin. *Brain Communications* **2**, fcz053 (2020).
142. Neukomm, L. J. & Freeman, M. R. Diverse cellular and molecular modes of axon degeneration. *Trends in Cell Biology* **24**, 515–523 (2014).
143. Cavanagh, J. B. The 'dying back' process. A common denominator in many naturally occurring and toxic neuropathies. *Arch. Pathol. Lab. Med.* **103**, 659–664 (1979).
144. Beirowski, B. *et al.* The progressive nature of Wallerian degeneration in wild-type and slow Wallerian degeneration (WldS) nerves. *BMC Neurosci* **6**, 6 (2005).
145. Pease, S. E. & Segal, R. A. Preserve and protect: maintaining axons within functional circuits. *Trends in Neurosciences* **37**, 572–582 (2014).
146. Tang-Schomer, M. D., Johnson, V. E., Baas, P. W., Stewart, W. & Smith, D. H. Partial interruption of axonal transport due to microtubule breakage accounts for the formation of periodic varicosities after traumatic axonal injury. *Experimental Neurology* **233**, 364–372 (2012).
147. Tran, N. M. *et al.* Single-Cell Profiles of Retinal Ganglion Cells Differing in Resilience to Injury Reveal Neuroprotective Genes. *Neuron* **104**, 1039-1055.e12 (2019).
148. Yang, J. *et al.* Regulation of Axon Degeneration after Injury and in Development by the Endogenous Calpain Inhibitor Calpastatin. *Neuron* **80**, 1175–1189 (2013).
149. Pietsch, M., Chua, K. & Abell, A. Calpains: Attractive Targets for the Development of Synthetic Inhibitors. *CTMC* **10**, 270–293 (2010).
150. Tang, D., Kang, R., Berghe, T. V., Vandenabeele, P. & Kroemer, G. The molecular machinery of regulated cell death. *Cell Res* **29**, 347–364 (2019).
151. Sasaki, T. *et al.* Inhibitory Effect of di- and Tripeptidyl Aldehydes on Calpains and Cathepsins. *Journal of Enzyme Inhibition* **3**, 195–201 (1990).
152. Hiwasa, T., Sawada, T. & Sakiyama, S. Cysteine proteinase inhibitors and *ras* gene products share the same biological activities including tranforming activity toward NIH3T3 mouse fibroblasts and the differentiation-inclucing activity toward PC12 rat pheochromocytoma cells. *Carcinogenesis* **11**, 75–80 (1990).
153. Baek, K. H., Karki, R., Lee, E.-S., Na, Y. & Kwon, Y. Synthesis and investigation of dihydroxychalcones as calpain and cathepsin inhibitors. *Bioorganic Chemistry* **51**, 24–30 (2013).
154. Kartkaya, K., Kanbak, G., Oğlakçı, A., Burukoğlu, D. & Özer, M. C. Protective effect of calpain inhibitor N-acetyl-l-leucyl-l-leucyl-l-norleucinal on acute alcohol consumption related cardiomyopathy. *Mol Biol Rep* **41**, 6743–6753 (2014).
155. Dana, D. & Pathak, S. K. A Review of Small Molecule Inhibitors and Functional Probes of Human Cathepsin L. *Molecules* **25**, 698 (2020).
156. Ellis, R. C., Earnhardt, J. N., Hayes, R. L., Wang, K. K. W. & Anderson, D. K. Cathepsin B mRNA and protein expression following contusion spinal cord injury in rats: Cathepsin B expression after spinal cord injury. *Journal of Neurochemistry* **88**, 689–697 (2003).
157. Sun, L. *et al.* Cathepsin B-dependent motor neuron death after nerve injury in the adult mouse. *Biochem Biophys Res Commun* **399**, 391–395 (2010).
158. Perry, R. B.-T. *et al.* Subcellular Knockout of Importin β1 Perturbs Axonal Retrograde Signaling. *Neuron* **75**, 294–305 (2012).
159. Lule, S. *et al.* Genetic Inhibition of Receptor Interacting Protein Kinase-1 Reduces Cell Death and Improves Functional Outcome After Intracerebral Hemorrhage in Mice. *Stroke* **48**, 2549–2556 (2017).
160. Chen, J., Kos, R., Garssen, J. & Redegeld, F. Molecular Insights into the Mechanism of Necroptosis: The Necrosome as a Potential Therapeutic Target. *Cells* **8**, 1486 (2019).
161. He, Y. *et al.* Induction of autophagy in rat hippocampus and cultured neurons by iron. *Acta Neurochir Suppl* **105**, 29–32 (2008).
162. Cheng, H.-C. *et al.* Akt suppresses retrograde degeneration of dopaminergic axons by inhibition of macroautophagy. *J Neurosci* **31**, 2125–2135 (2011).
163. Shen, X. *et al.* Autophagy regulates intracerebral hemorrhage induced neural damage via apoptosis and NF-κB pathway. *Neurochem Int* **96**, 100–112 (2016).
164. Klionsky, D. J., Elazar, Z., Seglen, P. O. & Rubinsztein, D. C. Does bafilomycin A $_1$ block the fusion of autophagosomes with lysosomes? *Autophagy* **4**, 849–850 (2008).
165. Maday, S. Mechanisms of neuronal homeostasis: Autophagy in the axon. *Brain Research* **1649**, 143–150 (2016).
166. Sarkar, S., Ravikumar, B., Floto, R. A. & Rubinsztein, D. C. Rapamycin and mTOR-independent autophagy inducers ameliorate toxicity of polyglutamine-expanded huntingtin and related proteinopathies. *Cell Death Differ* **16**, 46–56 (2009).
167. Lin, X., Han, L., Weng, J., Wang, K. & Chen, T. Rapamycin inhibits proliferation and induces

autophagy in human neuroblastoma cells. *Bioscience Reports* **38**, BSR20181822 (2018).
168. Kitaoka, Y. *et al.* Axonal protection by Nmnat3 overexpression with involvement of autophagy in optic nerve degeneration. *Cell Death Dis* **4**, e860–e860 (2013).
169. Munemasa, Y. & Kitaoka, Y. Autophagy in axonal degeneration in glaucomatous optic neuropathy. *Progress in Retinal and Eye Research* **47**, 1–18 (2015).
170. Cassidy-Stone, A. *et al.* Chemical inhibition of the mitochondrial division dynamin reveals its role in Bax/Bak-dependent mitochondrial outer membrane permeabilization. *Dev Cell* **14**, 193–204 (2008).
171. Westermann, B. Mitochondrial fusion and fission in cell life and death. *Nat Rev Mol Cell Biol* **11**, 872–884 (2010).
172. Matsushita, K. *et al.* Evidence for Apoptosis After Intracerebral Hemorrhage in Rat Striatum. *J Cereb Blood Flow Metab* **20**, 396–404 (2000).
173. Hwang, L. *et al.* Dexmedetomidine ameliorates intracerebral hemorrhage-induced memory impairment by inhibiting apoptosis and enhancing brain-derived neurotrophic factor expression in the rat hippocampus. *International Journal of Molecular Medicine* **31**, 1047–1056 (2013).
174. Wang, L., Tian, M. & Hao, Y. Role of p75 neurotrophin receptor in neuronal autophagy in intracerebral hemorrhage in rats through the mTOR signaling pathway. *Cell Cycle* **19**, 376–389 (2020).
175. Stockwell, B. R. *et al.* Ferroptosis: A Regulated Cell Death Nexus Linking Metabolism, Redox Biology, and Disease. *Cell* **171**, 273–285 (2017).
176. Dixon, S. J. & Stockwell, B. R. The Hallmarks of Ferroptosis. *Annu. Rev. Cancer Biol.* **3**, 35–54 (2019).
177. Ratan, R. R. The Chemical Biology of Ferroptosis in the Central Nervous System. *Cell Chemical Biology* **27**, 479–498 (2020).
178. Summers, D. W., DiAntonio, A. & Milbrandt, J. Mitochondrial Dysfunction Induces Sarm1-Dependent Cell Death in Sensory Neurons. *Journal of Neuroscience* **34**, 9338–9350 (2014).
179. Karuppagounder, S. S. *et al.* N-acetylcysteine targets 5 lipoxygenase-derived, toxic lipids and can synergize with prostaglandin E_2 to inhibit ferroptosis and improve outcomes following hemorrhagic stroke in mice: NAC Synergizes With PGE_2 to Improve Outcomes After ICH. *Ann Neurol.* **84**, 854–872 (2018).
180. Evans, C., Cook, S. J., Coleman, M. P. & Gilley, J. MEK inhibitor U0126 reverses protection of axons from Wallerian degeneration independently of MEK-ERK signaling. *PLoS One* **8**, e76505 (2013).
181. Zhang, Y. *et al.* Neuroprotective effect of deferoxamine on erastininduced ferroptosis in primary cortical neurons. *Neural Regen Res* **15**, 1539 (2020).
182. Yao, X. *et al.* Deferoxamine promotes recovery of traumatic spinal cord injury by inhibiting ferroptosis. *Neural Regen Res* **14**, 532 (2019).
183. Liu, Z. D., Liu, D. Y. & Hider, R. C. Iron Chelator Chemistry. in *Iron Chelation Therapy* (ed. Hershko, C.) vol. 509 141–166 (Springer US, 2002).
184. Ayala, A., Muñoz, M. F. & Argüelles, S. Lipid Peroxidation: Production, Metabolism, and Signaling Mechanisms of Malondialdehyde and 4-Hydroxy-2-Nonenal. *Oxidative Medicine and Cellular Longevity* **2014**, 1–31 (2014).
185. Raines, D. J., Sanderson, T. J., Wilde, E. J. & Duhme-Klair, A.-K. Siderophores. in *Reference Module in Chemistry, Molecular Sciences and Chemical Engineering* B9780124095472110000 (Elsevier, 2015). doi:10.1016/B978-0-12-409547-2.11040-6.
186. Karuppagounder, S. S. *et al.* Therapeutic targeting of oxygen-sensing prolyl hydroxylases abrogates ATF4-dependent neuronal death and improves outcomes after brain hemorrhage in several rodent models. *Sci. Transl. Med.* **8**, 328ra29-328ra29 (2016).
187. Smirnova, N. A. *et al.* Utilization of an In Vivo Reporter for High Throughput Identification of Branched Small Molecule Regulators of Hypoxic Adaptation. *Chemistry & Biology* **17**, 380–391 (2010).
188. Selim, M. *et al.* Deferoxamine mesylate in patients with intracerebral haemorrhage (i-DEF): a multicentre, randomised, placebo-controlled, double-blind phase 2 trial. *The Lancet Neurology* **18**, 428–438 (2019).
189. Han, N., Ding, S.-J., Wu, T. & Zhu, Y.-L. Correlation of free radical level and apoptosis after intracerebral hemorrhage in rats. *Neurosci. Bull.* **24**, 351–358 (2008).
190. Wang, Y. *et al.* miR-183-5p alleviates early injury after intracerebral hemorrhage by inhibiting heme oxygenase-1 expression. *Aging (Albany NY)* **12**, 12869–12895 (2020).
191. Zhao, X. *et al.* Transcription Factor Nrf2 Protects the Brain From Damage Produced by Intracerebral Hemorrhage. *Stroke* **38**, 3280–3286 (2007).
192. Milvy, P., Kakari, S., Campbell, J. B. & Demopoulos, H. B. Paramagnetic species and radical products in cat spinal cord. *Ann N Y Acad Sci* **222**, 1102–1111 (1973).
193. Kurihara, M. Role of monoamines in experimental spinal cord injury in rats. Relationship between Na+-K+-ATPase and lipid peroxidation. *J Neurosurg* **62**, 743–749 (1985).

194. Gutteridge, J. M. & Halliwell, B. The measurement and mechanism of lipid peroxidation in biological systems. *Trends Biochem Sci* **15**, 129–135 (1990).
195. Nagamatsu, M. *et al.* Ischemic reperfusion causes lipid peroxidation and fiber degeneration. *Muscle Nerve* **19**, 37–47 (1996).
196. Ursini, F., Maiorino, M. & Gregolin, C. The selenoenzyme phospholipid hydroperoxide glutathione peroxidase. *Biochimica et Biophysica Acta (BBA) - General Subjects* **839**, 62–70 (1985).
197. Zhang, Z. *et al.* Glutathione peroxidase 4 participates in secondary brain injury through mediating ferroptosis in a rat model of intracerebral hemorrhage. *Brain Research* **1701**, 112–125 (2018).
198. Hu, C. *et al.* Reduced expression of the ferroptosis inhibitor glutathione peroxidase-4 in multiple sclerosis and experimental autoimmune encephalomyelitis. *J. Neurochem.* **148**, 426–439 (2019).
199. Hémar, A., Olivo, J.-C., Williamson, E., Saffrich, R. & Dotti, C. G. Dendroaxonal Transcytosis of Transferrin in Cultured Hippocampal and Sympathetic Neurons. *J. Neurosci.* **17**, 9026–9034 (1997).
200. Hentze, M. W., Muckenthaler, M. U., Galy, B. & Camaschella, C. Two to Tango: Regulation of Mammalian Iron Metabolism. *Cell* **142**, 24–38 (2010).
201. Robinson, S. R., Dang, T. N., Dringen, R. & Bishop, G. M. Hemin toxicity: a preventable source of brain damage following hemorrhagic stroke. *Redox Report* **14**, 228–235 (2009).
202. Dang, T., Robinson, S. R., Dringen, R. & Bishop, G. M. Uptake, metabolism and toxicity of hemin in cultured neurons. *Neurochemistry International* **58**, 804–811 (2011).
203. Kontoghiorghes, G. & Kontoghiorghe, C. Iron and Chelation in Biochemistry and Medicine: New Approaches to Controlling Iron Metabolism and Treating Related Diseases. *Cells* **9**, 1456 (2020).
204. Holt, C. E., Martin, K. C. & Schuman, E. M. Local translation in neurons: visualization and function. *Nat Struct Mol Biol* **26**, 557–566 (2019).
205. Terenzio, M. *et al.* Locally translated mTOR controls axonal local translation in nerve injury. *Science* **359**, 1416–1421 (2018).
206. Cho, Y. *et al.* Activating Injury-Responsive Genes with Hypoxia Enhances Axon Regeneration through Neuronal HIF-1α. *Neuron* **88**, 720–734 (2015).
207. Liu, P.-H., Tsai, H.-Y., Chung, Y.-W., Wang, Y.-J. & Tseng, G.-F. The proximity of the lesion to cell bodies determines the free radical risk induced in rat rubrospinal neurons subjected to axonal injury. *Anat Embryol (Berl)* **207**, 439–451 (2004).
208. Liu, P.-H., Yang, L.-H., Wang, T.-Y., Wang, Y.-J. & Tseng, G.-F. Proximity of lesioning determines response of facial motoneurons to peripheral axotomy. *J Neurotrauma* **23**, 1857–1873 (2006).
209. Lorenzana, A. O., Lee, J. K., Mui, M., Chang, A. & Zheng, B. A surviving intact branch stabilizes remaining axon architecture after injury as revealed by in vivo imaging in the mouse spinal cord. *Neuron* **86**, 947–954 (2015).
210. Geisler, S. *et al.* Vincristine and bortezomib use distinct upstream mechanisms to activate a common SARM1-dependent axon degeneration program. *JCI Insight* **4**, e129920 (2019).
211. Gerdts, J., Brace, E. J., Sasaki, Y., DiAntonio, A. & Milbrandt, J. SARM1 activation triggers axon degeneration locally via NAD+ destruction. *Science* **348**, 453–457 (2015).

7. Appendix

Table S1 Supporting Fig. 23 The AUC analyses of hemin-induced AxD.

	Kolmogorov-Smirnov test	**Levené test**	**Omnibus Test**	**Post hoc Test**
AUC Axon area	Z = 0.093, *P* = 0.200	*F*(3,20) = 0.116, *P* = 0.949	one-way ANOVA *F*(3,20) = 8.547, *P* = 0.001, partial-η^2 = 0.562	post hoc Bonferroni *P* = 0.026 for 50 µM, *P* = 0.018 for 100 µM, and *P* < 0.001 for 200 µM vs. 0 µM
AUC Axonal swelling area	Z = 0.104, *P* = 0.200	*F*(3,20) = 0.993, *P* = 0.416	one-way ANOVA *F*(3,20) = 6.721, *P* = 0.003, partial-η^2 = 0.502	post hoc Bonferroni *P* = 0.012 for 50 µM, *P* = 0.005 for 100 µM, and *P* = 0.016 for 200 µM vs. 0 µM
AUC Axonal fragment area	Z = 0.245, *P* = 0.001	*F*(3,20) = 5.800, *P* = 0.005	Kruskal-Wallis Test [chi]2 (3,*N* = 24) = 16.393, *P* = 0.001, η^2 = 0.713	post hoc Mann-Whitney test with Bonferroni correction at α = 0.0167, *P* = 0.037 for 50 µM, *P* = 0.004 for 100 µM and 200 µM vs. 0 µM

Table S2 Supporting Fig. 24 Time- and concentration-dependent AxD after exposure to hemin.

Readout	**Mauchly test**	**Omnibus Test**	**post hoc Test**
Axon area	Chi2 is undefined because the number of repeated measurements is greater than the sample size; hence, sphericity was not assumed and the Greenhouse-Geisser correction was applied	one-way ANOVA with Greenhouse-Geisser correction (ε = 0.045) across time*group: *F*(6.109) = 19.758, *P* < 0.001, partial-η^2 = 0.748	post hoc Bonferroni *P* = 0.018 for 50 µM from 15 hours (*P* < 0.001 from 19 hours), *P* = 0.040 for 100 µM from 14 hours (*P* < 0.001 from 18.5 hours), *P* = 0.020 for 200 µM from 11.5 hours (*P* < 0.001 from 15 hours) vs. 0 µM
Axonal swelling area		one-way ANOVA with Greenhouse-Geisser correction (ε = 0.042) across time*group: *F*(5.703) = 3.201, *P* = 0.013, partial-η^2 = 0.324	post hoc Bonferroni *P* = 0.030 for 50 µM from 8 hours, *P* = 0.019 for 100 µM from 6 hours, *P* = 0.010 for 200 µM from 6 hours until 18.5 h vs. 0 µM
Axonal fragment area		one-way ANOVA with Greenhouse-Geisser correction (ε = 0.026) across time*group: *F*(3.522) = 9.115, *P* < 0.001, partial-η^2 = 0.578	post hoc Bonferroni *P* = 0.044 for 100 µM from 17 hours, *P* = 0.037 for 200 µM from 9 hours vs. 0 µM

Table S3 Related to Fig. 30 Comparison of the linear regression slopes of the four morphological patterns of AxD. Bonferroni correction for multiple comparisons was applied, α = 0.0083 was considered statistically significant (six comparisons).

Morphological pattern of AxD	**Linear regression slopes**
Granular degeneration	*F*(1,22) = 19.330, R^2 = 0.468, *P* < 0.001
Retraction degeneration	*F*(1,22) = 0.066, R^2 = 0.003, *P* = 0.800
Swelling degeneration	*F*(1,22) = 16.900, R^2 = 0.434, *P* < 0.001
Transport degeneration	*F*(1,22) = 5.757, R^2 = 0.207, *P* = 0.025
Morphological pattern of AxD	**Comparison of the slopes**
Granular degeneration vs. retraction degeneration	*F*(1,44) = 6.971, *P* = 0.011, not significant at α = 0.008
Granular degeneration vs. swelling degeneration	*F*(1,44) = 0.202, *P* = 0.655

Granular degeneration vs. transport degeneration	$F(1,44) = 8.865$, $P = 0.005$
Retraction degeneration vs. swelling degeneration	$F(1,44) = 7.842$, $P = 0.0076$
Retraction degeneration vs. transport degeneration	$F(1,44) = 0.406$, $P = 0.528$
Swelling degeneration vs. transport degeneration	$F(1,44) = 9.074$, $P = 0.004$

Table S4 Supporting Fig. 31 Statistical analysis of the features of AxD upon exposure to hemin.

	Kolmogorov-Smirnov test	**Levené test**	**Test**
Axon area	Z = 0.233, $P < 0.001$	$F(1,50) = 0.019$, $P = 0.890$	Mann-Whitney U test: $U < 0.001$, $P < 0.001$ for 100 µM $r = 0.858$
Axonal swelling area	Z = 0.093, $P = 0.200$	$F(1,50) = 2.734$, $P = 0.104$	t-test: t (50) = -2,237, $P = 0.030$ for 100 µM, $d = -0.633$
Axonal fragment area	Z = 0.257, $P < 0.001$	$F(1,50) = 17.841$ $P < 0.001$	Mann-Whitney U test: $U < 0.001$, $P < 0.001$ for 100 µM r = 0.858

Table S5 Supporting Fig. 32 Concentration-responses of the calpain inhibitors in hemin-induced AxD.

	Axon area	**Axonal swelling area**	**Axonal fragment area**
ALLN	Kruskal-Wallis Test [chi]2 (4,$N = 30$) = 15.746, $P = 0.003$, $\eta^2 = 0.543$ post hoc Mann-Whitney U test with correction at α = 0.0125: Axon: $P = 0.423$ for 0.1 µM, $P = 0.749$ for 1 µM, $P = 0.109$ for 10 µM, $P = 0.004$ for 100 µM	Kruskal-Wallis Test [chi]2 (4,$N = 30$) = 15.458, $P = 0.004$, $\eta^2 = 0.533$ post hoc Mann-Whitney U test with correction at α = 0.0125: Axonal swelling: $P = 1$ for 0.1 µM, $P = 0.262$ for 1 µM, $P = 0.055$ for 10 µM, $P = 0.010$ for 100 µM	Kruskal-Wallis Test [chi]2 (4,$N = 30$) = 17.144, $P = 0.002$, $\eta^2 = 0.591$ post hoc Mann-Whitney U test with correction at α = 0.0125: Axonal fragment: $P = 0.423$ for 0.1 µM, $P = 0.522$ for 1 µM, $P = 0.010$ for 10 µM, $P = 0.004$ for 100 µM
E64d	Kruskal-Wallis Test [chi]2 (4,$N = 30$) = 1.802, $P = 0.772$, $\eta^2 = 0.062$	Kruskal-Wallis Test [chi]2 (4,$N = 30$) = 4.959, $P = 0.292$, $\eta^2 = 0.171$	Kruskal-Wallis Test [chi]2 (4,$N = 30$) = 2.215, $P = 0.696$, $\eta^2 = 0.076$
MDL28170	Kruskal-Wallis Test	Kruskal-Wallis Test	Kruskal-Wallis Test

	[chi]2 (4,*N* = 30) = 14.052, *P* = 0.007, η^2 = 0.485 post hoc Mann-Whitney U test with correction at α = 0.0125: Axon: *P* = 0.749 for 0.1 µM, *P* = 0.873 for 1 µM, *P* = 0.749 for 10 µM, *P* = 0.004 for 100 µM	[chi]2 (4,*N* = 30) = 4.933, *P* = 0.294, η^2 = 0.170	[chi]2 (4,*N* = 30) = 13.092, *P* = 0.011, η^2 = 0.451 post hoc Mann-Whitney U test with correction at α = 0.0125: Axonal fragment: *P* = 0.262 for 0.1 µM, *P* = 0.631 for 1 µM, *P* = 0.337 for 10 µM, *P* = 0.016 for 100 µM

Table S6 Supporting Fig. 33 Concentration-responses of the transcription and translation inhibitors in hemin-induced AxD.

	Axon area	**Axonal swelling area**	**Axonal fragment area**
Act-D	Kruskal-Wallis Test [chi]2 (4,*N* = 30) = 6.740, *P* = 0.150, η^2 = 0.232	Kruskal-Wallis Test [chi]2 (4,*N* = 30) = 6.138, *P* = 0.189, η^2 = 0.212	Kruskal-Wallis Test [chi]2 (4,*N* = 30) = 6.920, *P* = 0.140, η^2 = 0.239
Chx	Kruskal-Wallis Test [chi]2 (4,*N* = 30) = 22.301, *P* < 0.001, η^2 = 0.769 post hoc Mann-Whitney U test with correction at α = 0.0125: Axon: *P* = 0.200 for 0.1 µM, *P* = 0.006 for 1 µM, *P* = 0.004 for 10 µM, *P* = 0.004 for 50 µM	Kruskal-Wallis Test [chi]2 (4,*N* = 30) = 18.034, *P* = 0.001, η^2 = 0.622 post hoc Mann-Whitney U test with correction at α = 0.0125: Axonal swelling: *P* = 0.150 for 0.1 µM, *P* = 0.109 for 1 µM, *P* = 0.004 for 10 µM, *P* = 0.004 for 50 µM	Kruskal-Wallis Test [chi]2 (4,*N* = 30) = 10.576, *P* = 0.032, η^2 = 0.365 post hoc Mann-Whitney U test with correction at α = 0.0125: Axonal fragment: *P* = 0.522 for 0.1 µM, *P* = 0.631 for 1 µM, *P* = 0.006 for 10 µM, *P* = 0.037 for 50 µM

Table S7 Supporting Fig. 34 Concentration-responses of the necroptosis inhibitors in hemin-induced AxD.

	Axon area	**Axonal swelling area**	**Axonal fragment area**
GSK872	Kruskal-Wallis Test [chi]2 (4,*N* = 30) = 1.217, *P* = 0.875, η^2 = 0.042	Kruskal-Wallis Test [chi]2 (4,*N* = 30) = 3.940, *P* = 0.414, η^2 = 0.136	Kruskal-Wallis Test [chi]2 (4,*N* = 30) = 4.899, *P* = 0.298, η^2 = 0.169
NSA	Kruskal-Wallis Test [chi]2 (4,*N* = 30) = 7.333, *P* = 0.119, η^2 = 0.253	Kruskal-Wallis Test [chi]2 (4,*N* = 30) = 5.123, *P* = 0.275, η^2 = 0.177	Kruskal-Wallis Test [chi]2 (4,*N* = 30) = 11.940, *P* = 0.018, η^2 = 0.412 post hoc Mann-Whitney U test with correction at α = 0.0125: Axonal fragment: *P* = 0.873 for 0.1 µM, *P* = 0.873 for 1 µM, *P* = 0.200 for 5 µM,

			P = 0.010 for 10 µM
Nec-1 + Nec1i	Kruskal-Wallis Test [chi]2 (8,N = 30) = 8.972, P = 0.345, η^2 = 0.309	Kruskal-Wallis Test [chi]2 (8,N = 30) = 4.345, P = 0.825, η^2 = 0.015	Kruskal-Wallis Test [chi]2 (8,N = 30) = 12.199, P = 0.143, η^2 = 0.421

Table S8 Supporting Fig. 35 Concentration-responses of the autophagy inhibitors in hemin-induced AxD.

	Axon area	**Axonal swelling area**	**Axonal fragment area**
BafA1	Kruskal-Wallis Test [chi]2 (4,N = 30) = 19.282, P = 0.001, η^2 = 0.665 post hoc Mann-Whitney U test with correction at α = 0.0125: Axon: P = 0.337 for 0.001 µM, P = 0.006 for 0.01 µM, P = 0.004 for 0.05 µM, P = 0.004 for 0.1 µM	Kruskal-Wallis Test [chi]2 (4,N = 30) = 10.508, P = 0.033, η^2 = 0.362 post hoc Mann-Whitney U test with correction at α = 0.0125: Axonal swelling: P = 0.150 for 0.001 µM, P = 0.037 for 0.01 µM, P = 0.016 for 0.05 µM, P = 0.004 for 0.1 µM	Kruskal-Wallis Test [chi]2 (4,N = 30) = 13.458, P = 0.009, η^2 = 0.464 post hoc Mann-Whitney U test with correction at α = 0.0125: Axonal fragment: P = 1 for 0.001 µM, P = 0.016 for 0.01 µM, P = 0.025 for 0.05 µM, P = 0.037 for 0.1 µM
Mdivi-1	Kruskal-Wallis Test [chi]2 (4,N = 30) = 5.974, P = 0.201, η^2 = 0.206	Kruskal-Wallis Test [chi]2 (4,N = 30) = 5.174, P = 0.270, η^2 = 0.178	Kruskal-Wallis Test [chi]2 (4,N = 30) = 4.460, P = 0.347, η^2 = 0.154

Table S9 Supporting Fig. 36 Concentration-response of the apoptosis inhibitor in hemin-induced AxD.

	Axon area	**Axonal swelling area**	**Axonal fragment area**
zVAD-fmk	Kruskal-Wallis Test [chi]2 (4,N = 30) = 5.359, P = 0.252, η^2 = 0.185	Kruskal-Wallis Test [chi]2 (4,N = 30) = 5.243, P = 0.263, η^2 = 0.181	Kruskal-Wallis Test [chi]2 (4,N = 30) = 6.723, P = 0.151, η^2 = 0.232

Table S10 Supporting Fig. 37-38 Cleaved caspase-3 expression upon staurosporine and hemin treatment

	Cleaved caspase-3
Staurosporine-treated axon	Mann-Whitney U test U < 0.001, P = 0.014, r = 0.870
Hemin-treated axons	Kruskal-Wallis Test [chi]2 (4,N = 20) = 4.203, P = 0.379, η^2 = 0.221

Table S11 Supporting Fig. 39 Concentration-responses of the ferroptosis inhibitors in hemin-induced AxD.

	Axon area	Axonal swelling area	Axonal fragment area
NAC	Kruskal-Wallis Test [chi]2 (4,*N* = 30) = 5.454, *P* = 0.244, η^2 = 0.188	Kruskal-Wallis Test [chi]2 (4,*N* = 30) = 1.892, *P* = 0.756, η^2 =0 .065	Kruskal-Wallis Test [chi]2 (4,*N* = 30) = 5.759, *P* = 0.218, η^2 = 0.199
DFO	Kruskal-Wallis Test [chi]2 (4,*N* = 30) = 14.865, *P* = 0.005, η^2 = 0.513 post hoc Mann-Whitney U test with correction at α = 0.0125: Axon: *P* = 0.749 for 10 µM, *P* = 0.025 for 50 µM, *P* = 0.004 for 100 µM, *P* = 0.006 for 200 µM	Kruskal-Wallis Test [chi]2 (4,*N* = 30) = 2.783, *P* = 0.595, η^2 = 0.096	Kruskal-Wallis Test [chi]2 (4,*N* = 30) = 4.391, *P* = 0.356, η^2 = 0.151
Fer-1	Kruskal-Wallis Test [chi]2 (4,*N* = 30) = 0.185, *P* = 0.996, η^2 = 0.0006	Kruskal-Wallis Test [chi]2 (4,*N* = 30) = 7.127, *P* = 0.129, η^2 = 0.246	Kruskal-Wallis Test [chi]2 (4,*N* = 30) = 5.935, *P* = 0.204, η^2 = 0.205
U0126+ U0124	Kruskal-Wallis Test [chi]2 (8,*N* = 30) = 6.063, *P* = 0.640, η^2 = 0.209	Kruskal-Wallis Test [chi]2 (8,*N* = 30) = 1.515, *P* = 0.992, η^2 = 0.052	Kruskal-Wallis Test [chi]2 (8,*N* = 30) = 12.158, *P* = 0.144, η^2 = 0.419
Trolox	Kruskal-Wallis Test [chi]2 (4,*N* = 30) = 3.901, *P* = 0.420, η^2 = 0.135	Kruskal-Wallis Test [chi]2 (4,*N* = 30) = 3.303, *P* = 0.508, η^2 = 0.114	Kruskal-Wallis Test [chi]2 (4,*N* = 30) = 12.426, *P* = 0.014, η^2 = 0.428 post hoc Mann-Whitney U test with correction at α = 0.0125: Axonal fragment: *P* = 0.749 for 0.1 µM, *P* = 0.200 for 1 µM, *P* = 0.262 for 10 µM, *P* = 0.037 for 100 µM

Table S12 Supporting Fig. 40 MDA and TfR1 expression upon hemin treatment

	MDA	TfR1
Hemin-treated axons	Kruskal-Wallis Test [chi]2 (3,*N* = 16) = 11.082, *P* = 0.011, η^2 = 0.739 post hoc Mann-Whitney U test with correction at α = 0.017: *P* = 0.14 for 8 hours, *P* = 0.14 for 16 hours, *P* = 0.14 for 24 hours	Kruskal-Wallis Test [chi]2 (3,*N* = 16) = 8.664, *P* = 0.034, η^2 = 0.578 post hoc Mann-Whitney U test with correction at α = 0.017: *P* = 0.14 for 8 hours, *P* = 0.14 for 16 hours, *P* = 0.14 for 24 hours

8. Publication list

Publications

First-author publications

Palumbo A*, Yamil AV Maluje, Boltze J, Zille M*, “Neuroprotective inhibitors of ferroptosis and necroptosis do not prevent hemin-induced AxD (tentative title)”, *corresponding authors, **in preparation**, **2021**

Palumbo A*, Gruening P, Landt SK, Heckmannn LE, Bartram L, Pabst A, Flory C, Ikhsan M, Pietsch S, Schulz R, Kren C, Koop N, Boltze J, Madany Mamlouk A, Zille M*, “Deep learning to decipher the progression and morphology of axonal degeneration”, *corresponding authors, **in revision**, pre-print version on bioRxiv, **2020**, doi: 10.1101/2020.08.26.269092

Co-author publications in peer-reviewed journals

Boltze J, Aronowski JA, Badaut J, Buckwalter MS, Caleo M, Chopp M, Dave KR, Didwischus N, Dijkhuizen RM, Doeppner TR, Dreier JP, Fouad K, Gelderblom M, Gertz K, Golubczyk D, Gregson BA, Hamel E, Hanley DF, Härtig W, Hummel FC, Ikhsan M, Janowski M, Jolkkonen J, Karuppagounder SS, Keep RF, Koerte IK, Kokaia Z, Li P, Liu F, Lizasoain I, Ludewig P, Metz GA, Montagne A, Obenaus A, **Palumbo A**, Pearl M, Perez-Pinzon M, Planas AM, Plesnila N, Popa-Wagner A, Raval AP, Rueger MA, Sansing LH, Sohrabji F, Stagg CJ, Stetler RA, Stowe AM, Sun D, Tanter M, Vay SU, Vemuganti R, Vivien D, Walczak P, Wang J, Xiong Y, and Zille M, “New mechanistic insights, novel treatment paradigms, and clinical progress in cerebrovascular diseases”, Frontiers in Aging Neuroscience, **2021,** doi: 10.3389/fnagi.2021.623751

Ikhsan M, **Palumbo A**, Rose D, Zille M, Boltze J, “Concise Review: Neuronal Stem Cell–Drug Interactions: A Systematic Review and Meta-Analysis”, Stem Cells Translational Medicine, **2019**, doi:10.1002/sctm.19-0020

Co-author publications in peer-reviewed conference proceedings

Gruening P, **Palumbo A**, Heckmann L, Landt S, Brackhagen L, Zille M, Madany Mamlouk A, “Robust and markerfree *in vitro* axon segmentation with CNNs”, 9th EAI International Conference on Wireless Mobile Communication and Healthcare, **2021**, doi: 10.1007/978-3-030-70569-5_17

Gruening P, **Palumbo A**, Zille M, Barth E, Madany Mamlouk A, “A task-dependent active learning method for axon segmentation with CNNs”, AUTOMED2020, **2020**, doi: 10.18416/AUTOMED.2020

Menon NK, **Palumbo A**, Gruening P, Landt SK, Heckmannn L, Bartram L, Madany Mamlouk A, Zille M, “Segmentation of fluorescently labeled axons in a model of brain hemorrhage-induced axonal degeneration using convolutional neural networks”, Student Conference Proceedings 2020, **2020**, ISBN: 978-3-945954-62-1